University of Glasgow

Millimetre-wave and Terahertz Signal Generation Based on Monolithic Integrated Dual-wavelength Semiconductor DFB Lasers

Bocheng Yuan

Submitted in fulfilment of the requirements for the Degree of

Doctor of Philosophy (PhD)

James Watt School of Engineering

College of Science and Engineering

University of Glasgow

October 2024

Abstract

The high-frequency RF signals generated using the optical beat frequency method exhibit significant design flexibility in terms of frequency. With the advancement of photonic integration technology, these devices achieve a high level of integration, enabling the generation and modulation of signals to be completed chip level devices. Typically, the beat frequency generation process requires two independent single-wavelength lasers, necessitating additional design considerations to ensure the polarization and phase relationship between the two devices. Additionally, at least two power sources are needed to pump the two devices separately, which means that external noise is more likely to affect the phase correlation between the two independent optical signals.

This thesis presents the design, fabrication, and characterisation of a series of monolithically integrated dual-wavelength lasers. The main feature is that two lasing wavelengths are simultaneously emitted within a single resonant cavity, resulting in the two lasing modes naturally having the same polarisation. Lasers and their arrays which achieved beat frequencies range from 50 GHz to 1 THz were fabricated based on three different grating structures: two π phase shifts with equivalent chirped gratings, sidewall grating with lateral modulation of grating coupling coefficient, and superimposed sampled Bragg gratings. For devices operating at terahertz frequencies, the frequency interval can be precisely controlled. With a grating pattern precision of 0.5 nm, the theoretical minimum beat frequency interval can reach 1.1 GHz.

Furthermore, by injecting an external optical frequency comb's sub-harmonic to the integrated electro-absorption modulator, the phases of the two lasing modes are locked. The experiment recorded two frequencies, 67.75 GHz and 136 GHz, both of which exhibited a linewidth of 1 Hz in the locked state. The phase noise test results indicate that the phase noise of the generated signal adheres to the inherent attenuation law of the frequency comb. This confirms that the injection locking of a dual-wavelength laser can successfully multiply the frequency of an external RF signal without introducing additional noise.

Experimental results confirm that the monolithically integrated dual-wavelength laser possesses a wide design range for beat frequencies. Moreover, after locking, the generated millimetre-wave and THz signals exhibit extremely narrow linewidths and very low phase noise, making the system highly stable and precise for high-frequency applications. This

device has significant potential to become a crucial component in microwave/THz photonic integration.

Publications

Journal

1. **B. Yuan**, Y. Fan, S. Ye, Y. Zhang, Y. Sun, X. Sun, W. Cheng, S. Liang, Y. Huang, R. Zhang, J. Wang, J. H. Marsh, L. Hou, "Dual-Wavelength DFB Laser Array Based on Sidewall Grating and Lateral Modulation of the Grating Coupling Coefficient," in *Journal of Lightwave Technology*, vol. 41, no. 9, pp. 2775-2784, 1 May1, 2023.
2. **B. Yuan**, Y. Fan, S. Zhu, W. Cheng, Y. Zhang, X. Chen, Y. Sun, S. Liang, Y. Huang, R. Zhang, J. Akbar, J. H. Marsh, L. Hou, "Millimeter-wave generation based on a monolithic dual-wavelength DFB laser with four phase-shifted sampled gratings and equivalent chirp technology," *Opt. Lett*. 48, pp. 5093-5096, 2023.
3. L. Hou, **B. Yuan**, Y. Fan, X. Sun, Y. Sun, S. Zhu., S. Sweeney, J. H. Marsh, "Monolithic Dual Wavelength DFB Lasers Based on Sidewall Gratings for THz/MMW Signal Generation," in *IEEE Journal of Selected Topics in Quantum Electronics*,2024 (early access).
4. M. Al-Rubaiee, **B. Yuan**, Y. Fan, S. Zhu, J. H. Marsh and L. Hou, "Ultrastable 10 GHz Mode-Locked Laser on Semi-Insulating Substrate Through RF Injection Locking," in *IEEE Photonics Technology Letters*, vol. 36, no. 19, pp. 1189-1192, 1 Oct.1, 2024.
5. Y. Fan, **B. Yuan,** M. Al-Rubaiee, Y. Sun, S. Zhu, J. Akbar, J. H. Marsh, L. Hou, "Millimeter-Wave Generation Based on Four Phase-Shifted Sampled Moiré Grating Dual-Wavelength DFB Laser," in *IEEE Photonics Technology Letters*, vol. 36, no. 4, pp. 282-285, 15 Feb.15, 2024.
6. Y. Fan, **B. Yuan,** M. Al-Rubaiee, Y. Sun, S. Zhu, J. H. Marsh, L. Hou, "Dual-wavelength distributed feedback laser array based on four-phase-shifted sampled Bragg grating for terahertz generation," *Opt. Lett*. 49, pp. 3472-3475, 2024.
7. Y. Sun, **B. Yuan**, X. Sun, S. Liang, Y. Huang, R. Zhang, Y. Ye, Y. Fan, W. Cheng, J. H. Marsh, L. Hou "DFB laser array based on four phase-shifted sampled Bragg gratings with precise wavelength control," *Opt. Lett*. 47, pp. 6237-6240, 2022. (doi: 10.1364/OL.475909)
8. S. Ye, X. Sun, **B. Yuan**, P. Read, P. Maidment, Y. Huang, R. Zhang, S. Watson, A. Kelly, J. H. Marsh, L. Hou, "1.55-μm Sidewall Grating DFB Lasers Integrated With a Waveguide Crossing for an Optical Beam Forming Network," in *IEEE Photonics Technology Letters*, vol. 35, no. 14, pp. 785-788, 15 July15, 2023.
9. W. Cheng, X. Sun, S. Ye, **B. Yuan,** Y. Sun, J. H. Marsh, L. Hou, "Sidewall grating slot waveguide microring resonator biochemical sensor," *Opt. Lett*. 48, pp. 5113-5116, 2023.
10. W. Cheng, X. Sun, S. Ye, **B. Yuan,** J. Xiong, X. Liu, Y. Sun, J. H. Marsh, L. Hou, "Double slot micro ring resonators with inner wall angular gratings as ultra-sensitive biochemical sensors," *Opt. Express* 31, pp. 20034-20048, 2023.
11. W. Cheng, S. Ye, **B. Yuan**, J. H. Marsh, and L. Hou, "Subwavelength Grating Cascaded Microring Resonator Biochemical Sensors with Record-High Sensitivity," *ACS Photonics* 11 (8), pp.3343-3350, 2024.

Conference

1. M. Al-Rubaiee, S. Ye, **B. Yuan, Y.** Fan, J. H. Marsh, and L. Hou, "10 GHz Low Divergence Angle Mode-Locked Lasers with Ultralow Timing Jitter through Injection-Locking Techniques", *CLEO 2024*, Charlotte, North Carolina, USA, 05-10 May 2024. (Accepted for Publication)

2. W. Cheng, X. Sun, S. Ye, **B. Yuan**, J. H. Marsh, L. Hou, "High Sensitivity FSR-Free Sidewall Grating Slot Waveguide Microring Resonator Biochemical Sensors ", *CLEO 2024*, Charlotte, North Carolina, USA, 05-10 May 2024. (Accepted for Publication)
3. W. Cheng, X. Sun, S. Ye, **B. Yuan,** J. H. Marsh, and L. Hou, "Subwavelength Grating Cascaded Microring Resonator Biochemical Sensors with Record-High Sensitivity". *CLEO 2024*, Charlotte, North Carolina, USA, 05-10 May 2024. (Accepted for Publication)
4. Y. Fan, **B. Yuan,** M. Al-Rubaiee, J. H. Marsh, L. Hou, "Dual-wavelength DFB Laser Based on Four Phase-shifted Sampled Moiré Grating for MMW Generation". *CLEO 2024*, Charlotte, North Carolina, USA, 05-10 May 2024. (Accepted for Publication)
5. M. Al-Rubaiee, S. Ye, **B. Yuan**, Y. Fan, J. H. Marsh and L. Hou, "Ultra-stable 10 GHz Optical Clocks Based on Injection Mode-Locked Semiconductor Lasers", *46th European Semiconductor Laser Workshop ESLW 2023*, University of Glasgow, 30 September 2023.
6. Y. Sun, **B. Yuan**, X. Sun, J. H. Marsh, L. Hou, "Eight-Channel DFB Laser Array Based on Four Phase-Shifted Sampled Bragg Gratings", *46th European Semiconductor Laser Workshop* (ESLW 2023), Glasgow, UK, 30 Sept 2023.
7. **B. Yuan** Y. Fan, S. Zhu, W. Cheng, Y. Zhang, X. Chen, J. H. Marsh, L. Hou, "Monolithic dual-wavelength laser array based on four phase-shifted grating and equivalent chirp technology," *49th European Conference on Optical Communications* (ECOC 2023), Hybrid Conference, Glasgow, UK, 2023, pp. 617-619.
8. W. Cheng, S. Ye, X. Sun, **B. Yuan**, J. H. Marsh and L. Hou, "Double Slot Micro Ring Resonators with Inner Wall Angular Gratings as Ultra Highly Sensitive Biochemical Sensors," *2022 IEEE Photonics Conference (IPC)*, Vancouver, BC, Canada, 2022, pp. 1-2.
9. Y. Fan, S. Ye, Y. Huang, **B. Yuan**, J. H. Marsh and L. Hou, "Dual-Wavelength DFB Laser with 1.28 THz Frequency Spacing Based on Four Phase Shifted Sampling Gratings," *2022 IEEE Photonics Conference (IPC)*, Vancouver, BC, Canada, 2022, pp. 1-2.
10. Y. Sun, **B. Yuan**, J. H. Marsh, X. Sun, Y. Fan and L. Hou, "DFB Laser Array Based on Four Phase-Shifted Sampled Bragg Gratings," *2022 IEEE Photonics Conference (IPC)*, Vancouver, BC, Canada, 2022, pp. 1-2.
11. **B. Yuan**, S. Ye, Y. Zhang, X. Chen, J. H. Marsh, L. Hou, "Dual-Wavelength DFB Laser With 640 GHz Frequency Spacing Based on Sidewall Grating and Reconstruction Equivalent-Chirp Technology", *IEEE Photonics Conference* (IPC), Vancouver, BC, Canada, 13-17 Nov 2022.
12. S. Zhu, W. Cheng, **B. Yuan,** Y. Fan, Y. Sun, A. S. Hezarfen, J. H. Marsh, and L. Hou, "High Sensitivity Biochemical Sensors Based on a Mach-Zehnder Interferometer with a Slot Bus Waveguide and Double Slot Hybrid Plasmonic Waveguide", In: *50th European Conference on Optical Communication* (ECOC2024), Frankfurt, Germany, 22-26 Sept 2024, (Accepted for Publication)
13. S. Zhu, **B. Yuan,** Y. Fan, Y. Sun, J. H. Marsh, and L. Hou, "Tunable Dual-band Microwave Photonic Filters Covering 37.2 GHz to 186.1 GHz Utilizing Chirped Sampled Gratings", In: *50th European Conference on Optical Communication* (ECOC2024), Frankfurt, Germany, 22-26 Sept 2024, (Accepted for Publication)
14. Y. Fan, Y. Zhang, Y. Sun, **B. Yuan**, J. H. Marsh and L. Hou, "Monolithic Optical Injection Locking DFB Lasers Based on Four Phase-Shifts Sampling Sections," *2023 Conference on Lasers and Electro-Optics Europe & European Quantum Electronics Conference (CLEO/Europe-EQEC)*, Munich, Germany, 2023, pp. 1-1.

15. **B. Yuan,** Y. Fan, S. Zhu, Y. Zhang, J. H. Marsh and L. Hou, "Dual-wavelength DFB Laser Based on Four Phase-shifts Sections and Equivalent Chirp Technology for Millimeter-wave Generation," *2023 Conference on Lasers and Electro-Optics Europe & European Quantum Electronics Conference (CLEO/Europe-EQEC)*, Munich, Germany, 2023, pp. 1-1.
16. W. Cheng, X. Sun, S. Ye, **B. Yuan,** X. Liu, J. H. Marsh, and L. Hou, "Inner-Wall Grating Double Slot Microring Resonator for High Sensitivity and Large Measurement Range Label-Free Biochemical Sensing," *2023 Conference on Lasers and Electro-Optics (CLEO)*, San Jose, CA, USA, 2023, pp. 1-2.
17. Y. Fan, **B. Yuan**, S. Ye, Y. Sun, J. H. Marsh and L. Hou, "Dual Wavelength DFB Laser Array Based on Four Phase Shifted Sampled Bragg Gratings for THz Generation," *2023 Conference on Lasers and Electro-Optics (CLEO)*, San Jose, CA, USA, 2023, pp. 1-2.

Table of contents

Chapter 4: Experimatal results

Chapter 5: Obtaining high-quality RF signals through optical injection locking

Chapter 6: Future discussion

List of Figures

Fig 4.6	(a) Measured P-I curves of the device with 30 nm/mm chirp rate under different V_{EAM}, (b) P-I curves of the devices with different chirp rate for values of V_{EAM} shown in Table 4.1.
Fig 4.7	Schematic of the RF signal measurement system.
Fig 4.8	(a) Measured RF signals of the DWL array, (b) RF signal linewidth of the array versus I_{DFB}, (c) fitted linewidth curve of the device with 70 nm/mm chirp rate, (d) 2-D optical spectrum, (e) wavelength spacing and PM, (f) RF frequency and SNR versus TEC temperature of the device with 70 nm/mm chirp rate under I_{DFB}= 75 mA and V_{EAM}= −1.7 V.
Fig 4.9	(a) Microscope image of the dual-wavelength DFB laser array with L=1200 μm, (b) SEM image of the grating at the beginning of the DFB cavity, (c) SEM image of the grating at the middle of the DFB cavity.
Fig 4.10	2-D optical spectrum map of a laser with L = 1200 μm, D=0.6 μm when the EAM reverse voltage is set to 0 V (a), and –2.5 V (b).
Fig 4.11	The spectra of the devices with DFB cavity lengths of (a) 1200 μm operating at I_{DFB}=105 mA, V_{EAM}=-2.5V, and (b) 1000 μm, I_{DFB}=112 mA, V_{EAM}=-1.1V, with a fixed D=0.6 μm.
Fig 4.12	(a) $\Delta\lambda$ and power margin between λ_1 and λ_2 versus I_{DFB} when V_{EAM} is –2.5 V. (b) $\Delta\lambda$ versus V_{EAM}. (c) One-hour 2-D spectral scan of a laser at time intervals of 5 min when L = 1200 μm, D=0.6 μm. (d) Δλ and power margin between λ_1 and λ_2 versus time.
Fig 4.13	Measured *P-I* curves for (a) L=1200 μm, D=0.6 μm, (b) a laser array with different D values when L=1200 μm, V_{EAM}=0 V, (c) a laser array with different D values when L=1000 μm, V_{EAM}=0 V.
Fig 4.14	(a) Measured RF spectrum from laser arrays with different D values for L=1200 μm and 1000 μm, respectively. (b) RF spectral scan over 1 hour at intervals of 5 min for a device with L=1200 μm, D=0.6 μm. (c) RF frequency and intensity versus time.
Fig 4.15	(a) RF spectrum of DFB laser with L=1200 μm, 100 MHz scanning range and 20 kHz resolution when I_{DFB}=102 mA, V_{EAM}=–2.5 V. (b) Optical linewidths of the array.
Fig 4.16	(a) Schematic of the proposed DWL based on C-SBG, and SEM images of EPS 1 (b) and EPS 2 (c), (d) microscope image of the DWL array.
Fig 4.17	Measured optical spectra of 300 GHz – 1 THz array.
Fig 4.18	Measured AC traces of 300 GHz – 1 THz array.
Fig 4.19	Schematic of THz detection.
Fig 4.20	THz radiation power versus injection currents of the array.
Fig 4.21	Schematic of the modified device, (a) after etching grating and waveguide, (b) TSRW etching, (c) metal deposition of p- and n- electrode.
Fig 4.22	SEM cross-sectional image of the fabricated device.
Fig 4.23	SEM image of the fabricated C-SBG sidewall gratings
Fig 4.24	Microscope images of (a) fabricated device electrode, (b) experimental probe set up.
Fig 4.25	Measured optical spectra of the 135-180 GHz array.
Fig 4.26	(a) Schematic of the RF frequency measurement setup, (b) photograph of the setup.
Fig 4.27	Measured RF frequency spectra.
Fig 4.28	Measured linewidth of CH1.
Fig 5.1	Schematic of injection-locking of the DWL system.
Fig 5.2	(a) Measured spectrum of the DWL at DFB current of 98 mA and EAM voltage of –1.2 V before injection, (b) measured spectrum of the OFC

	with frequency spacing of 13.55 GHz, (c) measured DWL spectrum after injection.
Fig 5.3	(a) Measured frequency spectrum from the OFC when the frequency interval is 13.55 GHz (5×), (b) measured frequency spectrum after the injection locking, (c) spectrum with 1 Hz RBW and 200 Hz span at center frequency of 67.75 GHz.
Fig 5.4	(a) Measured frequency spectrum from the OFC when the frequency interval is 2.255 GHz (30×), (b) measured frequency spectrum after the injection locking, (c) spectrum with 1 Hz RBW and 200 Hz span at center frequency of 67.75 GHz.
Fig 5.5	(a) Optical spectrum of the 136 GHz device after injection with OFC frequency interval is 13.6 GHz (10×), (b) Measured 136 GHz signal linewidth with and without locking.
Fig 5.6	Spectrum with 1 Hz RBW and 200 Hz span at center frequency of 136 GHz.
Fig 5.7	SSB phase noise analysis when the OFC's frequency interval is set as 5× (a), 10× (b), 20× (c) and 30× (d) sub-harmonics of the DWL beat frequency (67.75 GHz).

List of Tables

Acronyms

4PS	Four Phase-Shifted
AC	Autocorrelation
BG	Buried Grating
BOE	Buffered Oxide Etch
CMT	Coupled Mode Theory
CW	Continuous Wave
DAST	Diethylamino-Sulfur Tetrafluoride
DFB	Distributed Feedback
DWL	Dual-Wavelength Laser
EAM	Electro-Absorption Modulator
EDFA	Erbium Doped Fibre Amplifier
EPS	Equivalent Phase Shift
ESA	Electrical Spectrum Analyser
FP	Fabry-Pérot
FWM	Four Wave Mixing
FWHM	Full Width At Half Maximum
Gbps	Gigabits Per Second
GRINSCH	Graded Index Separate Confinement Heterostructure
HBT	Heterojunction Bipolar Transistors
HEMT	High Electron Mobility Transistors
HF	Hydrofluoric Acid
HSQ	Hydrogen Silsesquioxane
ICP	Inductively Coupled Plasma
JWNC	James Watt Nano-Fabrication Centre
MMW	Millimetre-Wave
MQW	Multi-Quantum Well
NLoS	Non-Line-Of-Sight
OFC	Optical Frequency Comb
OFD	Optical Frequency Division
OSA	Optical Spectrum Analyser
PCA	Photoconductive Antenna
PC	Polarisation Controller
PD	Photodetector
PEC	Proximity Effect Correction
PECVD	Plasma-Enhanced Chemical Vapor Deposition
PM	Power Margin
PMMA	Polymethyl Methacrylate
QCL	Quantum Cascade Lasers
RBW	Resolution Bandwidth
RF	Radio Frequency
RIE	Reactive Ion Etching
RoF	Radio-Over-Fiber
SAG	Selective Area Growth
SBG	Sampled Bragg Grating
SCH	Separate Confinement Heterostructure
SEM	Scanning Electron Microscope
SHG	Second-Harmonic Generation
SiN	Silicon Nitride
SLAM	Simultaneous Localization And Mapping
SMSR	Side-Mode Suppression Ratio

SOA	Semiconductor Optical Amplifier
SOI	Silicon On Insulator
SSB	Single Sideband
TEC	Thermoelectric Cooler
Tbps	Terabit-Per-Second
THz	Terahertz
TMM	Transfer Matrix Method
TSRW	Two-Step Ridge Waveguide
V2S	Vehicle-To-Sensor On-Board
V2V	Vehicle-To-Vehicle
V2X	Vehicle-To-Everything
VOA	Variable Optical Attenuator

Acknowledgments

I would like to take this opportunity to express my gratitude to all the individuals who have supported me throughout my academic journey.

First and foremost, I would like to express my deepest gratitude to my supervisor, Dr. Lianping Hou, for his invaluable guidance and support throughout my studies. Your vast knowledge, academic rigor, and constant encouragement have been an incredible source of guidance throughout my PhD journey. Your passion for research and attention to detail have profoundly influenced the way I approach problems, and your feedback has pushed me to refine my work to the highest standards. I am particularly thankful for the freedom you gave me to explore my ideas while always being there to offer insightful suggestions and advice.

I would also like to extend my heartfelt thanks to Professor John H. Marsh, whose profound knowledge and unique insights in the fields of photonic devices and semiconductor materials have left a lasting impression on me. Whenever I veered off track in my pursuit of knowledge, your guidance helped broaden my perspective and set me on the right path. The occasional light-hearted jokes in Chinese added a sense of joy and camaraderie to the research group, making the journey even more enjoyable.

I would like to express my gratitude to Professor Stephen Sweeney for his insightful guidance on my publications and for assistance when I lacked experimental equipment. Your support has been invaluable to my research.

I would like to thank Professor Yunshan Zhang for the valuable discussions over the past three years, which have deepened my understanding of device applications. I sincerely hope that, in the future, I can transition from being your student to becoming your friend. I also extend my gratitude to Professor Xiangfei Chen for your unwavering support, and I hope that in the future, I will be capable of offering assistance for you.

Dr. Shengwei Ye has been my mentor in nanofabrication technology, guiding me from a novice to a skilled practitioner. I am deeply grateful for his hands-on instruction and selfless support throughout this process. I would also like to thank the staff at JWNC for their patient guidance in teaching me how to use various instruments and for explaining their underlying principles. My work would not have been possible without your support.

My colleagues and friends, Yizhe Fan, Simeng Zhu, and Yiming Sun always sharing the ups and downs of life in Scotland with me. I wish you both success in finding your own paths and pursuing what you love. Of course, a special thanks to Mohanad for introducing me to the delights of Iraqi cuisine, which has truly opened the door to a whole new world of flavours for me.

Lastly, I want to express my deepest gratitude to my parents and family. Your support has been selfless and unwavering, despite the 8-hour time difference that separates us, you have always been my most reliable source of strength. I also want to thank my beloved Mengjun Li, for standing by my side through every difficult moment. I look forward to sharing a beautiful future together.

Thanks to all of you,
Bocheng Yuan

Author Declaration

I hereby declare that the submitted PhD thesis, titled **Millimetre-wave and Terahertz Signal Generation Based on Monolithic Integrated Dual-wavelength Semiconductor DFB Lasers**, is the result of my independent and original research conducted at the James Watt School of Engineering, University of Glasgow. All sources of information and materials used in the thesis have been clearly cited and acknowledged within the text. Where the work of others has been included, it has been properly referenced following academic conventions.

I solemnly declare that this thesis does not contain any instances of academic misconduct, such as plagiarism, fabrication, or falsification of data. This work has not been submitted, either in whole or in part, for any other degree or qualification. I assume full responsibility for the legitimacy and authenticity of the findings presented in this thesis.

Bocheng Yuan

Chapter 1: Introduction

1.1 Overview of millimetre-wave and terahertz technology.

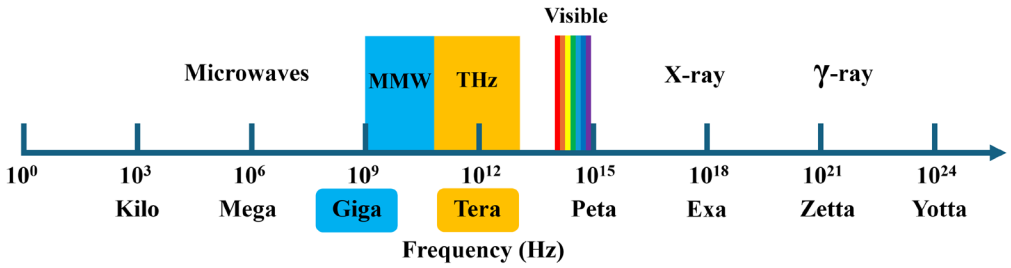

Fig. 1.1 The millimetre-wave and terahertz region in the whole electromagnetic spectrum.

Due to their critical roles in wireless communication, radar, imaging, and medical applications, the millimetre-wave (MMW) and terahertz (THz) frequency bands have been research hotspots over the past decade.

MMW refer to electromagnetic waves with a radio frequency (RF) range of 30 GHz to 300 GHz, corresponding to wavelengths of 10 mm to 1 mm. This frequency band was first studied by Indian physicist Jagadish Chandra Bose between 1894 and 1896, during which he achieved a frequency of 60 GHz in his experiments [1]. Before 2019, MMW were primarily used in satellite and radar systems, typically in military and aerospace industries [2, 3]. However, with the surge in data consumption, the industry has recognised the need and opportunity to use MMW in next-generation mobile networks. Compared to low-frequency band communications, MMW systems possess the following communication characteristics:

1. **Higher Bandwidth Availability**: MMW frequencies offer wider bandwidths than lower frequency bands, supporting higher data transmission rates, making them ideal for applications that require ultra-high-speed data transfer, such as 5G and beyond [4].
2. **Short Wavelengths**: MMW signals have wavelengths typically ranging from 1 to 10 mm. These shorter wavelengths enable the design of compact and highly directional antenna arrays, which are essential for efficient beamforming techniques [5, 6].
3. **Directional Propagation**: MMW systems typically use highly directional antennas to overcome the increased path loss at these frequencies. Beamforming techniques

are employed to direct the signal energy toward the receiver, enhancing link reliability and reducing interference [7].

While MMW communication offers significant advantages, it also presents unique challenges:

1. **Limited Coverage and Signal Penetration**: MMW signals are more susceptible to blockages and atmospheric conditions, resulting in reduced coverage compared to lower frequency bands. They have limited ability to penetrate obstacles, such as buildings or foliage, which can affect their usability in certain scenarios [8, 9].
2. **Sensitivity to Reflections and Diffraction**: MMW signals are also highly sensitive to reflections and diffraction, which can lead to multipath fading and signal degradation. Again, sophisticated signal processing algorithms and beamforming techniques are necessary to mitigate these effects and maintain reliable communication links [9].

Based on the characteristics of MMW communication mentioned above, it is currently widely applied in the following areas:

1. **Vehicular Networks**: V2X (Vehicle-to-Everything) communication [10] is revolutionising the automotive industry by enabling vehicles to exchange information with other vehicles, infrastructure, pedestrians, and networks. The substantial bandwidth offered by MMW communications could be highly advantageous for V2X applications. Projections for future autonomous vehicles suggest that they may generate up to 1 TB of data per hour of driving, with data rates exceeding 750 Mbps. In the following, we focus on three primary use cases: Vehicle-to-Sensor on-board (V2S), Vehicle-to-Vehicle (V2V), and Vehicle-to-Infrastructure (V2I).
2. **5G/6G cellular network**: MMW is a crucial element of 5G and future networks, designed to deliver ultra-fast data rates in the order of gigabits per second (Gbps) and low latency below 10 milliseconds. MMW cellular access takes advantage of the abundant spectrum available above 10 GHz, enabling the transmission of large volumes of data at exceptionally high speeds.
3. **Satellite communications**: Satellite networks have traditionally operated in frequency bands below 6 GHz, including the L band (1-2 GHz), the S band (2-4 GHz), and the C band (4-6 GHz). However, MMW technology and higher frequency bands, such as U-band (40-60 GHz), V-band (40-75 GHz), and E-band (60-90 GHz), offer

significantly greater bandwidth. By leveraging these higher frequencies, satellite systems can establish high-capacity links that support faster data rates and accommodate bandwidth-intensive applications like ultra-high-definition video streaming and data-intensive scientific research [11, 12].

The frequency range of 0.1-3 THz, situated between the lower end of optical frequency and the higher end of microwave frequency, is referred to as the terahertz gap. This term highlights the challenge of efficiently generating and detecting signals within this frequency range [13-17].

Unlike ionizing radiation, THz frequencies are non-ionizing because their photon energy (ranging from 0.1 to 12.4 meV) is over three orders of magnitude weaker than the energy levels required to ionize atoms or molecules (typically around 12 eV). As a result, THz radiation cannot release electrons from atoms or molecules. The THz band offers a vast range of spectral resources, spanning from tens of gigahertz to several terahertz, which provides more than ten times the bandwidth available in MMW bands, while operating at least an order of magnitude below optical frequencies. Moreover, technologies for achieving terabit-per-second (Tbps) transmission in the THz band are advancing rapidly [18]. In addition to the obvious enhancement in communication bandwidth, THz technology also exhibits irreplaceable qualities and significant potential for development in the following areas due to its aforementioned characteristics.

1. **Terahertz Sensing**: At THz frequencies, the spatial resolution of signals improves significantly due to the short wavelengths, enabling high-definition spatial differentiation [19]. THz sensing techniques leverage the frequency-selective resonances of various materials within the environment, along with the small wavelengths—typically on the order of micrometres [20]. This allows for the extraction of distinctive information based on the signal's signature. While THz signals can penetrate non-conductive materials such as plastics, fabrics, paper, wood, and ceramics, they encounter challenges when interacting with metallic materials or when water significantly attenuates their radiation. The specific variations in strength and phase of THz signals, influenced by differences in material thickness, density, or chemical composition, allow for the precise identification of physical objects [21].
2. **Terahertz Imaging**: Unlike infrared and visible light, THz waves possess superior penetration capabilities, rendering common materials relatively transparent to THz

signals. This characteristic makes THz imaging particularly valuable for security screening applications, such as inspecting postal packages for concealed objects. It enables the scanning of envelopes, parcels, and small bags to identify potential hazards [22]. Additionally, THz radiation is non-ionizing and poses no known health risks to biological cells aside from heating. This safety profile makes it an attractive option for imaging the human body, where ionizing radiations like ultraviolet, X-rays, and gamma rays are unsuitable due to their significant health risks [23].

3. **Terahertz Positioning:** Future 6G and beyond systems are expected to deliver highly accurate positioning and localization capabilities for both indoor and outdoor environments, in addition to communication services. Devices equipped with THz sensing and imaging are anticipated to enable centimetre-level localization in virtually any setting [24]. Moreover, leveraging THz imaging for localization offers distinct advantages over other methods. THz imaging can accurately localize users in non-line-of-sight (NLoS) conditions, even when their signals to the base station undergo multiple reflections (e.g., multiple bounces). High-frequency localization techniques often rely on the concept of Simultaneous Localization and Mapping (SLAM) [25], where accuracy is enhanced by capturing high-resolution images of the environment—a capability that THz imaging excels at providing.

Of course, the physical characteristics of THz waves also present certain challenges in their applications, with propagation attenuation being the foremost issue. Since the wavelength of a THz wave is on the same order of magnitude as the dimensions of molecules in the atmosphere and human tissue, strong molecular absorption and particle scattering effects that are negligible in lower-frequency bands become significant [26]. Specifically, water vapour and oxygen molecules in the atmosphere can cause severe signal loss, reaching thousands of dB per kilometre in extreme cases. Beyond gaseous absorption by water molecules, liquid water droplets found in clouds, rain, snowflakes, and fog—can further attenuate signal strength, as their dimensions are comparable to the THz wavelength. Additionally, surrounding physical objects become sufficiently large relative to the THz wavelength to cause significant scattering, and ordinary surfaces are typically too rough to produce specular reflections. Consequently, THz waves are highly susceptible to blockage by buildings, furniture, vehicles, foliage, and even the human body.

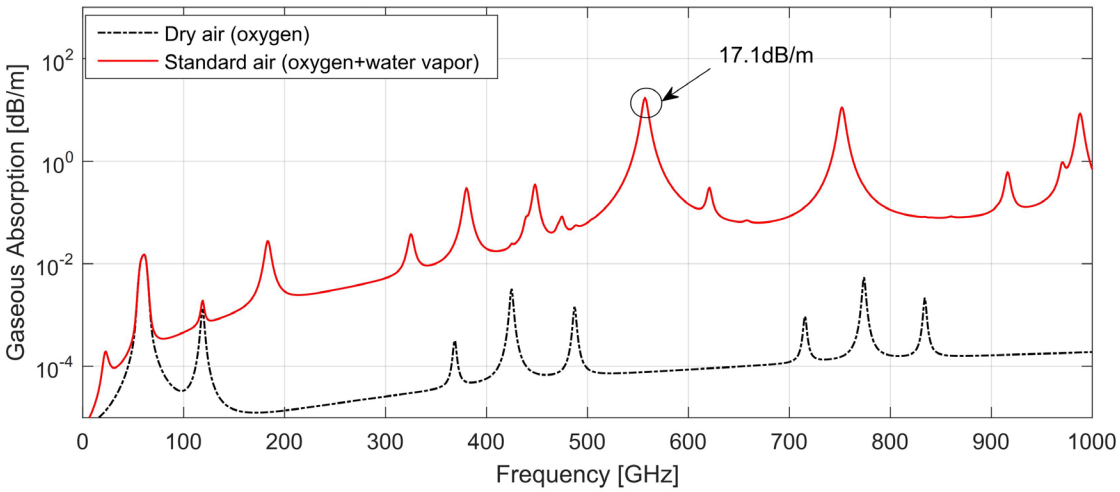

Fig. 1.2 Illustration of gaseous absorption from 1 GHz to 1000 GHz [27].

The atmospheric attenuation from 1 GHz to 1000 GHz is illustrated in Fig. 1.2. As illustrated, signals in the frequency range of 1-1000 GHz exhibit pronounced absorption peaks at certain specific frequency windows during atmospheric transmission. Notably, at approximately 560 GHz, atmospheric absorption reaches 17.1 dB/m. In contrast, atmospheric attenuation in the sub-6 GHz frequency range is less than 0.0001 dB/m. Clearly, atmospheric propagation attenuation is a significant limiting factor for communication in the THz frequency band.

1.2 Photonic generation of high-frequency RF signals

Due to the unique position of MMW and THz within the electromagnetic spectrum, researchers from the fields of electronics and photonics have converged to collaboratively address the technical challenges in this area.

In the realm of electronics, III-V semiconductor technologies, such as InP heterojunction bipolar transistors (HBTs), high electron mobility transistors (HEMTs), and GaAs-based Schottky diodes, have achieved room-temperature power generation ranging from 100 μW to mW, particularly at frequencies above 1 THz, nearly five times the levels achieved a decade ago [28-30]. Meanwhile, silicon-based integrated technology has enabled the development of complex phased arrays, imaging, and communication systems, with output power reaching up to 100 μW at 1 THz [31].

In recent years, photonic approaches for generating high frequency RF signals have become increasingly attractive. The core reasons include the ability to upconvert RF frequencies to optical frequencies, thereby offering much broader signal processing

bandwidth; the capability to transmit signals over low-loss optical fibres, which nearly eliminates the issue of high atmospheric attenuation at high frequencies; and the flexibility in designing and adjusting RF frequencies [32, 33]. Notable demonstrations include the generation of ultra-broadband signals [34], RF distribution and transport over fibre [35, 36], programmable microwave photonic filters [37, 38], and a photonics-enhanced radar system [39].

Currently, there are three primary methods for generating MMW and THz signals using photonics:

1. **Terahertz time-domain spectroscopy (THz-TDS)**: As illustrated in Fig. 1.3(a), the principle of THz-TDS begins with a femtosecond laser generating an optical pulse train, with each pulse split into two paths. One path directs the pulse to a THz emitter, such as a photoconductive antenna, where the optical pulse is converted into an ultrashort electromagnetic pulse. This pulse then propagates through free space and is focused onto an ultrafast detector, such as a low-temperature-grown GaAs photoconductive switch or an electro-optic crystal. The other portion of the pulse is sent to the detector after passing through a time-delay stage. The principle of a TDS system is the Fourier transform. After an ultrafast optical pulse passes through the THz emitter, it generates an electromagnetic pulse that radiates through space. As this pulse passes through a sample, its amplitude and phase are altered. By varying the time delay of the reference light, the system samples the electromagnetic wave after it has traversed the sample. The sample's spectral characteristics are then recorded through a Fourier transform. The system does not require an actual THz light source, typically, a mode-locked laser with a frequency of several hundred MHz and an optical pulse width of a few picoseconds is sufficient to produce a Fourier spectrum exceeding 2 THz. It is important to note that this method does not generate a pure MMW or THz frequency (as shown in Fig. 1.3(b)), but rather a series of transmitted (or reflected) signals through space. Therefore, this approach is better suited for characterising material properties rather than for communication purposes [40-42].

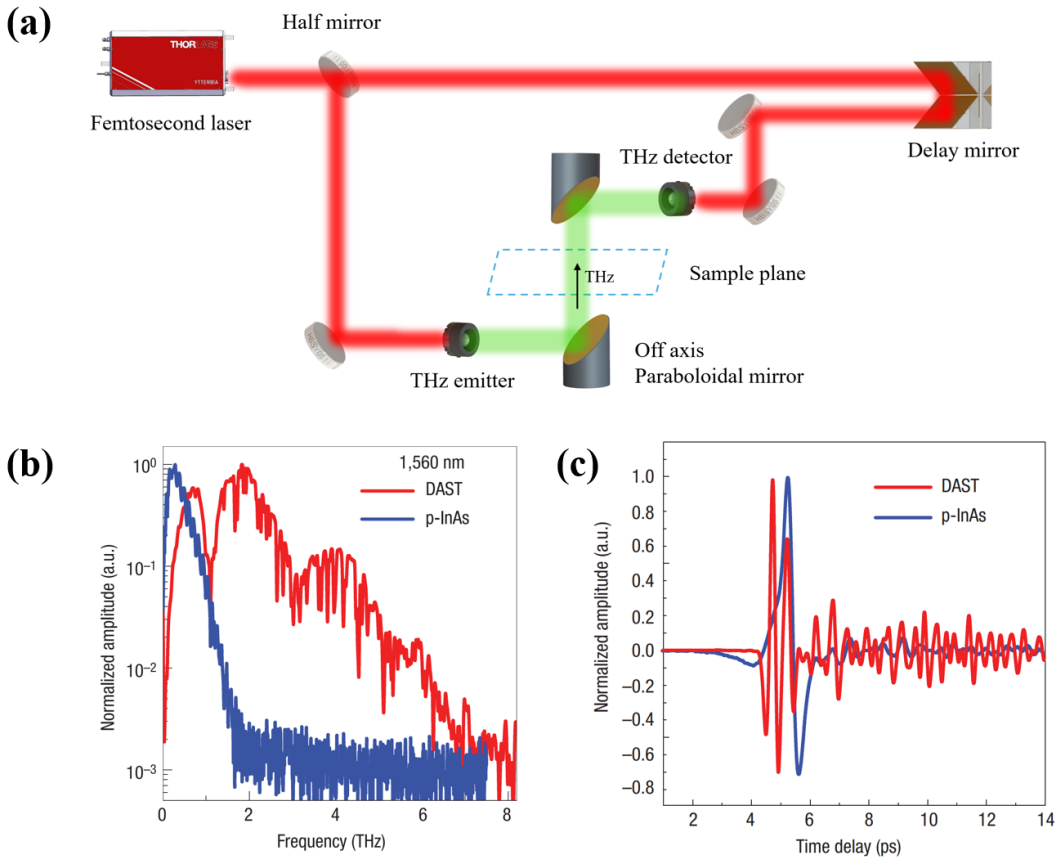

Fig. 1.3. (a) Typical set-up for THz-TDS, (b) corresponding Fourier-transformed spectra with nonlinear crystal DAST (diethylamino-sulfur tetrafluoride) and p-InAs as detector, respectively. (c) Examples of THz pulses emitted from p-InAs and DAST [43].

2. **Quantum cascade laser**: As shown in Fig. 1.4(a), in traditional semiconductor lasers, light is generated by the radiative recombination of conduction band electrons with valence band holes across the bandgap of the active material. In contrast, in quantum cascade lasers (QCL) (shown in Fig. 1.4(b)), electrons propagate through coupled quantum wells in a potential staircase, where the conduction band is split into several distinct sub-bands due to quantum confinement. The energy released during transitions between sub-bands is evidently lower than that of conduction-to-valence transitions, rendering this characteristic particularly suitable for long-wavelength excitation, such as those in the several terahertz frequency range [44-50]. Furthermore, by carefully designing the thickness of the quantum wells and barriers, as well as applying varying bias electric fields, the spacing between energy levels can be controlled. This, in principle, allows the device to operate at arbitrary wavelengths. Additionally, by integrating well-established grating and other technologies from semiconductor lasers into QCLs, precise frequency mode output

and mode-locked QCLs have now been achieved. Terahertz QCLs now are considered the only solid-state terahertz sources capable of providing well above milliwatt-level average optical power, which is crucial for imaging applications [51]. However, the practical operation of QCLs faces a significant limitation: temperature. It is currently understood that the operating temperature of all QCLs is restricted to within one to two times $h\nu/K_B$, where h is Planck's constant, ν is the photon frequency generated by the transition, and K_B is Boltzmann's constant. For example, QCLs operating at frequencies below 2 THz typically require temperatures lower than 80 K (-193°C) [52, 53]. This characteristic poses a significant barrier to the wider adoption of QCLs.

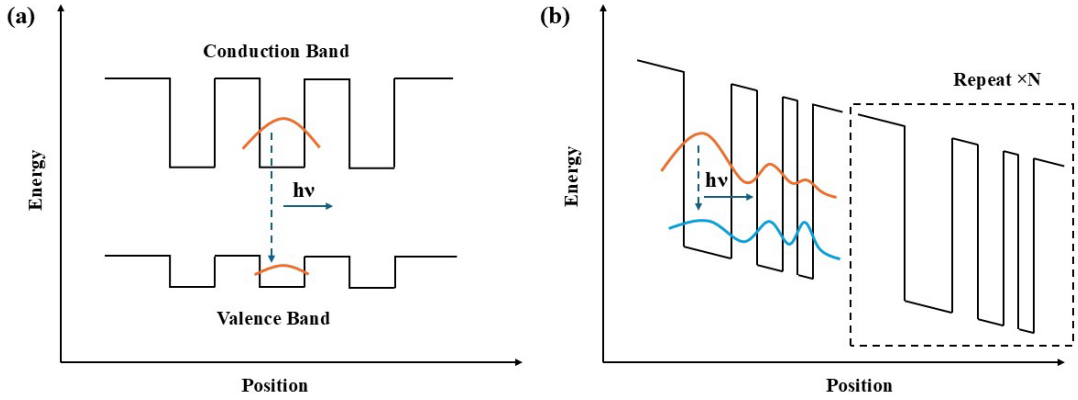

Fig. 1.4. Transition diagram of (a) quantum wells laser, (b) quantum cascade laser.

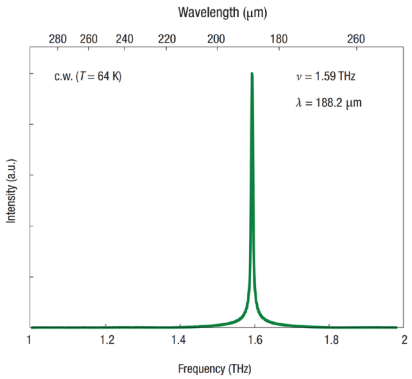

Fig. 1.5. A typical QCL output spectrum under continuous wave operation at 64K temperature [43].

3. **Integrated optical frequency division**: The principle of generating MMW using an optical frequency division (OFD) system involves first producing a stable frequency comb within an optical resonator through optical oscillation or nonlinear effects [54,

55]. Subsequently, an optical filter is used to select two or more optical modes from the comb, which are then heterodyned to produce a pure RF signal. Or similarly, the generated frequency comb can directly heterodyne with the optical signal from the original laser to produce an RF signal. This technology forms the foundation of optical atomic clocks and has led to the generation of the most precise microwave frequencies to date. Owing to the advancements in SOI (Silicon on insulator) and SiN (Silicon Nitride) platform integration technology and its exceptionally high-quality factor, the resulting frequency comb demonstrates ultra-low phase noise, achieving a level of -109 dBc/Hz at a 10 GHz frequency offset [56, 57]. Meanwhile, the development of SiN photonic integration technology, along with heterogeneous integration techniques, can significantly enhance the level of chip integration. As illustrated in the figure below, the integrated chip is reduced to a size comparable to just a few coins [58]. However, the operation of this integrated system still requires at least one high-power external optical pump, which limits its applicability in certain scenarios. Additionally, due to the inherent characteristics of optical frequency combs, as the division ratio increases, the signal's performance in terms of output power and phase noise deteriorates, the highest reported frequency to date is 226 GHz [59].

Fig. 1.6. Microscope image of integrated OFD chip [58].

1.3 The aim of this research

As previously mentioned, MMW and THz frequencies offer unique value in applications such as communication, sensing, and imaging. Although several solutions for generating MMW and THz have been proposed in both electronic and photonic domains, there are still limitations in practical applications. For example, THz-TDS systems cannot generate a single pure THz frequency; QCLs require additional cooling equipment during operation within the 0.1-2 THz frequency range; and OFD (Optical Frequency Division) systems are passive integrated chips that require external high-power pump sources.

This thesis presents a method based on III-V DFB (Distributed Feedback) semiconductor lasers. By designing the grating structure, the laser simultaneously emits two wavelengths, and MMW and THz signals are generated using the beat frequency principle. The experiment successfully demonstrated the generation of RF signals from 50 GHz to 1 THz. The chip designed and fabricated in this study features a high level of integration, requiring only a millimetre-scale resonant cavity to achieve dual-wavelength lasing, the resolution of the beat frequency design can reach 1 GHz. Furthermore, the thesis shows that by using optical injection or direct RF injection techniques, the linewidth of the generated MMW and THz signals can be reduced to as narrow as 1 Hz.

1.4 Thesis outline

The overall structure of this paper is as follows,

Chapter 1 provides a brief overview of the applications of MMW and THz, as well as the current methods for generating MMW and THz signals.

Chapter 2 begins by explaining the basic principles of beat frequency generation for RF signals. Then it presents the basic design approach for the device, which includes using the Coupled Mode Theory (CMT) and the Transfer Matrix Method (TMM) to design gratings that enable dual-wavelength lasing, as well as employing the Traveling Wave Model (TWM) based on rate equations to analyse the dynamic characteristics of the laser. The key innovation lies in the design of three different grating structures, which allow precise control of two lasing wavelengths, enabling the generation of various RF frequencies.

Chapter 3 provides a detailed description of each step involved in the device fabrication process. The grown III-V epitaxial wafers are processed into laser bars through a series of steps, including etching, metal deposition, insulation material deposition, thinning, annealing, and cleaving.

Chapter 4 presents the test results of the devices and their arrays based on the three different grating structures. First, spectral testing shows that the arrays achieve stable dual-wavelength lasing under appropriate current and voltage biases. The side-mode suppression ratio (SMSR) exceeds 30 dB, and the power difference between the two lasing modes is less than 1 dB. In the frequency spectrum tests, devices with frequencies below 75 GHz were observed using an electrical spectrum analyser after the optical signals were converted to electrical signals by a commercial high-speed photodetector (PD). For devices operating at 135 GHz and 150

GHz, their frequencies were directly extracted from the electro-absorption modulator (EAM) region of the device using a GSG probe and a G-band mixer. For devices operating at 300 GHz to 1 THz, their frequency was characterised using an autocorrelator and the power of the THz radiation was measured using a photoconductive antenna and a Golay cell detector.

Chapter 5 demonstrates a phase-locking technique: optical injection locking. When the device is under an injection-locked state, the RF linewidth is reduced from several hundred kHz to below 1 Hz. The resulting pure spectrum and extremely low phase noise make the device suitable for a wide range of applications.

Chapter 6 summarises the thesis and discusses potential future directions. It includes an overview of the main innovations and achievements of the study, the challenges the device faces in practical applications, and potential future developments that could enhance the device through further hybrid integration and packaging improvements.

Chapter 2: Theory and design

2.1 Optical beat frequency

Optical beat frequency refers to the phenomenon where two optical waves of slightly different frequencies interfere with each other, producing a beat frequency equal to the difference between their frequencies.

Two transmitted optical fields can be described by their electric fields,

$$\begin{cases} E_1(t) = A_1 \exp\left(\omega_1 t + \varphi_1\right) \\ E_2(t) = A_2 \exp\left(\omega_1 t + \varphi_2\right) \end{cases} \tag{2.1}$$

Where A_1, A_2 represent the amplitudes of the two light beams, ω_1, ω_2 represent their respective frequencies, and φ_1, φ_2 represent their initial phases. When the two optical signals intersect in space with matching polarization states, interference occurs. The electric field intensity after interference is the superposition of the two fields. Since the optical field intensity is proportional to the square of the electric field intensity, the resulting optical intensity $I(t)$ after beating can be expressed as:

$$\begin{aligned} I(t) &= \frac{c\epsilon_0}{2}\left(E_1(t) + E_2(t)\right)^2 \\ &= \frac{c\epsilon_0}{2}\{\frac{{A_1}^2+{A_2}^2}{2} + \frac{{A_1}^2}{2}\cos(2\omega_1 t + 2\varphi_1) + \frac{{A_2}^2}{2}\cos(2\omega_2 t + 2\varphi_2) \\ &+ A_1 A_2 \cos[(\omega_1 + \omega_2)\, t + (\varphi_1 - \varphi_2)] + A_1 A_2 \cos\left[(\omega_1 - \omega_2)t + (\varphi_1 - \varphi_2)\right]\} \end{aligned} \tag{2.2}$$

Where c is the speed of light, ϵ_0 is the dielectric constant of free space. Based on equation (2.2), it can be observed that the resulting optical field contains four frequency components: $2\omega_1$, $2\omega_2$, $\omega_1 + \omega_2$ and $\omega_1 - \omega_2$. For semiconductor lasers operating in the C-band (1530-1565 nm), their output optical frequency exceeds 100 THz (for instance, at 1550 nm, the frequency is 193.4 THz). Therefore, only the frequency component $\omega_1 - \omega_2$ can fall within the THz gap, while the other three frequencies, being far beyond the response bandwidth of photodetectors, will be effectively treated as DC components.

Fig. 2.1 illustrates the process of beat frequency. Fig. 2.1(a) and 2.1(b) show two sinusoidal waves at 193.4 THz and 194.4 THz, respectively. After the beat frequency process, the resulting waveform is shown in Fig. 2.1(c), which consists of a series of high-frequency waves with a low-frequency envelope (red curve). The period of the envelope is 1 ps, corresponding to the frequency difference of 1 THz.

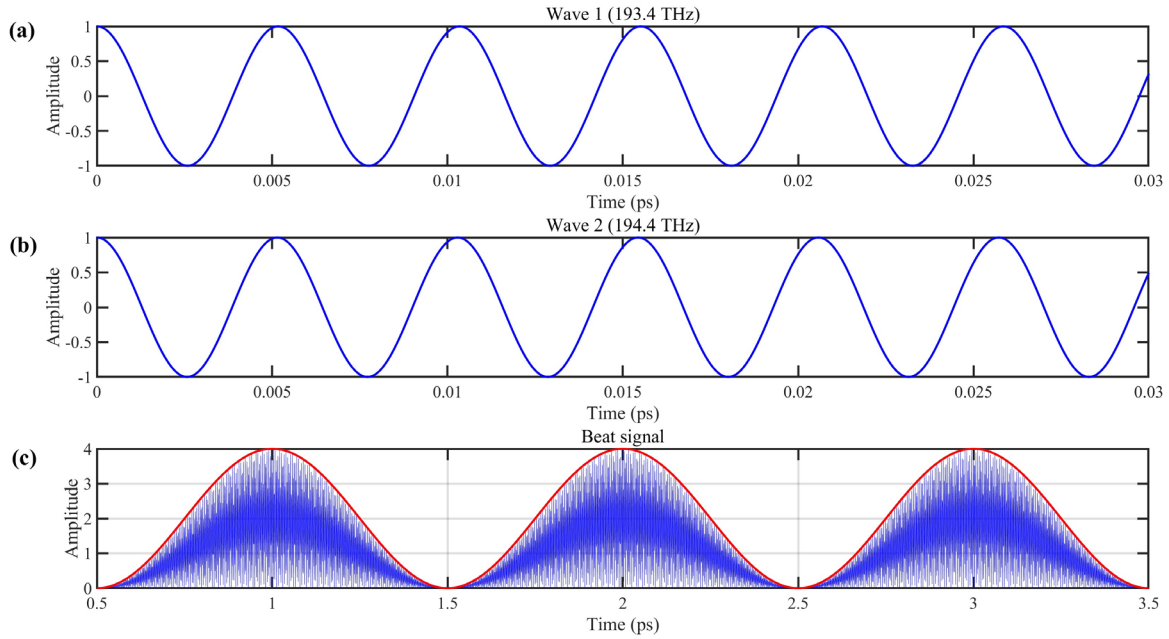

Fig. 2.1. A wave with a frequency of (a) 193.4 THz, (b) 194.4 THz, and (c) the beat waveform, the red curve shows the envelope.

Based on the above, generating MMW and THz signals requires the laser to emit two wavelengths simultaneously with a designable frequency difference, utilising the characteristics of optical beat frequency and PD.

2.2 Bragg grating and transfer matrix method

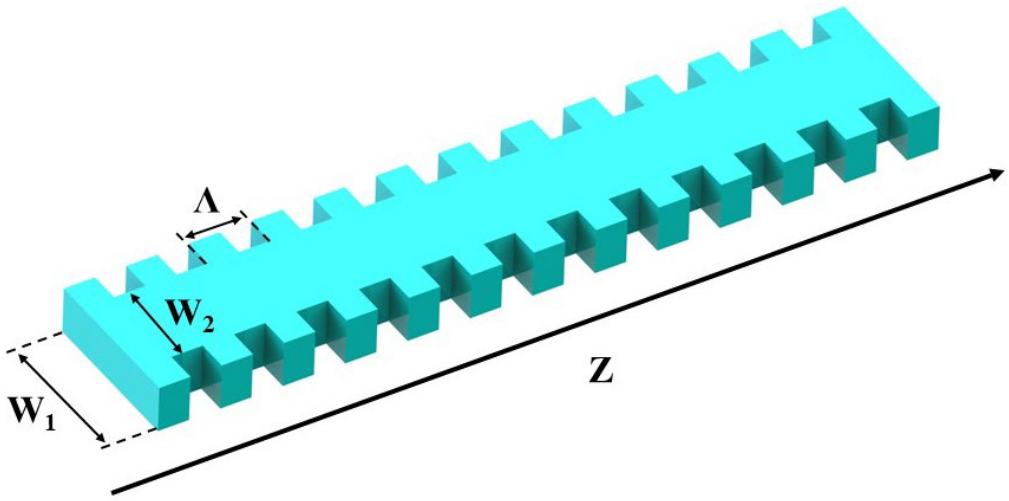

Fig. 2.2. Schematic diagram of sidewall Bragg grating.

For semiconductor lasers, introducing a periodic refractive index variation, such as Bragg grating, within the resonant cavity can effectively select the output wavelength of the device. This type of device is known as a distributed feedback (DFB) semiconductor laser [60-62]. The analysis of Bragg gratings is typically based on coupled mode theory (CMT) [61, 63], and the transfer matrix method (TMM) [64-67] is an effective approach for calculating the propagation characteristics of light within Bragg gratings. Fig 2.2 illustrates the structure of a sidewall Bragg grating, which is commonly used in DFB lasers, as well as in SOI and SiN waveguides [68-71]. The principle involves etching periodic grooves on the sidewalls, causing the waveguide width to vary periodically in the Z direction, which in turn induces a periodic perturbation in the refractive index.

In the case of one-dimensional analysis, where light propagates along the z-axis, the forward (A) and backward (B) propagating waves along the z-axis can be represented as follows,

$$\begin{aligned} A(z) &= A_0 \exp(i\beta z) \\ B(z) &= B_0 \exp(-i\beta z) \end{aligned} \tag{2.3}$$

Here, $A(z)$ and $B(z)$ represent the amplitudes of the forward and backward waves at position z, respectively. The propagation constant β is given by,

$$\beta = \frac{2\pi}{\lambda} n_{eff} \tag{2.4}$$

n_{eff} is the effective refractive index of the mode, and λ is the wavelength of the light in vacuum.

In Bragg grating, due to the periodic modulation of the refractive index, coupling occurs between the forward and backward propagating modes. This coupling can be described by the coupled-mode equations [61],

$$\begin{aligned} \frac{dA(z)}{dz} &= i\kappa(z)B(z)exp(-i2\beta z) \\ \frac{dB(z)}{dz} &= i\kappa^*(z)A(z)exp(i2\beta z) \end{aligned} \tag{2.5}$$

Where $\kappa(z)$ is the grating coupling coefficient. In most cases, due to the small amplitude of refractive index modulation within the grating period, the grating coupling coefficient can be approximated as,

$$\kappa(z) = \frac{\pi \Delta n(z)}{2 n_{eff} \Lambda} \tag{2.6}$$

Where Λ is the grating period and $\Delta n(z)$ is the index modulation amplitude. It is important to note that once the grating period is determined, the Bragg wavelength λ_b, at which reflection resonance occurs, can also be precisely determined $\lambda_b = 2n_{eff}\Lambda$. Substituting into Equation 2.4, the propagation constant under the Bragg condition is $\beta_0 = \frac{\pi}{\Lambda}$.

By applying the rotated wave approximation (RWA), the coupled-mode equations are simplified to:

$$\begin{aligned} \frac{dA(z)}{dz} + i\Delta\beta A(z) &= i\kappa(z)B(z) \\ \frac{dB(z)}{dz} - i\Delta\beta B(z) &= i\kappa^*(z)A(z) \end{aligned} \tag{2.7}$$

Here, $\Delta\beta = \beta - \beta_0$ represents the deviation of the propagation constant from the Bragg condition.

Equation 2.7 can be converted into matrix form to represent the coupled-mode equations more compactly. The matrix form is typically written as,

$$\frac{d}{dz}\begin{pmatrix} A(z) \\ B(z) \end{pmatrix} = i\begin{pmatrix} \Delta\beta(z) & \kappa(z) \\ \kappa^*(z) & -\Delta\beta(z) \end{pmatrix}\begin{pmatrix} A(z) \\ B(z) \end{pmatrix} \tag{2.8}$$

Considering that the values of $\Delta\beta$ and κ are determined solely by the effective refractive index n_{eff}, the grating modulation period Λ, and the local refractive index modulation amplitude $\Delta n(z)$, this illustrates that the coupling between the forward and backward modes is essentially due to the distributed reflection caused by the variation in refractive index along the z direction.

Define the transfer matrix $T(z)$ so that,

$$\begin{pmatrix} A(z) \\ B(z) \end{pmatrix} = T(z)\begin{pmatrix} A(0) \\ B(0) \end{pmatrix} \tag{2.9}$$

The transfer matrix $T(z)$ can be derived in its exponential form as,

$$T(z) = \exp\left[i\begin{pmatrix} \Delta\beta(z) & \kappa(z) \\ \kappa^*(z) & -\Delta\beta(z) \end{pmatrix}z\right] \tag{2.10}$$

Considering that $\Delta\beta(z)$ and $\kappa(z)$ are constants locally, the analytical solution for the transfer matrix $T(z)$ can be expressed as,

$$T(z) = \begin{pmatrix} \cos(\gamma z) - i\Delta\beta(z)sin(\gamma z) & -i\frac{\kappa(z)}{\gamma}\sin(\gamma z) \\ i\frac{\kappa^*(z)}{\gamma}\sin(\gamma z) & \cos(\gamma z) + i\Delta\beta(z)sin(\gamma z) \end{pmatrix} \tag{2.11}$$

Where $\gamma^2 = \Delta\beta^2 + |\kappa|^2$.

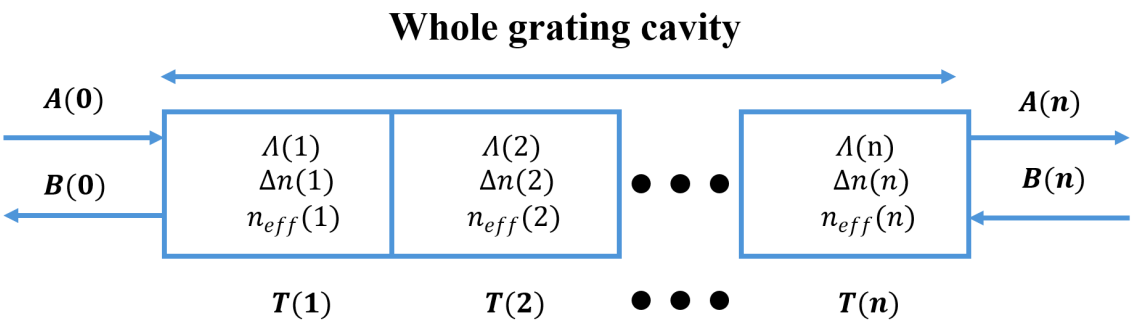

Fig. 2.3. Schematic of TMM.

As shown in Fig. 2.3, the total transmission matrix can be expressed as the product of each discrete matrix.

$$T_{total} = T_n \cdot T_{n-1} \cdot T_{n-2} \cdots T_2 \cdot T_1 \tag{2.12}$$

$$\begin{pmatrix} A(n) \\ B(n) \end{pmatrix} = T_{total} \begin{pmatrix} A(0) \\ B(0) \end{pmatrix} \tag{2.13}$$

The primary information is the overall reflection and transmission of the grating, which is,

$$R = |\frac{B(0)}{A(0)}|^2, T = |\frac{A(n)}{A(0)}|^2 \tag{2.14}$$

Their relationship with the transmission matrix T_{total} is,

$$R = |\frac{T_{21}}{T_{22}}|^2, T = |\frac{\det T}{T_{22}}|^2 \tag{2.15}$$

Considering that the entire physical model does not introduce absorption and radiation, the entire cavity is lossless, therefore $\det T \equiv 1$.

In the passive simulation of gratings, in addition to R and T, group delay is also a crucial parameter. It reflects the time delay experienced by light of a specific wavelength due to reflections and refractions within the cavity. For the DFB laser, the longer the light with a specific wavelength remains within the cavity, the larger number of photons that can be stimulated to emit radiation. Group delay is the negative derivative of phase with respect to frequency,

$$\tau(\omega) = -\frac{\varphi(\omega)}{d\omega} = \frac{d}{d\omega} arg(T_{11}(\omega)) \tag{2.16}$$

Where ω is the frequency of the input light.

Furthermore, in a refractive index-coupled DFB laser, the photon density at each point within the cavity along the z-direction can be expressed as [72-74],

$$P(z) \approx \frac{2\epsilon_0 \Delta n(z) n_g \lambda}{hc} (|A(z)|^2 + |B(z)|^2) \quad (2.17)$$

Where h is the Plank's constant, and n_g refers to the group index. Based on this formula, the normalized photon distribution within the entire cavity can be obtained by calculating the normalized electric field intensity at each given z position.

2.3 Three novel grating structures for achieving dual-wavelength lasing

2.3.1 Two π phase shifts grating with equivalent chirp technology

Typically, inserting a π-phase shift in the middle of a uniform Bragg grating introduces a transmission peak at the Bragg wavelength in the reflection spectrum, thereby ensuring that the laser operates in a single-wavelength mode [75, 76]. It is easy to consider whether inserting two π-phase shifts could introduce two transmission peaks within the reflection spectrum, thereby enabling dual-wavelength lasing. Fig 2.4 shows the refractive index modulation of the uniform grating (blue curve), the π-phase shifted grating (red curve), and the grating with two π-phase shifts located at 1/3 and 2/3 of the cavity length (black curve). The refractive index modulation along the z dimension $n(z)$ of the grating with two π-phase shifts can be expressed by Equation 2.18.

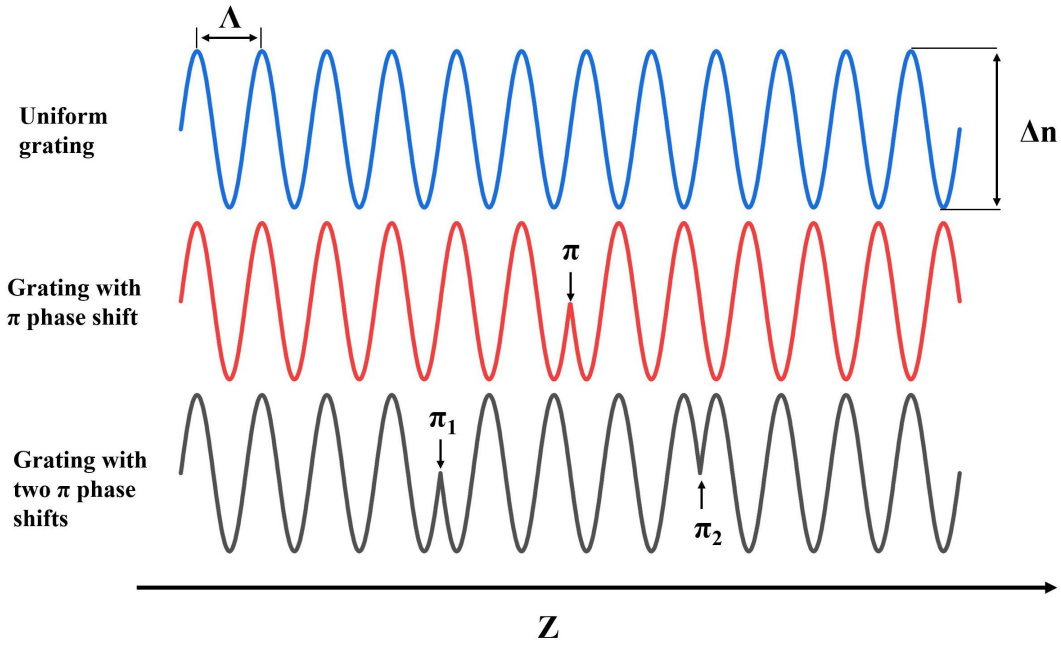

Fig. 2.4. Schematic of (a) uniform Bragg grating, (b) Bragg grating with π phase shift in the middle of the cavity, (c) Bragg grating with two π phase shifts symmetrically distributed at 1/3 and 2/3 of the cavity length.

$$n(z) = \begin{cases} \frac{1}{2}\Delta n(z)\sin\left(\frac{2\pi}{\Lambda}z\right) + c.c & (z \le \frac{1}{3}L) \\ \frac{1}{2}\Delta n(z)\sin\left(\frac{2\pi}{\Lambda}z + \pi\right) + c.c & (\frac{1}{3}L < z \le \frac{2}{3}L) \\ \frac{1}{2}\Delta n(z)\sin\left(\frac{2\pi}{\Lambda}z + 2\pi\right) + c.c & (\frac{2}{3}L < z) \end{cases} \quad (2.18)$$

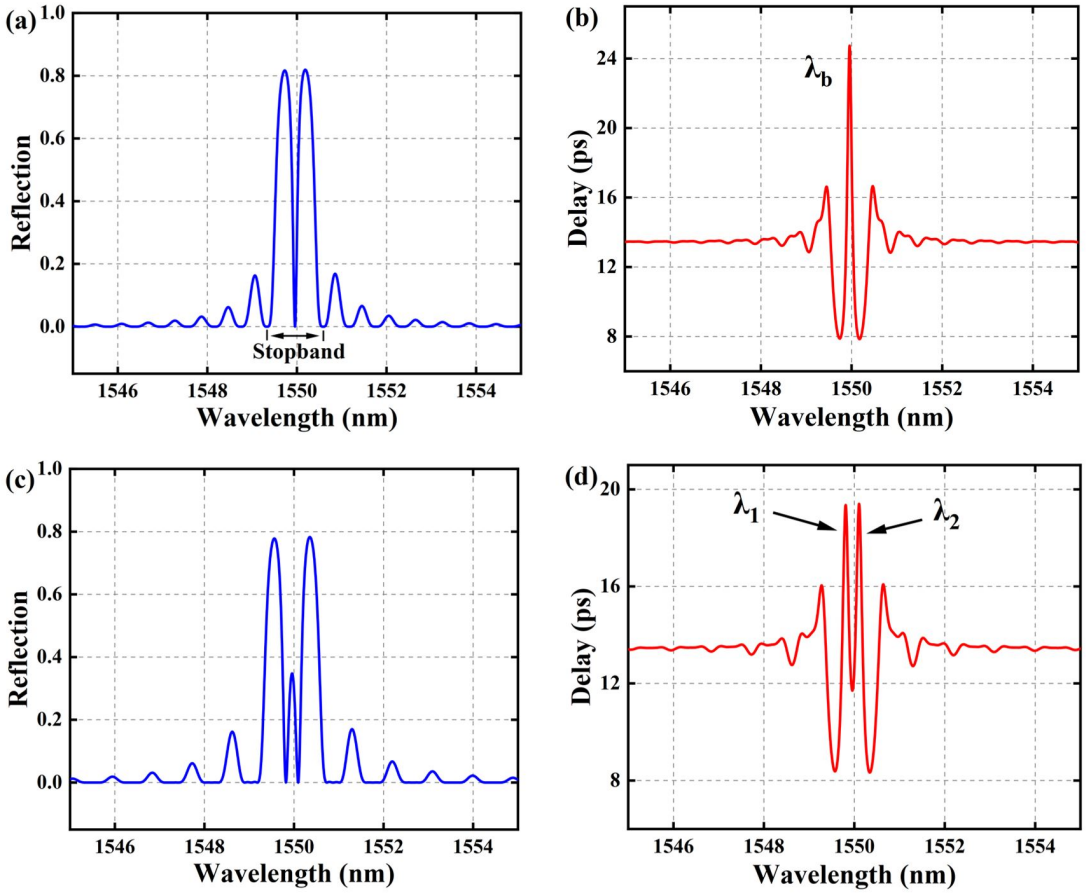

Fig. 2.5. Reflection spectrum (a) and time delay spectrum (b) of uniform grating with a π phase shift at the middle of the cavity. Reflection spectrum (c) and time delay spectrum (d) of the grating with two π phase shifts symmetrically distributed at 1/3 and 2/3 of the cavity length.

Where $\Delta n(z)$ is the amplitude of the refractive index modulation, Λ is the grating period, and $c.c$ represents the DC component of the refractive index. Using the TMM algorithm, the reflection spectra and time delay spectra for both a single π phase shift and two π phase shifts structures are calculated. Table 2.1 presents the simulation parameters.

Table 2.1 Simulation parameters

Type	Cavity length L (μm)	Δn	n_{eff}	Λ (nm)	Phase shift position
Single π phase shift	1000	0.0008	3.2	242	0.5L
Two π phase shifts	1000	0.0008	3.2	242	1/3L & 2/3L

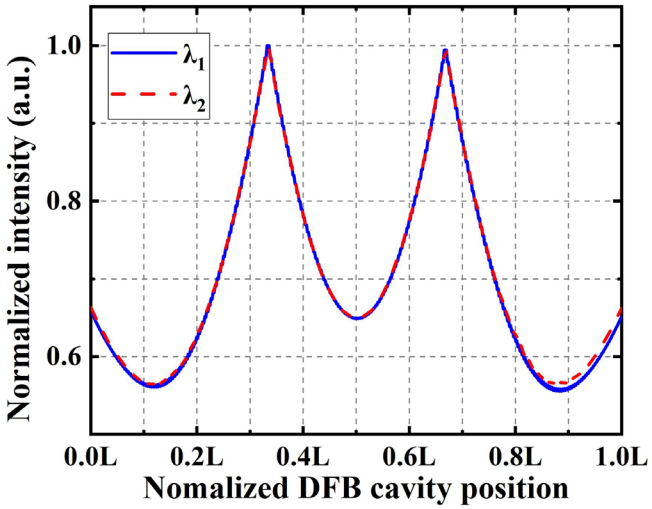

Fig. 2.6. Normalized photon distribution of λ_1 and λ_2 of uniform grating with two π phase shifts.

In fact, according to simulation results, symmetrically introducing two π phase shifts within the cavity indeed enable this grating structure to generate two lasing modes. As shown in Fig 2.5 (a), for a structure with a single π-phase shift, a transmission peak appears at the Bragg wavelength within the stopband of the grating's reflection spectrum. This corresponds to the longest delay at that wavelength (λ_b) in the time delay spectrum (Fig. 2.5(b)), making it the most potential wavelength to lase. Note that the stopband here refers to the distance between the two zeros flanking the maximum reflection window. When two π phase shifts are introduced within the cavity, as shown in Fig 2.5(c), two transmission peaks appear within the reflection stopband. The corresponding time delay spectrum exhibits two peaks (λ_1 and λ_2) as well, indicating the presence of two potential lasing modes in this structure.

However, the spatial distribution of photons for the two wavelengths in this structure reveals a problem: mode competition. As observed in Fig 2.6, the photon distributions for the two potential lasing wavelengths within the cavity are completely identical. Considering that the DFB laser is essentially a gain cavity, this could easily lead to a "winner-takes-all"

situation, finally affecting the simultaneous lasing of both wavelengths. This issue can be addressed by applying linear chirp to the grating. Chirp refers to the modulation of the grating period. Under the grating chirp, the grating period varies with the position along the cavity (z dimension),

$$\Lambda(n) = \Lambda(1) + C_r \cdot (n-1) \tag{2.19}$$

Here, n is the grating order, and C_r is the chirp rate, defined as the ratio of the difference between the periods of the last and the first grating to the cavity length L, $C_r = \frac{\Lambda(last)-\Lambda(1)}{L}$. As shown in Fig. 2.7, it is important to note that the chirp here is actually discrete, meaning that the change in grating period occurs only between adjacent complete grating periods, rather than within a single period. Since the Bragg wavelength is related to the grating period when the effective refractive index n_{eff} is constant, applying linear chirp to the grating period effectively alters the spatial position of the equivalent reflection for different wavelengths.

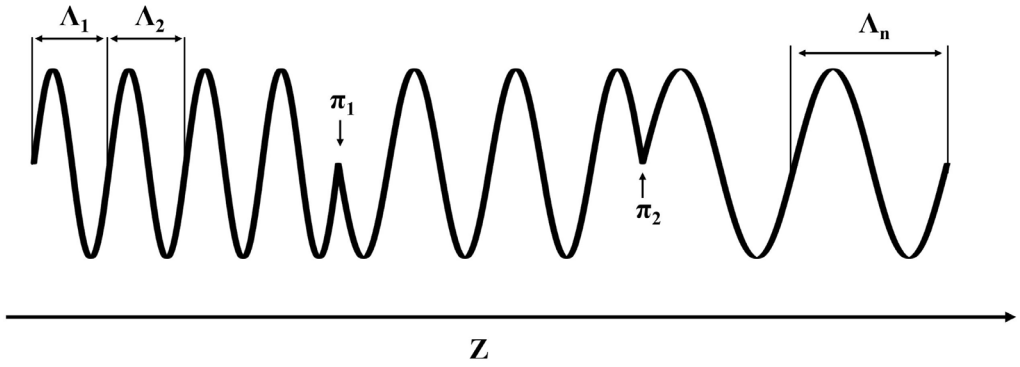

Fig. 2.7. Schematic of conventional chirped grating with two π phase shifts symmetrically distributed at 1/3 and 2/3 of the cavity length.

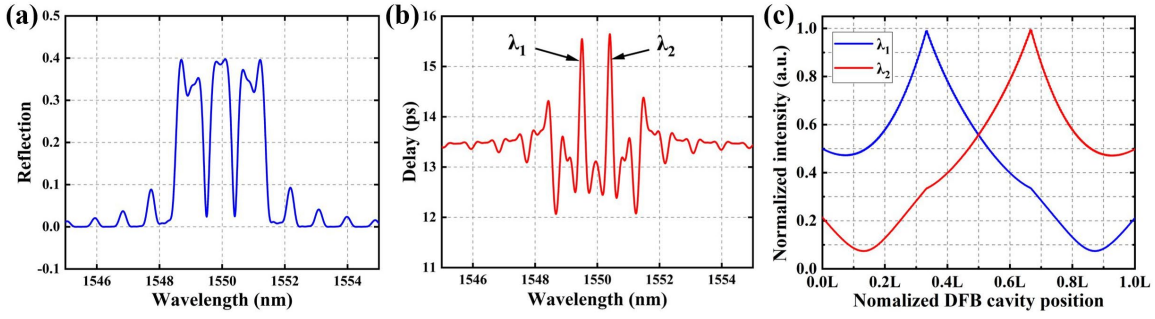

Fig. 2.8. Simulation results of conventional chirped grating with two π phase shifts (a) reflection spectrum, (b) delay spectrum, (c) photon distribution.

As shown in Fig 2.8 (a) and (b), when the chirp rate is 0.3 nm/mm, meaning the grating period varies from 241.85 nm to 242.15 nm, the reflection and delay spectra remain two

lasing wavelengths. Meanwhile, as shown in Fig. 2.8 (c), the two photons become significantly separated in space, which helps to suppress mode competition. In the simulation, the other parameters are consistent with those in Table 2.1. It is noted that under this level of chirp, the maximum reflection decreases from 0.78 (Fig 2.5 (c)) to 0.4 (Fig 2.8 (a)), indicating that the chirp process weakens the grating. Therefore, the chirp rate needs to be controlled within a certain range.

A more pressing issue is that the grating period changes by only 0.25 nm throughout the entire chirp process. Even with advanced electron-beam lithography (EBL) [77-79], the maximum pattern resolution is typically around 0.5 nm, which means that this chirp process cannot be practically implemented. This issue can be resolved through equivalent chirp technology.

First, a periodic phase modulation is applied to the uniform Bragg grating, dividing it into four equally spaced sections within one period P, with a π/2 phase shift between each adjacent section. The schematic is shown in Fig 2.9, and this type of phase modulation is referred to as four phase-shifted (4PS) Bragg grating.

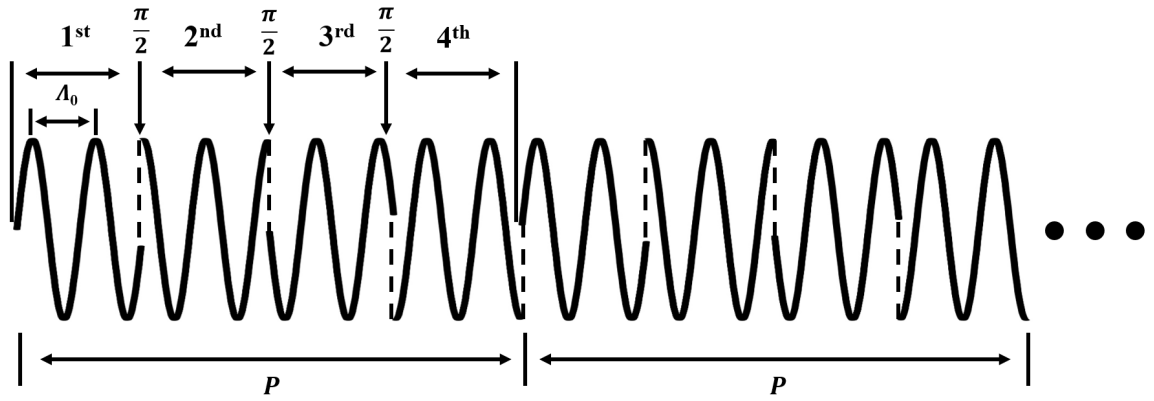

Fig. 2.9. Schematic of four phase-shifted Bragg grating.

In 4PS, the refractive index modulation can be expressed as,

$$n(z) = \frac{1}{2}\Delta n(z)\sin\left(\frac{2\pi}{\Lambda_0}z + \varphi(z)\right) + c.c \tag{2.20}$$

To differentiate it from the discussion later, the seed grating period here is Λ_0, and $\varphi(z)$ within each period P is given by,

$$\varphi(z) = \begin{cases} 0 & (0 < z < \frac{1}{4}P) \\ \frac{1}{2}\pi & (\frac{1}{4}P < z < \frac{2}{4}P) \\ \pi & (\frac{2}{4}P < z < \frac{3}{4}P) \\ \frac{3}{2}\pi & (\frac{3}{4}P < z < P) \end{cases} \tag{2.21}$$

Similar to a conventional sampled grating [80-82], this periodic phase modulation also generates multiple reflection channels in the reflection spectrum, with the Fourier coefficient of the mth order channel given by,

$$F_m = \frac{1}{P}\int_0^P \varphi(z) \cdot \exp\left(\frac{i2m\pi}{P}z\right) dz \tag{2.22}$$

After calculating the Fourier coefficients for integer values of m between -4 to 4, the results show that $F_1 = 0.9$, $F_{-3} = 0.3$, and $F_m = 0$ for all other cases [83]. This indicates that in the 4PS structure, only the +1st and -3rd channels exhibit reflection, with the intensity of the +1st channel being 0.9 times that of a uniform Bragg grating.

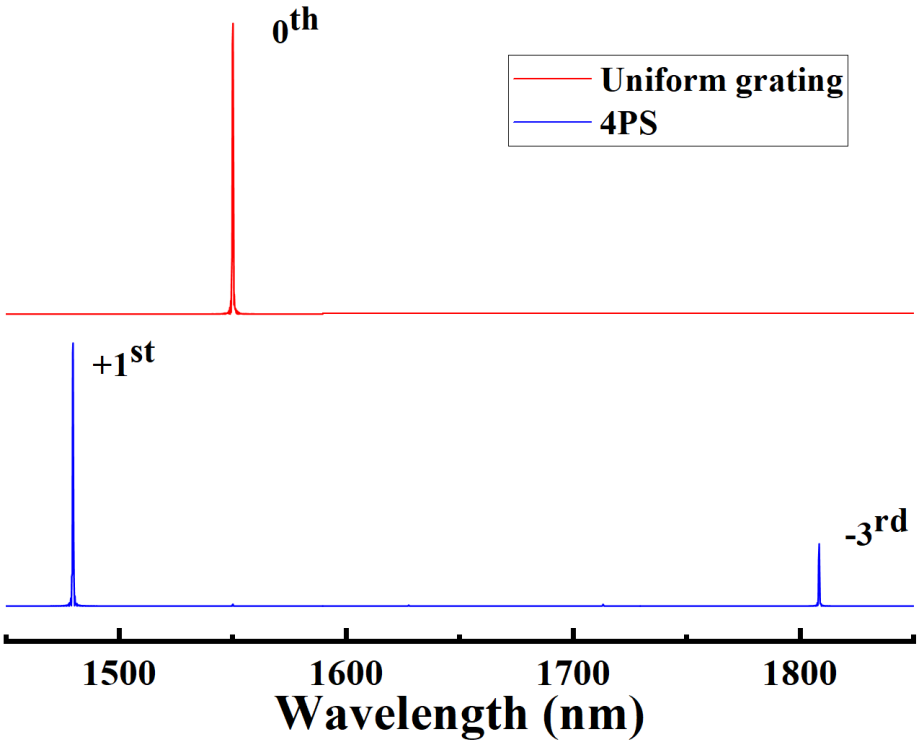

Fig. 2.10. Calculated reflection spectra of uniform grating and 4PS.

Fig. 2.10 shows the reflection spectra of the uniform grating and the 4PS grating. It can be observed that the reflection window of the uniform grating appears at the Bragg wavelength (1550 nm), while the reflection of the 4PS grating primarily occurs in the +1st channel, with a weaker reflection in the -3rd channel which corresponds to the results

calculated by Equation 2.22. During the simulation, Λ_0 is 242 nm and the modulation period P is set to 4.5 μm.

The wavelength of the +1st channel λ_{+1} is determined by the phase modulation period P and the seed grating period Λ_0,

$$\begin{cases} \Lambda_{+1} = \frac{P \cdot \Lambda_0}{P + \Lambda_0} \\ \lambda_{+1} = 2n_{eff}\Lambda_{+1} \end{cases} \tag{2.23}$$

Typically, since the material gain spectrum of the laser is around 1550 nm, Λ_0 is set to about 257 nm, while P is set to approximately 4.5 μm, making the +1st channel near 1550 nm. In practical design, Λ_0 is normally kept constant, and the position of the +1st channel is adjusted by varying the micrometer-scale P.

For a uniform Bragg grating, the change rate of the Bragg wavelength with respect to the grating period Λ_0 can be expressed as,

$$\frac{d\lambda_b}{d\Lambda_0} = 2n_{eff} \tag{2.24}$$

That is, a 1 nm change in the seed grating period will result in a 6.4 nm shift in the Bragg wavelength (assuming n_{eff} is 3.2).

In the 4PS structure, the change rate of the +1st channel wavelength with respect to the modulation period P is,

$$\frac{d\lambda_{+1}}{dP} = \frac{2n_{eff}}{(\frac{P}{\Lambda_0}+1)^2} \tag{2.25}$$

Since P is typically an order of magnitude larger than Λ_0, $\frac{d\lambda_{+1}}{dP} \ll \frac{d\lambda_b}{d\Lambda_0}$. For example, when P=4.5 μm, Λ_0=257 nm and n_{eff}=3.2, then $\frac{d\lambda_{+1}}{dP}$=0.0187, significantly smaller than in the uniform grating structure. Therefore, in the 4PS structure, grating chirp can be equivalently achieved by modulating the phase modulation period P while keeping Λ_0 constant. Moreover, the chirp rate can be amplified to a manageable range, for example, scaling the conventional Bragg grating chirp rate of 0.3 nm/mm to an equivalent 100 nm/mm, significantly reducing the fabrication difficulty.

Similarly, two π-phase shifts are introduced at 1/3 and 2/3 of the cavity length to enable dual-wavelength lasing in the +1st channel. Fig. 2.11 shows the simulation results for the equivalently chirped 4PS. Fig. 2.11(a) and (b) respectively display the two transmission peaks within the +1st channel and the two wavelengths in the time delay spectrum. Fig. 2.11

(c) illustrates that, in this structure, the photon distributions of λ_1 and λ_2 are spatially separated within the cavity. Furthermore, since chirp alters the reflection wavelengths of the cavity (by introducing dispersion) [65], varying the chirp rate can also adjust the spacing between λ_1 and λ_2, thereby changing the beat frequency. The simulation parameters are provided in Table 2.2.

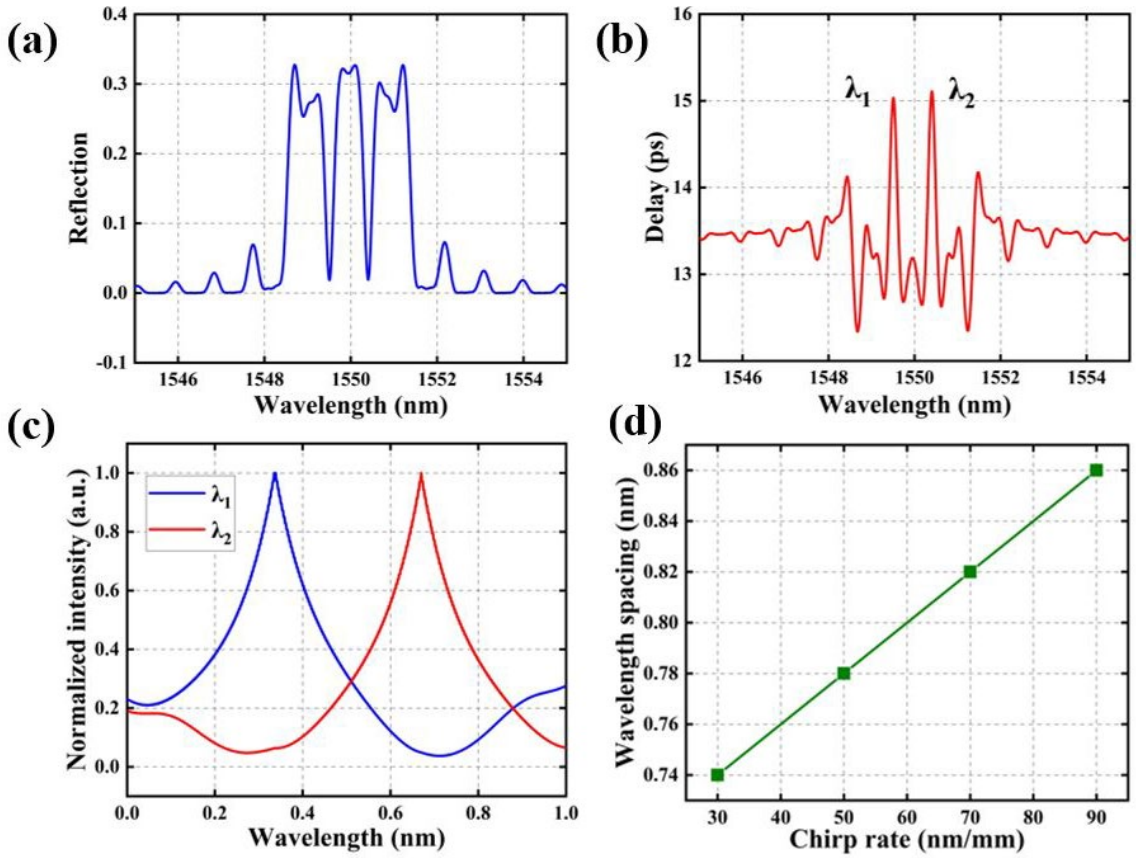

Fig. 2.11. Simulation results of chirped 4PS structure with two π phase shifts (a) reflection spectrum, (b) delay spectrum, (c) photon distribution along the cavity, (d) wavelength spacing versus chirp rate.

Table 2.2 Simulation parameters of chirped 4PS

Parameter	value
Cavity length L	1000 μm
Refractive index n_{eff}	3.2
Seed grating period Λ_0	242 nm
Sampling period P	4.5 μm
Chirp rate C_r	100 nm/mm
Index modulation amplitude Δn	0.0008
π Phase shifts positions	1/3 L & 2/3 L

In summary, chirp in the 4PS structure is equivalently achieved by varying the phase modulation period P, significantly reducing the fabrication difficulty. The introduction of two π phase shifts at symmetric positions within the cavity allows the grating to filter out two potential lasing wavelengths, and different chirp rates can be set to adjust the beat frequency. Therefore, two π phase shifts with equivalent chirp is one of the grating configurations used in this work to achieve high-frequency RF signals generation.

2.3.2 Sidewall grating with lateral modulation of the grating coupling coefficient

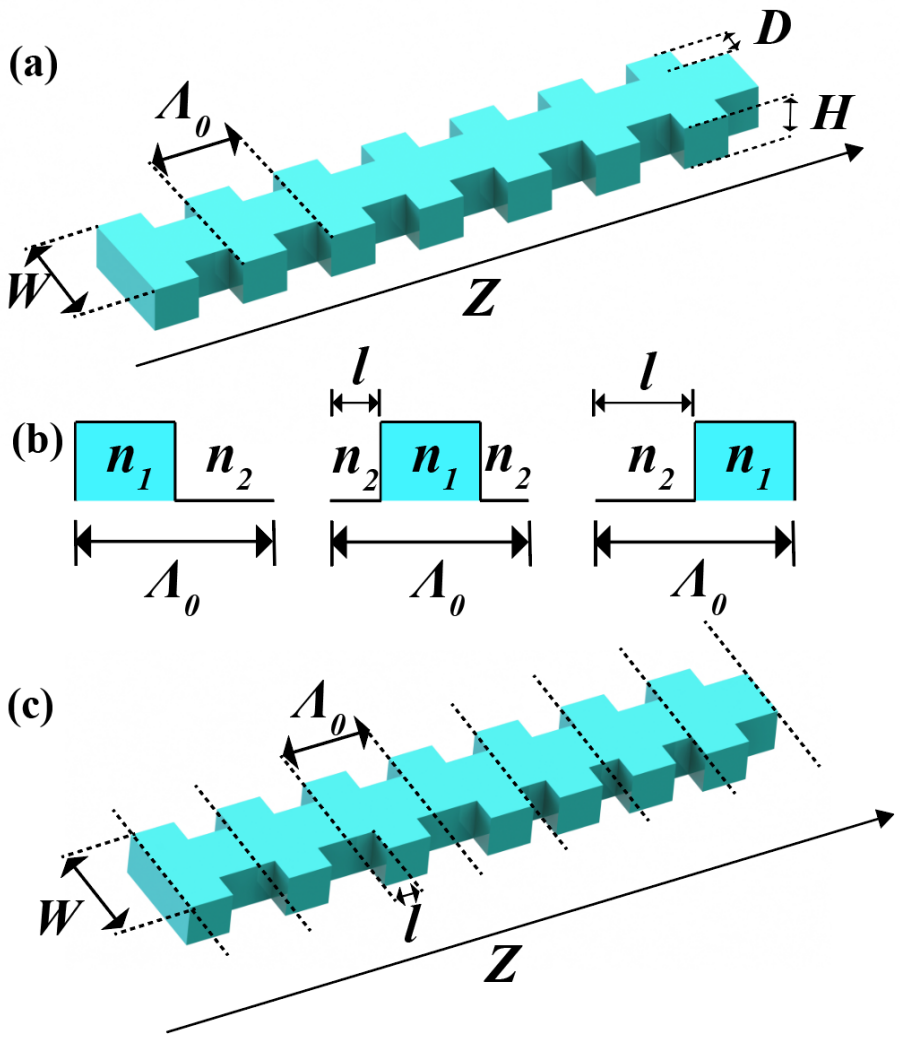

Fig. 2.12. Schematic of (a) uniform sidewall grating, (b) grating misalignment modulation, and (c) sidewall grating with alignment modulation.

In the scheme introduced in the previous section, the introduction of two π phase shifts creates two transmission peaks within the reflection stopband, leading to dual-wavelength lasing. Additionally, transmission peaks can also be constructed using the reflection stopband and the sidelobes on either side. In this subsection, a scheme is proposed to achieve

dual-wavelength lasing by controlling the degree of misalignment on both sides in each period of the sidewall grating, thereby modulating the distribution of the grating coupling coefficient along the z-dimension and amplifying the sidelobes on either side of the reflection stopband.

In a uniform sidewall grating, the gratings on either side of the sidewall have the same period Λ_0, the same lateral etch recess depth D and the corrugations on both sides are completely symmetrical as shown in Fig. 2.12(a). Each grating period comprises two refractive index segments n_1 and n_2; these are located on the left and right sides of the waveguide and the high index segments on either side are in perfect alignment (Fig. 2.12(a)).

However, the position of the n_1 segment in each grating period can be changed while keeping the grating period and duty cycle the same. Here, the variable alignment factor l is used to describe the relative positions of the n_1 segment in one grating period (Fig. 1(b)) and its value is the length from the start of the grating period to the start of the n_1 segment.

Fig. 2.12(b) shows schematics of a grating period with l = 0, $\Lambda_0/4$ and $\Lambda_0/2$ respectively. In the grating structure proposed here, one sidewall has a uniform Bragg grating and the other sidewall has a grating whose alignment with the uniform grating is modulated along the device. The two gratings have the same period Λ_0 and 50% duty cycle but on one sidewall l is modulated along the cavity as shown in Fig. 2.12(c). As l varies along the cavity, the degree of alignment of the gratings on the two sidewalls changes, therefore κ is modulated accordingly [84]. The relationship between κ and the variable alignment factor l can be expressed as [84],

$$\kappa(z) = \kappa_0 \cos\left(\frac{\pi \cdot l(z)}{\Lambda_0}\right) \tag{2.26}$$

where κ_0 is the grating coupling coefficient when the gratings on both sides have no misalignment (i.e., $l = 0$), and $l(z)$ describes the l distribution along the cavity (i.e., in the z-dimension). Equation 2.26 shows that the modulation in κ along the cavity can be determined by $l(z)$.

Then, if $l(z)$ is designed to be,

$$l(z) = \frac{\Lambda_0}{\pi} \cdot \arccos\left[1 - \exp\left(\frac{-4 \cdot ln2 \cdot (z - L/2)^2}{(L/3)^2}\right)\right] \tag{2.27}$$

where L is the cavity length, the normalized κ distribution along the cavity is,

$$\kappa(z) = 1 - \exp\left[\frac{-4 \cdot ln2 \cdot (z - L/2)^2}{(L/3)^2}\right] \tag{2.28}$$

As a result, $\kappa(z)$ exhibits an inverse Gaussian distribution within the cavity. Fig. 2.13 shows the $l(z)$ and $\kappa(z)$ distribution along the cavity. At the middle of the cavity (i.e., $z = 0.5L$), l reaches a maximum value of $0.5\Lambda_0$, which means the gratings on both sides of the ridge waveguide are completely misaligned and the normalized κ reaches its minimum value.

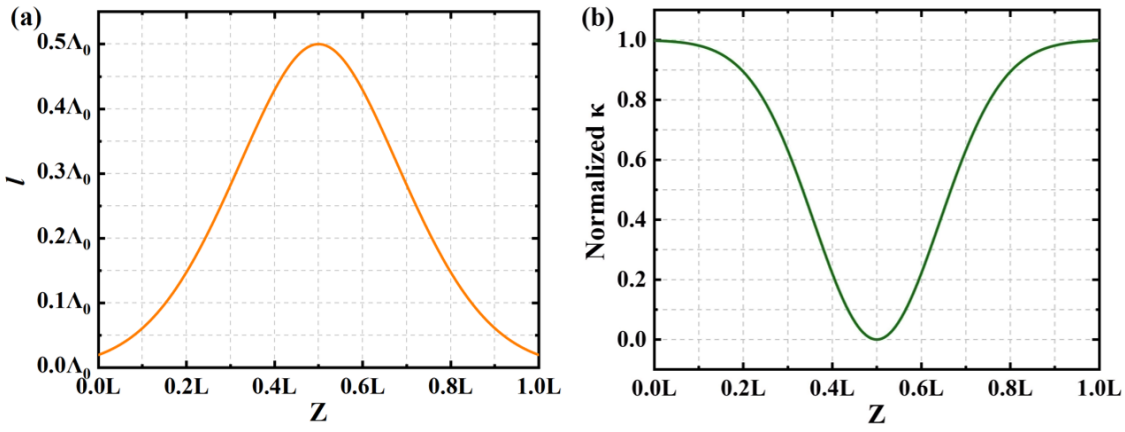

Fig. 2.13. The distribution of (a) variable alignment factor l and (b) κ along the cavity.

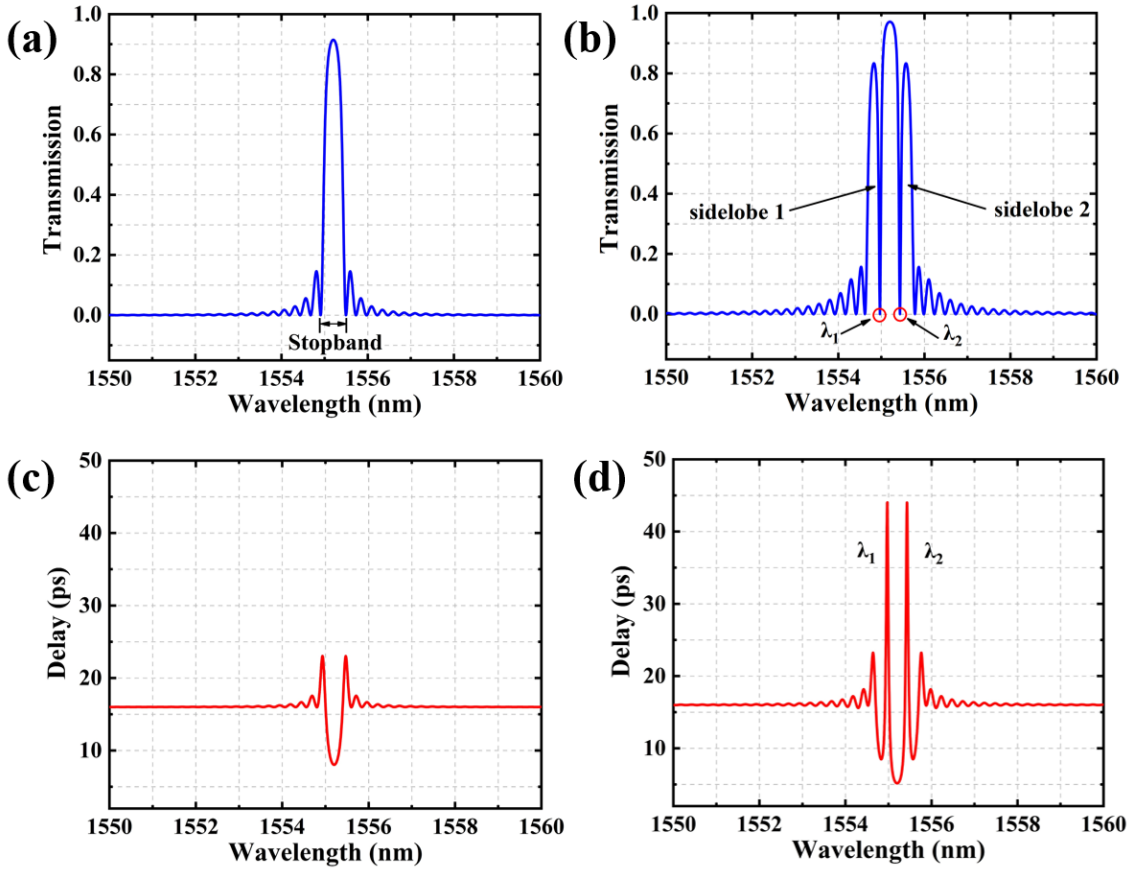

Fig. 2.14. The simulated reflection spectra of (a) uniform sidewall grating, and (b) sidewall grating with misalignment modulation. The time delay spectra of (c) uniform Bragg grating, (d) sidewall grating with misalignment modulation

When $\kappa(z)$ has an inverse-Gaussian distribution along the cavity as shown in (3), the two sidelobes of the stopband are significantly enhanced and form two transmission peaks which allow dual-wavelength lasing [85, 86]. The calculated reflection spectra and the time delay spectra based on the TMM are shown in Fig. 2.14. In the calculations, the effective index n_{eff} is set to 3.2, the grating period Λ_0 is set to 243 nm, κ_0 is 40/cm, and the cavity length L is 1000 μm. As shown in Fig. 2.14(a), a uniform grating provides a dominant reflection (stopband) with weak sidelobes on both sides. The peaks in the spectrum between the sidelobes and the stopband are too shallow to support dual-wavelength lasing. With modulation, the sidelobes are significantly enhanced, resulting in two deep and narrow peaks as shown in Fig. 2.14(b). The time-delay spectrum shown in Fig. 2.14(c) and (d) also illustrate that the time-delay peaks of λ_1 and λ_2 are significantly enhanced with the modulation scheme. Since the positions of the lasing wavelengths (λ_1 and λ_2) are the positions of the first zeros on either side of the maximum reflectivity, the wavelength spacing is equal to the width of the stopband which is related to L and κ_0 [65].

Using the TMM, the wavelength spacing for different L and κ_0 are calculated. As shown in Fig. 2.15, the frequency spacing increases with increasing κ_0, and decreases with increasing L. This result is consistent with the change law of the stopband width with κ_0 and L [65], and also indicates that the frequency spacing can be designed through appropriate choices of κ_0 and L.

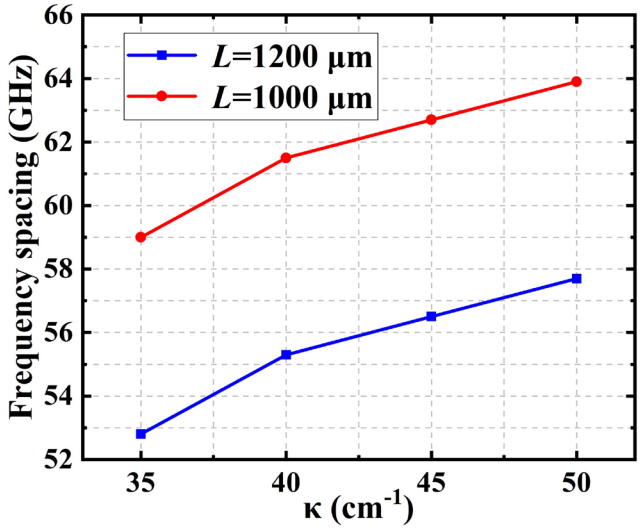

Fig. 2.15. Frequency spacing between the two lasing modes versus κ_0 under cavity lengths of 1000 μm and 1200 μm.

Figure 2.16 shows the photon distribution under the grating coupling coefficient modulation stucture. It can be observed that the photon distributions for the two wavelengths overlap within the cavity, which may lead to competition between the two modes. Unlike

phase-shifted gratings, the photon distribution within the cavity is smooth rather than concentrated at the phase shift locations, which helps to mitigate the longitudinal spatial hole burning effect of the laser.

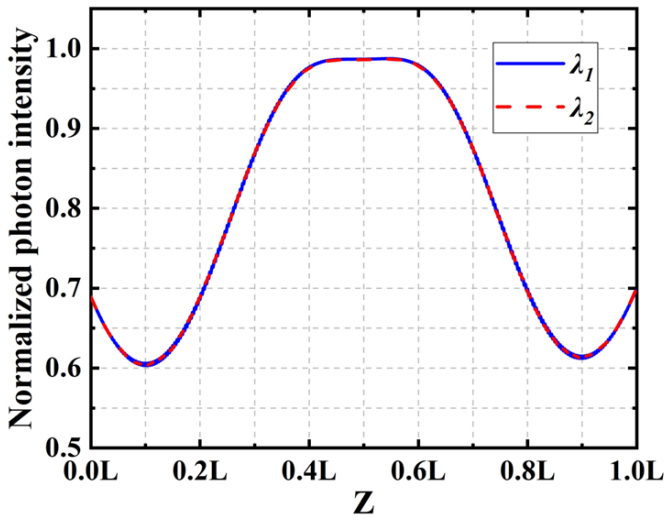

Fig. 2.16. Photon distribution of λ_1 and λ_2 with grating coupling coefficient modulation structure.

In conclusion, the proposed design is based on a laterally coupled modulated grating structure, where the grating coupling coefficient is controlled by adjusting the degree of alignment on both sides of the sidewall grating within each period. This modulation along the length of the cavity results in a coupling coefficient that follows an inverse-Gaussian distribution. As a result, the sidelobes on either side of the main reflection stopband are amplified, which, together with the stopband, forms two distinct transmission peaks. This configuration enables dual-wavelength lasing. The smooth photon distribution within the cavity, as opposed to the concentrated distribution in phase-shifted gratings, further reduces the longitudinal spatial hole burning effect, however, a potential drawback of this design is that the photon distributions for the two wavelengths are overlapping within the cavity, which can lead to mode competition.

Since the main stopband is directly proportional to the coupling coefficient κ_0 and inversely proportional to the cavity length L. By leveraging this relationship, it is possible to design devices with different κ_0 and L values to achieve difference wavelength separations, enabling the generation of different frequencies.

2.3.3 Superimposed sampled Bragg grating based on sidewall grating

It should be noted that the structures discussed in the previous two sections achieve dual-wavelength lasing by utilising either within a single reflection stopband or the regions on both sides of the stopband. Considering that the stopband width of DFB lasers is typically around 2 nm, means the wavelength interval $\lambda_2 - \lambda_1$ is less than 2 nm. According to the conversion for the frequency interval $\Delta f = \frac{c}{\lambda_1} - \frac{c}{\lambda_2}$ (c is the speed of light), the beat frequency will be less than 250 GHz, it is therefore not sufficient to achieve THz (above 300 GHz) using a single stopband. This section introduces a method of grating superimposition, where gratings with different periods are designed on both sides (upper side and lower side) of the sidewall grating to address this issue.

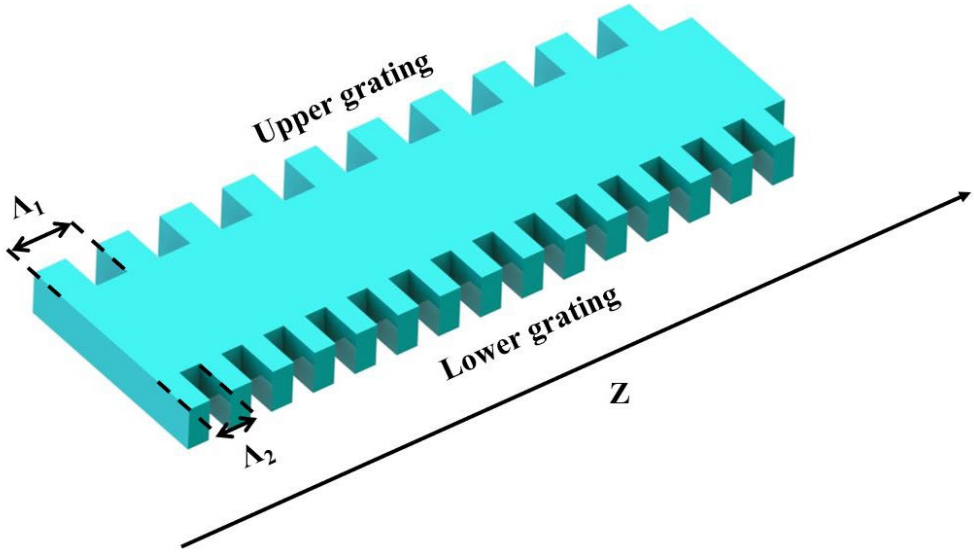

Fig. 2.17. Schematic of superimposed Bragg grating.

As shown in Figure 2.17, two different grating periods are set on either side of the sidewall grating, and the refractive index modulation is given by,

$$n(z) = \begin{cases} \frac{1}{2}\Delta n exp[i\left(\frac{2\pi z}{\Lambda_1} + \varphi_1\right)] + c.c \ (upper\ grating) \\ \frac{1}{2}\Delta n exp[i\left(\frac{2\pi z}{\Lambda_2} + \varphi_2\right)] + c.c \ \ (lower\ grating) \end{cases} \tag{2.29}$$

Considering that the TMM algorithm in previous content only calculates one-dimensional refractive index modulation, Equation 2.29 needs to be rewritten. Assuming that,

$$\begin{cases} \frac{1}{\Lambda_1} = \frac{1}{\Lambda_s} + \frac{1}{\Lambda_c} \\ \frac{1}{\Lambda_2} = \frac{1}{\Lambda_s} - \frac{1}{\Lambda_c} \end{cases} \tag{2.30}$$

Then Equation 2.29 can be expressed as,

$$n(z) = \begin{cases} \frac{1}{2}\Delta n exp[i\left(\frac{2\pi z}{\Lambda_s} + \frac{\varphi_1+\varphi_2}{2}\right)] \cdot \exp\left[i\left(\frac{2\pi z}{\Lambda_c} + \frac{\varphi_2-\varphi_1}{2}\right)\right] + c.c\ (upper\ grating) \\ \frac{1}{2}\Delta n exp\left[i\left(\frac{2\pi z}{\Lambda_s} + \frac{\varphi_1+\varphi_2}{2}\right)\right] \cdot \exp\left[-i\left(\frac{2\pi z}{\Lambda_c} + \frac{\varphi_2-\varphi_1}{2}\right)\right] + c.c\ (lower\ grating) \end{cases} \tag{2.31}$$

First, note that there is a common phase factor in both parts of the equation, $exp[i\left(\frac{2\pi z}{\Lambda_s} + \frac{\varphi_1+\varphi_2}{2}\right)]$, which represents the component where the two gratings are fully coupled. For the other pair of phase factors $\exp\left[i\left(\frac{2\pi z}{\Lambda_c} + \frac{\varphi_2-\varphi_1}{2}\right)\right]$ and $\exp\left[-i\left(\frac{2\pi z}{\Lambda_c} + \frac{\varphi_2-\varphi_1}{2}\right)\right]$, since they are complex conjugates with equal magnitudes, they can be understood as a modulation function applied to the amplitude of the refractive index. Taking only the real part, we have,

$$\Delta n(z) = \Delta n_0 \cos\left(\frac{2\pi z}{\Lambda_c} + \frac{\varphi_2-\varphi_1}{2}\right) \tag{2.32}$$

Where Δn_0 is the intrinsic amplitude of the refractive index modulation of the grating. Thus, Equation 2.29 can be expressed as,

$$n(z) = \frac{1}{2}\Delta n_0 \cos\left(\frac{2\pi z}{\Lambda_c} + \frac{\varphi_2-\varphi_1}{2}\right) \cdot exp\left[i\left(\frac{2\pi z}{\Lambda_s} + \frac{\varphi_1+\varphi_2}{2}\right)\right] + c.c \tag{2.33}$$

Where $\Lambda_s = 2\Lambda_1\Lambda_2/(\Lambda_1 + \Lambda_2)$ and $\Lambda_c = 2\Lambda_1\Lambda_2/|\Lambda_1 - \Lambda_2|$. In this way, the superimposition of the two Bragg gratings can actually be seen as a combination of a rapidly varying grating period Λ_s and a slowly varying envelope Λ_c of refractive index amplitude modulation [87-90]. It should be noted that the derivation of Equation 2.33 is intended to facilitate one-dimensional TMM simulations. In practice, for this grating superimposition model, when the Bragg wavelengths of the two gratings are sufficiently far apart (i.e., the stopbands of the two reflection spectra do not overlap), the grating superimposition can be simply understood as the sum of the two grating reflection spectra [65, 90-93], which still satisfies,

$$\begin{cases} \lambda_1 = 2n_{eff}\,\Lambda_1 \\ \lambda_2 = 2n_{eff}\,\Lambda_2 \end{cases} \tag{2.34}$$

If the period difference between the two side gratings is too small, leading to partial overlap of the two reflection spectra, new interference will occur in the overlapping region, generating additional modes. It should be noted that the method of using overlapping reflection stopbands to construct the target reflection spectrum is also known as a Moiré grating [94-97]. Similarly, if the π phase shifts are introduced in the middle of the two side gratings respectively, it can ensure that both gratings support single longitudinal mode lasing.

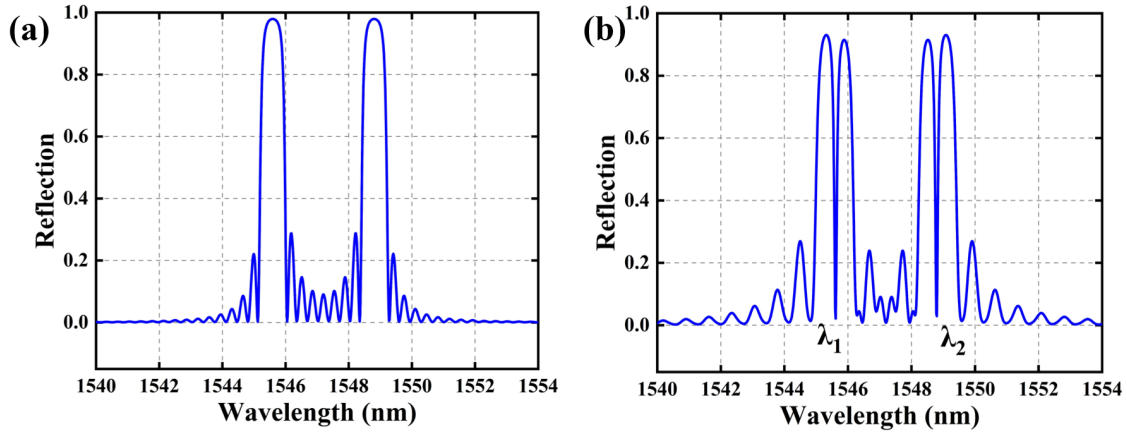

Fig. 2.18. Calculated reflection spectra of (a) uniform superimposed grating, (b) with π phase shifts at the middle of both sides.

As shown in Figure 2.18, the reflection spectra of the superimposed uniform grating and the grating with π-phase shifts were calculated. It can be clearly seen that each reflection channel contains a resonance peak, resulting in dual-wavelength lasing, where λ_1=1545.6 nm and λ_2=1548.8 nm. The simulation parameters are shown in Table 2.3.

Table 2.3 Simulation parameters of the superimposed uniform grating

Parameter	value
Cavity length L	1000 μm
Refractive index n_{eff}	3.2
upper grating period Λ_1	241.5 nm
lower grating period Λ_2	242 nm
Index modulation amplitude Δn	0.0039
π phase shifts positions	1/2 L

Obviously, according to Equation 2.34, the wavelength difference between the two modes is $\Delta\lambda = \lambda_2 - \lambda_2 = 2n_{eff}(\Lambda_2 - \Lambda_1)$. Assuming an effective refractive index of 3.2 and a maximum grating pattern resolution of 0.5 nm, the $\Delta\lambda$ must be an integer multiple of 3.2 nm, corresponds to a frequency spacing of 400 GHz. Clearly, this is insufficient to effectively cover the terahertz gap [98]. To address this issue, the uniform gratings on both sides need to be replaced with sampled Bragg gratings (SBG).

For a sampled Bragg grating, the refractive index expression is,

$$n(z) = \frac{1}{2}\Delta n \cdot s(z) \cdot exp[i\left(\frac{2\pi z}{\Lambda_1}\right)] + c.c \tag{2.35}$$

Where the sampling function $s(z)$ is a square wave function with a 50% duty cycle and P represents the sampling period. Then after Fourier series expansion, $\Delta n(z)$ can be expressed as,

$$n(z) = \sum_m \frac{1}{2} \Delta n F_m \exp\left[i\frac{2\pi z}{\Lambda_0} + i\frac{2\pi m z}{P}\right] + c.c \tag{2.36}$$

Where F_m represents the Fourier series coefficients of the square wave sampling function,

$$F_m = \frac{1}{P}\int_0^P s(z)\exp\left(\frac{i2\pi m z}{P}\right) \tag{2.37}$$

For the +1st channel, i.e., when $m = 1$, $F_m = \frac{1}{\pi}$, and Equation 2.36 can be,

$$n(z) = \frac{1}{2\pi} \Delta n \exp\left[i\frac{(P+\Lambda_0)2\pi z}{P\Lambda_0} +\right] + c.c \tag{2.38}$$

Here, it can be seen that the position of the +1st channel satisfies Equation 2.23 mentioned earlier, and the rate of change of the +1st channel wavelength with respect to the sampling period also conforms to Equation 2.25, which is much smaller than that of a uniform Bragg grating. For example, with a seed grating period of 257 nm, when the sampling period (around 4.5 μm) changes by 0.5 nm, the +1st channel wavelength changes by 0.00935 nm, equivalent to 1.17 GHz. This greatly enhances the design resolution of the beat frequency in this structure. In fact, due to this "scaling" characteristic of wavelength design, sampled grating structures have also been used in recent years for high-precision single-wavelength arrays and dense wavelength division multiplexing (DWDM) systems [99-105].

In addition, for Equation 2.36, if a displacement ΔP is introduced at $z = z_0$,

$$n(z) = \begin{cases} \frac{1}{2\pi} \Delta n \exp\left[i\frac{2\pi z}{\Lambda_0} + i\frac{2\pi z}{P}\right] + c.c \ (z < z_0) \\ \frac{1}{2\pi} \Delta n \exp\left[i\frac{2\pi z}{\Lambda_0} + i\frac{2\pi z}{P} + i\frac{2\pi \Delta P}{P}\right] \ (z \geq z_0) \end{cases} \tag{2.39}$$

It is equivalent to introducing a phase shift $\theta = \frac{2\pi\Delta P}{P}$, Thus, when $\Delta P = 0.5P$, $\theta = \pi$, meaning a displacement of $0.5P$ is equivalent to a π phase shift and is called an equivalent π phase shift (π-EPS).

Fig. 2.19 shows the structure of the superimposed SBG. The seed gratings on both sides are identical, with the same period Λ_0. Different sampling periods, P_1 and P_2 are applied on each side, and two independent π-EPSs are located in the middle of each side grating, ensuring each side forms its own single-wavelength lasing.

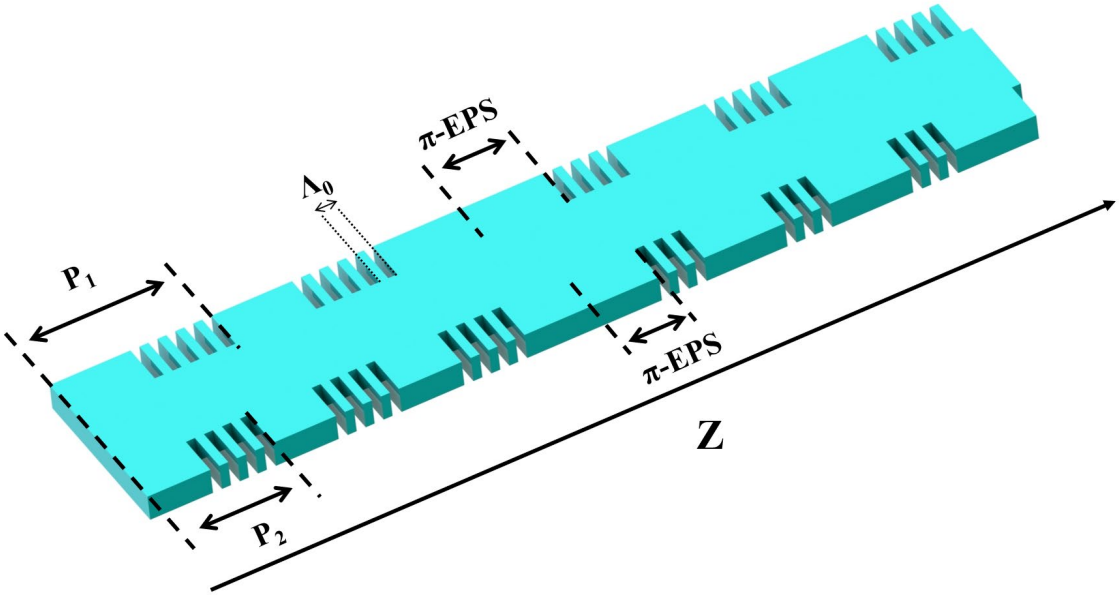

Fig. 2.19. Schematic of superimposed SBG.

Using the TMM algorithm, the reflection spectra array of the superimposed SBG were calculated and is shown in Fig 2.20. The simulation parameters are provided in Table 2.4. For this structure, the seed grating was initially set at 257 nm, ensuring that the 0th channel is far from the gain region around 1550 nm. The sampling periods were then set around 4.5 μm according to the specific wavelengths.

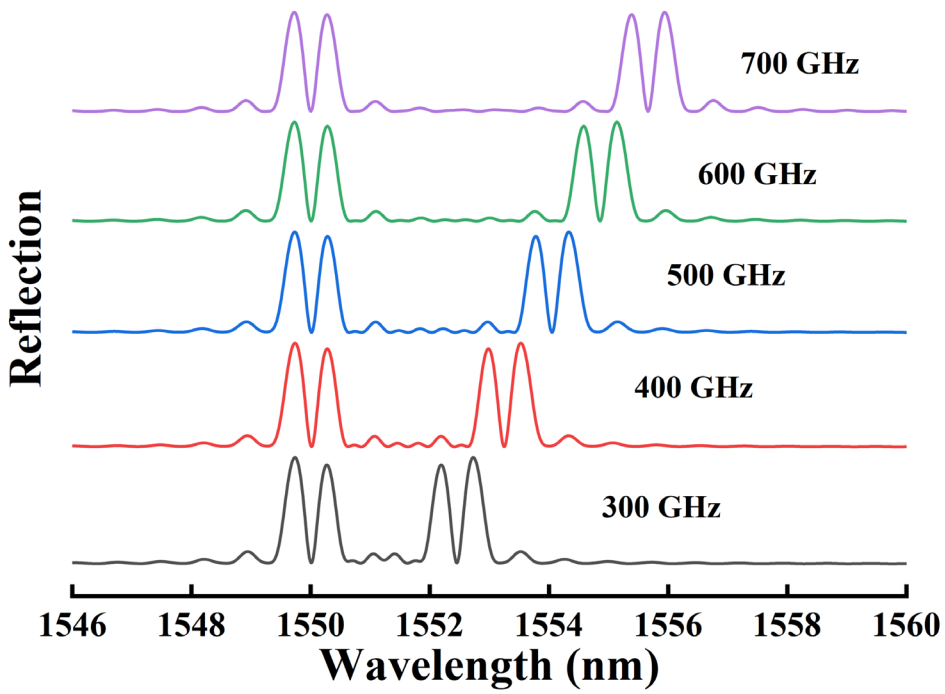

Fig. 2.20. Calculated reflection spectra of superimposed SBG with different P_1 and P_2.

Table 2.4 Simulation parameters of superimposed SBG

Beat frequency	n_{eff}	Λ_0	Δn	λ_1	λ_2	P_1	P_2
300 GHz					1552.4 nm		4.324 μm
400 GHz					1553.2 nm		4.364 μm
500 GHz	3.2	257 nm	0.0039	1550 nm	1554.0 nm	4.207 μm	4.405 μm
600 GHz					1554.8 nm		4.447 μm
700 GHz					1555.6 nm		4.490 μm

Table 2.5 Equivalent parameters of superimposed uniform Bragg grating

Beat frequency	n_{eff}	λ_1	λ_2	Λ_1	Λ_2
300 GHz			1552.4 nm		242.5725 nm
400 GHz			1553.2 nm		242.6975 nm
500 GHz	3.2	1550 nm	1554.0 nm	242.1875nm	242.8225 nm
600 GHz			1554.8 nm		242.9475 nm
700 GHz			1555.6 nm		243.0725 nm

Table 2.5 shows the parameters required to achieve Fig 2.20 using superimposed uniform Bragg gratings. In the case of the superimposed SBG, to increase the spacing by 100 GHz, the sampling period needs to change by approximately 41 nm, which is easily manageable with a 0.5 nm resolution in EBL. In contrast, for uniform Bragg gratings, to increase the frequency by 100 GHz, the seed grating period would need to change by 0.125 nm, which far exceeds the maximum resolution of EBL. Obviously, the superimposed SBG provides a practical solution for covering the terahertz gap.

It should be noticed that, since both SBG and 4PS satisfy Equations 2.23 and 2.25, a superimposed 4PS can also effectively cover the terahertz gap. However, because the 4PS structure has a larger equivalent κ in the $+1^{st}$ channel, its reflection spectrum stopband is wider, making it more likely for the two reflection spectra to overlap. This overlap limits the minimum frequency spacing that can be designed with superimposed 4PS structure. Therefore, using superimposed SBG is more appropriate in this context.

In summary, the two π phase shifts with equivalent chirp structure and the lateral coupling coefficient modulation structure introduced in the previous two sections are both

designed to achieve dual-wavelength lasing based on a single reflection stopband. Consequently, the maximum frequency difference between the two wavelengths is limited by the width of the reflection stopband, making these structures more suitable for dual-wavelength lasers operating in the MMW range. The superimposed SBG, on the other hand, leverages two independently designed reflection spectra, allowing for frequency spacing that can easily cover the terahertz range. However, due to the potential for interference when the two stopbands overlap, the superimposed SBG is less effective for achieving the smaller frequency differences required in the MMW range. Therefore, in practical device production, the appropriate structure should be selected based on the specific frequency requirements.

2.4 Dynamic characteristic simulation based on time-domain traveling wave model

Section 2.2 introduced the TMM algorithm, which is primarily used to calculate the passive response of gratings. In reality, the transmission of optical signals within a DFB laser involves a nonlinear system. This is particularly important when two wavelengths of light interfere within the resonant cavity, leading to changes in the distribution of carriers and photons, which in turn affects the refractive index and gain. Therefore, it is necessary to take these factors into account to study the dynamic output characteristics of dual-wavelength lasers and the conditions required for stable output. In this section, by solving the time-domain coupled-wave equations, the effects of gain saturation and LSHB in the laser are taken into account, this model has been validated and applied in the study of large-signal modulation dynamic characteristics of DFB lasers [106, 107]. The transient response and spectral characteristics of the laser are calculated, and the spectral information is obtained by analysing the time-domain optical field signals through Fourier transformation.

In traveling wave model (TWM), the optical field inside the laser can be represented by the forward propagating wave $A(z,t)$ and the backward-propagating wave $B(z,t)$. The total electric field is expressed as,

$$E(z,t) = A(z,t)e^{-i\beta_0 z} + B(z,t)e^{i\beta_0 z} \tag{2.40}$$

Where β_0 is the propagation constant at the Bragg frequency. The evolution of the forward and backward waves is described by the time-domain coupled-wave equations, which include gain, loss, and coupling effects,

$$\begin{cases} \frac{\partial A(z,t)}{\partial t} + v_g \frac{\partial A(z,t)}{\partial t} = (g - \alpha - i\Delta\beta)A(z,t) + i\kappa B(z,t) + s_A(z,t) \\ \frac{\partial B(z,t)}{\partial t} + v_g \frac{\partial B(z,t)}{\partial t} = (g - \alpha - i\Delta\beta)B(z,t) + i\kappa A(z,t) + s_B(z,t) \end{cases} \tag{2.41}$$

Where g is the field gain, determined by the carrier density, α is the loss coefficient caused by material absorption and waveguide scattering. $\Delta\beta$ is the Bragg detuning, κ is the coupling coefficient and $s_A(z,t)$, $s_B(z,t)$ are the spontaneous emission noise, typically generated as random noise. v_g refers to the group velocity. The field gain g is given by,

$$g(z,t) = \frac{\Gamma g_N[N(z,t)-N_0]}{2(1+\varepsilon P)} \tag{2.42}$$

where Γ is the optical confinement coefficient of the active layer, g_N is the differential gain, N_0 is the carrier density at transparency, ε is the gain compression coefficient, $N(z,t)$ is the carrier density with time and location, P the photon density. Due to the carrier injection effect [108], the effective refractive index can be expressed as,

$$n_{eff}(z,t) = n_{eff0} - \Gamma\alpha_H g_N[N(z,t) - N_0] \tag{2.43}$$

The refractive index takes the value n_{eff0} at the carrier density $N = N_0$, and α_H is the material linewidth enhancement factor [109].

The coupled Equation (2.41) can be solved in the time domain by a first-order difference approximation to the partial differential. If we choose the relation between time and spatial steps as $\Delta z = v_g \cdot \Delta t$ and neglect the second derivative $\frac{\partial^2 A(z,t)}{\partial z \partial t}$and $\frac{\partial^2 B(z,t)}{\partial z \partial t}$, we can obtain the traveling wave formula as follows,

$$\begin{cases} A(z+\Delta z, t+\Delta t) - A(z,t) = \\ \Delta z \cdot [(g - \alpha - i\Delta\beta)A(z,t) + i\kappa B(z,t) + s_A(z,t)] \\ B(z+\Delta z, t+\Delta t) - B(z,t) = \\ \Delta z \cdot [(g - \alpha - i\Delta\beta)B(z,t) + i\kappa A(z,t) + s_B(z,t)] \end{cases} \tag{2.44}$$

It is noted that with changes in carrier concentration, v_g will also fluctuate, but it is considered a constant here, as this assumption does not significantly impact the simulation results. Additionally, unlike the TMM algorithm, TWM does not input a wavelength to calculate the response. Instead, it solves the time-domain finite difference equations based on the pre-set Bragg propagation constant β (which already includes Bragg wavelength information) and a certain frequency detuning range $\Delta\beta$ to obtain the relationship between the laser output and time.

The time-dependent carrier rate equation is described as,

$$\frac{dN}{dt} = \frac{J}{ed} - B_m N^2 - C_m N^3 - \frac{g_N[N-N_0]}{1+\varepsilon P} v_g P \tag{2.45}$$

where J is the current injection density, e is the electron charge, d is the thickness of the active layer,B_m and C_m are bimolecular and Auger recombination coefficients, respectively. and P is the photon density, which is given by the normalized power $[|A|^2 + |B|^2]$.

If we choose $z = 0$ as the left facet, the boundary condition for the forward and reverse waves at the facets can be written as,

$$\begin{cases} A(0,t) = r_L B(0,t) \\ B(0,t) = r_R A(0,t) \end{cases} \tag{2.46}$$

where r_L and r_R are the amplitudes of the reflections from the left and right facets, respectively.

To take the spatial hole burning into consideration, the laser is divided into a number of sections with length $\Delta z = L/M$, where L is the cavity length and M is the number of sections, here $M = 200$. Theoretically, the material and grating parameters (g_N, n_{eff0}, α, β, κ) within each small grid can be customized to construct models under different conditions. In each time step, the carrier density N, field gain g, and effective index n_{eff} will change according to Equations (2.42), (2.43) and (2.45). The spontaneous noise is generated from a Gaussian distributed random number generator that satisfies the correlation [110],

$$\begin{cases} < S(z,t) \cdot S^*(z',t) >= \gamma K R_{SP} \Delta\beta(t-t') \cdot \Delta\beta(z-z')/v_g \\ < S(z,t) \cdot S(z',t) >= 0 \end{cases} \tag{2.47}$$

here $R_{SP} = B_m N^2/L$ is the bimolecular recombination per unit length contributed to spontaneous emission, γ is the spontaneous coupling factor, and K is the transverse Petermann factor. It has been proved by Petermann that the spontaneous emission fields coupled to the forward and reverse waves have equal amplitudes [111]. Table 2.6 shows the material and waveguide parameters used in the TWM.

It should be noted that since the fabrication process described later does not include the step of facet coating, the reflectivity of both facets is set to 0.32 during the simulation [112], and $\kappa L = 1.0$. A π-phase-shifted single-wavelength laser was simulated using the data from Table 2.6 and the injected current is 1.8 times the transparency current, as shown in Fig 2.21. It can be observed that after the laser surpasses the threshold and undergoes relaxation oscillations, the output power stabilises. The small fluctuations shown in the inset originate from spontaneous emission noise.

Table 2.6 Material and waveguide parameters used in the TWM

Parameter	Value
Bimolecular carrier recombination coefficient B_m	$1 \cdot 10^{10}\ cm^3 \cdot s^{-1}$
Auger carrier recombination coefficient C_m	$1 \cdot 10^{29}\ cm^6 \cdot s^{-1}$
Differential gain g_N	$3 \cdot 10^{16}\ cm^2$
Transparency carrier density N_0	$1.8 \cdot 10^{18}\ cm^{-3}$
Linewidth enhancement factor α_H	3
Absorption and scattering loss in wave guide α	$30\ cm^{-1}$
Effective refractive index n_{eff0}	3.2
Effective group refractive index n_g	3.5
Waveguide confinement factor Γ	0.35
Length of the laser cavity L	1000 μm
Thickness of the active layer d	78 nm
Spontaneous coupling factor γ	10^{-4}
Petermann factor K	1
Bragg wavelength λ_b	1550 nm
Nonlinear gain suppression coefficient ε	$3 \cdot 10^{-17}\ cm^3$

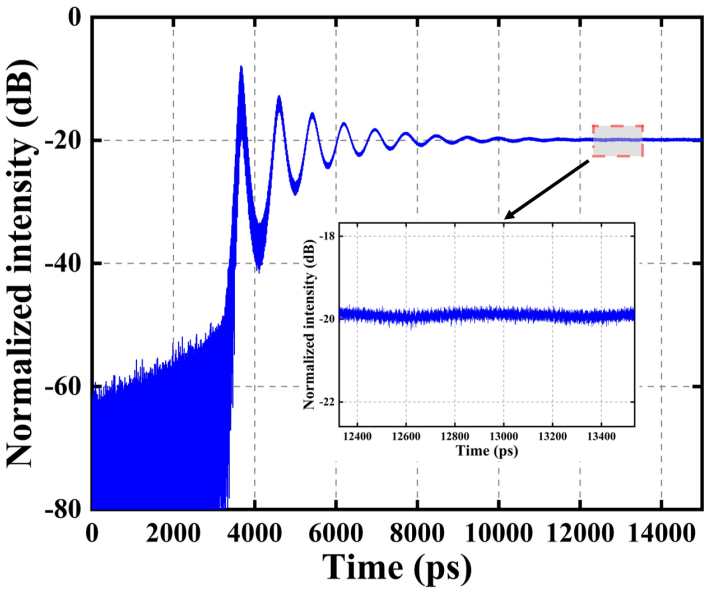

Fig. 2.21. Calculated output of a single wavelength DFB laser, with the inset showing an enlarged view of the data within the small red window under stable conditions.

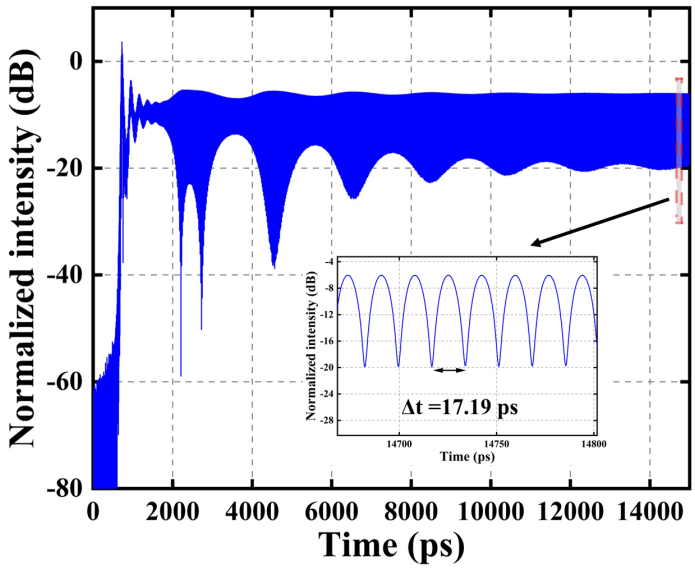

Fig. 2.22. Calculated output of a dual-wavelength DFB laser, the inset shows the enlarged beat output in the small red window.

Fig 2.22 shows the simulation results of the two π phase shifts with chirped grating structure, where the chirp is achieved by modifying the Bragg constant of each section, with a chirp rate set to 25 nm/mm. Since the coexistence of two lasing modes within the cavity requires larger carrier consumption, a higher injection current is needed to operate the device in a dual-wavelength state, the operation of Fig 2.22 is under three times of the transparency current. Due to the higher injection, the laser undergoes the process of turn-on and relaxation oscillations within 2000 ps. After 2000 ps, the laser exhibits a typical beat output state. It can be observed that between 2000 ps and 14000 ps, the beat output amplitude is modulated by a gradually decreasing intensity, which may be due to residual relaxation oscillations affecting the rate of carrier replenishment and consumption within the cavity. After 14,000 ps, the laser's beat output gradually stabilises, and the enlarged data reveals a beat period of 17.19 ps, corresponding to a frequency of 58.17 GHz.

As shown in Fig 2.23(a), by applying a fast Fourier transform to the laser output of Fig 2.22, the spectrum can be obtained, clearly revealing the two lasing wavelengths, which are $\lambda_1 = 1549.17\,nm$, $\lambda_2 = 1549.63\,nm$. The frequency difference between λ_1 and λ_2 is 58.17 GHz, consistent with the oscillation period of the laser output. It is worth noting that, since the TWM model accounts for the variations in carrier concentration and effective refractive index with the optical field, four-wave mixing (FWM) signals (FWM 1 and FWM 2) appear on both sides of the two lasing modes. Additionally, due to the introduction of facet reflections, Fabry-Pérot (FP) modes are observed in the spectrum, with a spacing of 42.86 GHz, matching the set cavity length of 1000 μm and group refractive index of 3.5.

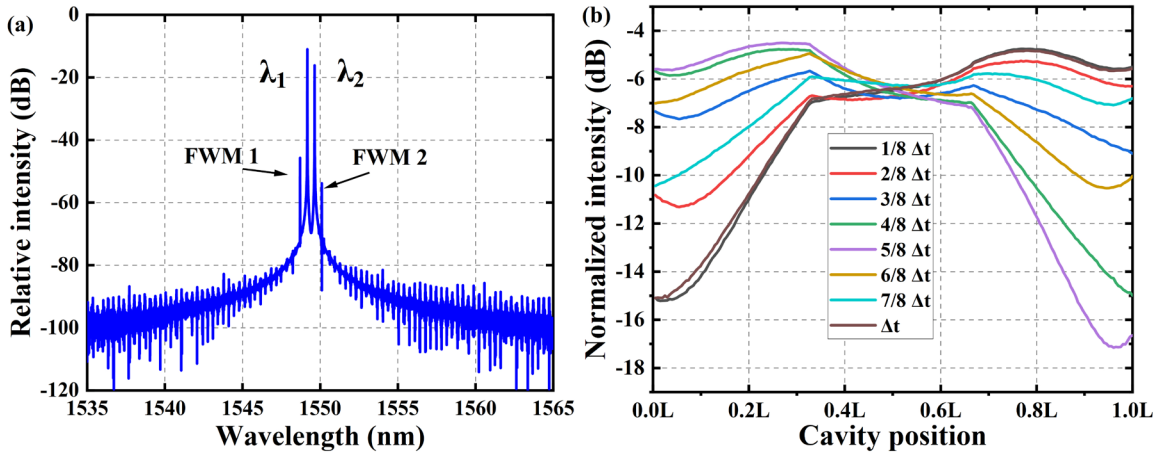

Fig. 2.23. (a) Calculated optical spectrum of a dual-wavelength DFB laser, (b) variation of the photon distribution over one oscillation period.

Clearly, since the laser is in an oscillatory output state, the internal photon distribution must be dynamically changing. Fig 2.23(b) shows the variation of the photon distribution over one oscillation period Δt. First, consistent with the static analysis results, photons locally accumulate at the two π phase shifts positions. Additionally, within one period, the overall photon distribution shifts either to the left or to the right, corresponding to the oscillation of the output power at one of the facets.

Due to the significant facet reflections, the dual-wavelength output of the laser is sensitive to the arbitrary phases at the facets [112-115]. During the simulation, the reflectivity at both ends was kept at 0.32, with the phase of the right facet fixed at 0. The spectra were calculated for the left facet phase varying between 0 and 2π, and the results are shown in Fig 2.24. The simulation results indicate that the device achieves the desired dual-wavelength output state only when the left facet phase is between 0.3π and 1.3π. Considering that the phase of the facets becomes uncontrollable during the cleaving process in laser fabrication, this means that even with optimal performance in other steps, the overall yield of the device would be limited to 50%. To address this issue, an additional EAM is incorporated at one of the facets during the device design. The EAM region is typically used to apply RF signals for modulation, however, in this work, the EAM is utilized to apply a constant reverse bias for phase modulation, thereby ensuring the device operates in a dual-wavelength output state. The detailed fabrication of this component will be discussed in Chapter 3.

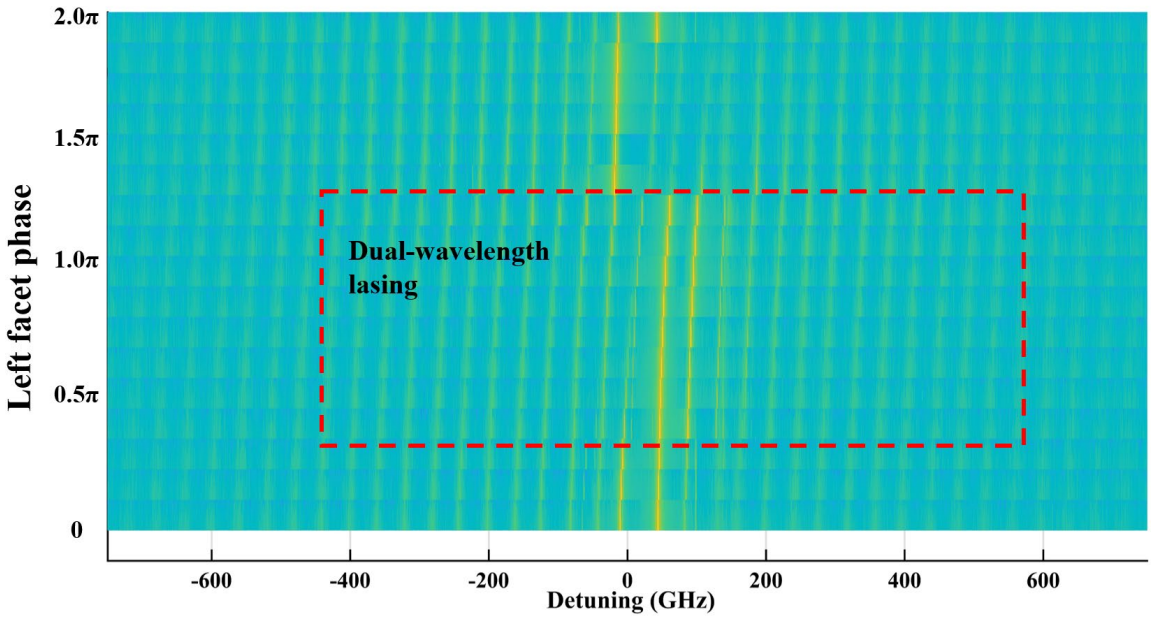

Fig. 2.24. Spectrum under different left facet phases.

2.5 Wafer structure and waveguide

In the previous sections, the focus was primarily on the selection of the laser's longitudinal modes, i.e., the wavelengths. In addition to this, the laser also requires an appropriate structure, specifically a waveguide, designed according to the epitaxial material stack, to confine the propagation direction of the optical signal.

Due to its advantages of low threshold current, good temperature stability, and high differential gain, the quantum well system forms the active region of the semiconductor laser [116-121]. Moreover, semiconductor materials have a convenient characteristic in that materials with lower bandgap have a higher refractive index, which allows the entire wafer to confine the propagating light near the quantum well layer through total internal reflection. However, a multi-quantum well (MQW) structure alone is inadequate for effectively confining both propagating light and electrons. The solution is to incorporate separate confinement heterostructure (SCH) layers, which guide the light and ensure that escaping electrons or holes remain near their respective quantum wells. Consequently, the equivalent slab waveguide consists of multiple layers as shown in Fig 2.25. Noticed that the index in

the SCH layers may be graded because the composition of the separate confinement layers may be graded.

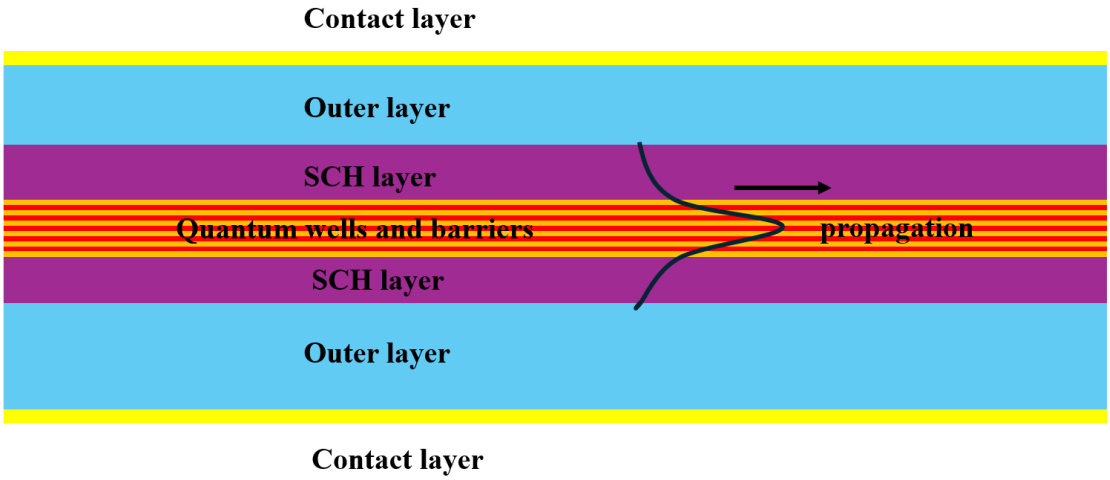

Fig. 2.25. Schematic of multi-layers slab wave guide.

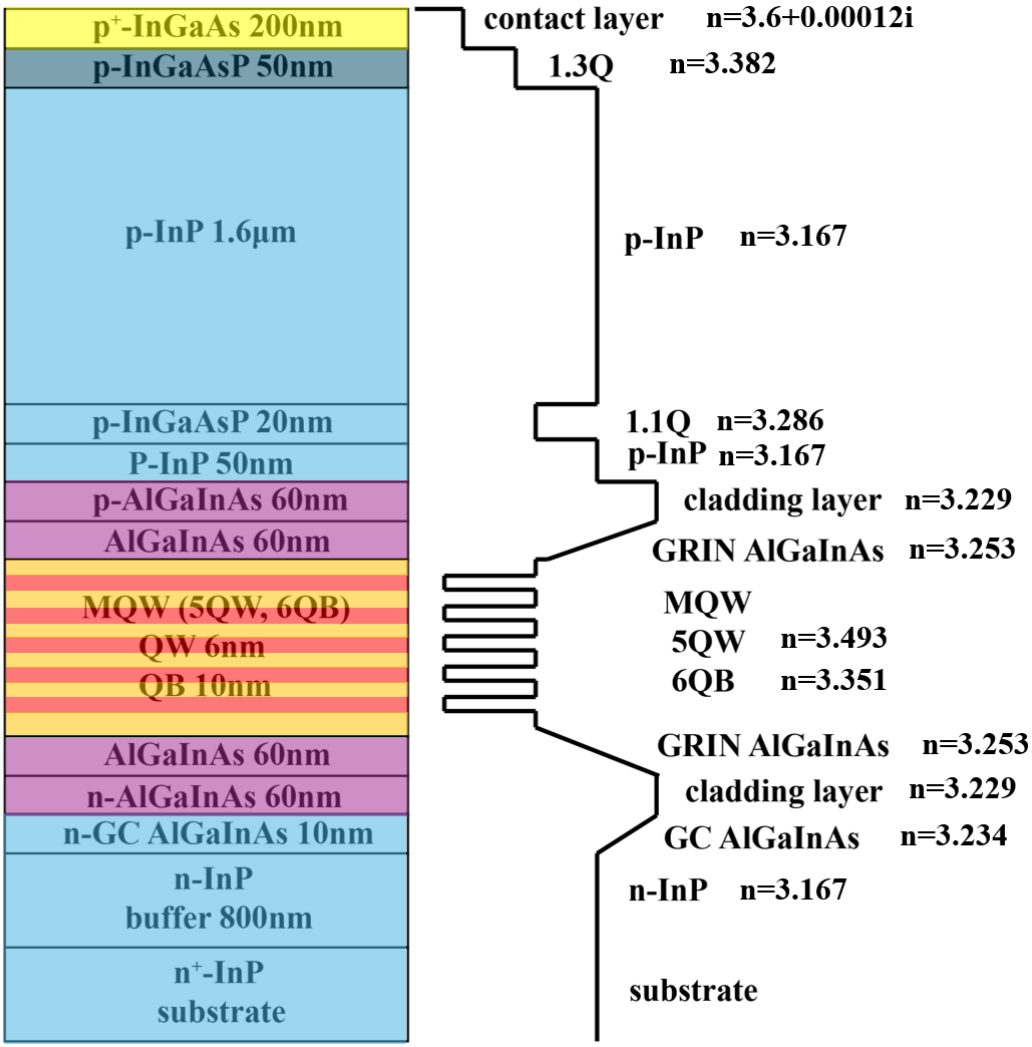

Fig. 2.26. Schematic of IQE 5 QWs InP wafer.

The epitaxial wafer used in this thesis is a 5-quantum well system based on InP, sourced from IQE (International Quantum Epitaxy) company, with an electroluminescence peak wavelength of approximately 1530 nm at room temperature. The quantum well system consists of five 6 nm-thick AlGaInAs wells and six 10 nm-thick AlGaInAs barriers, arranged in an alternating stack. Positioned above and below the quantum well system are two 60 nm AlGaInAs graded index separate confinement heterostructure (GRINSCH) layers, which collaborate with the quantum wells to confine light propagation and prevent electrons and holes from escaping the quantum well region. The P-type (Zn-doped, 1600 nm thick) and N-type (Si-doped, 800 nm thick) doped InP layers are positioned at the upper and lower layers of the MQWs system, respectively, to form the basic PN junction structure. A 20 nm layer of InGaAsP is placed between the P-type InP and the upper GRINSCH as an etch stop layer to prevent damage to the quantum well layer during the wet etching process. A heavily doped P-type InGaAs layer is grown on the topmost layer of the wafer, serving to connect with the subsequently deposited metal electrodes and to pump the device. Fig 2.26 illustrates the detailed epitaxial structure, showing the refractive index profile and the corresponding conduction band diagram for each layer.

Using Lumerical software, the spontaneous emission gain of the quantum well structure was calculated under different carrier injection concentrations and temperatures [122]. The results are shown in Fig 2.27. The results indicate that the gain peak of this structure is around 1550 nm, and with the increase in carrier concentration, the gain peak experiences a blue shift due to the carrier injection effect. Furthermore, when the carrier concentration remains constant, an increase in temperature leads to a reduction in the bandgap between the conduction band and the valence band, resulting in a red shift of the gain. Additionally, as the temperature rises, the intensity of the spontaneous emission gain decreases due to the increased rate of non-radiative recombination processes such as Auger recombination [123-125].

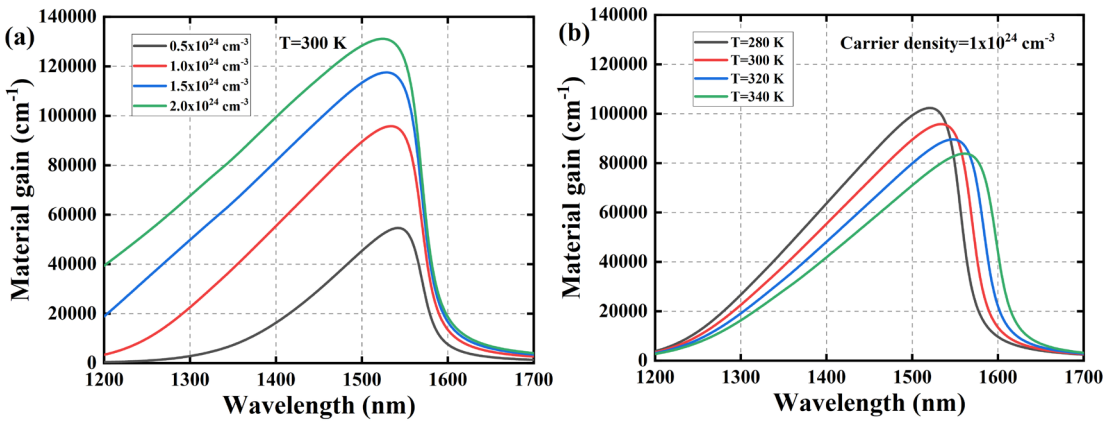

Fig. 2.27. (a) Material gain versus carrier density, and (b) temperature.

The confinement of the transverse optical field is achieved by a ridge waveguide. In this study, the height of the ridge waveguide is set to 1.92 μm, which corresponds to etching down to the upper 60 nm AlGaInAs cladding layer on both sides of the waveguide. Although theoretically, increasing the etching depth beyond the quantum well can provide a higher grating coupling coefficient, it also leads to larger waveguide loss, which is detrimental to the feedback and lasing of the device. Since a sidewall grating structure is used, etching into the quantum well would alter the cross-sectional profile of the gain region, changing the structure from refractive index coupling to gain coupling, making the previous simulation results inapplicable. Moreover, a deeper etching depth presents higher fabrication challenges. Due to the small dimensions, the etching rate in the grating gaps is slower than on other surfaces, making it difficult to maintain the etched pattern in alignment with the design.

Therefore, the decision to etch down to the 60 nm upper AlGaInAs cladding layer is made to achieve two objectives: on one hand, it allows for proximity to the quantum well to obtain a higher grating coupling coefficient, and on the other hand, it provides a margin for etching depth, preventing excessive etching beyond the quantum well layer due to potential errors.

Based on the etching depth of 1.92 μm, the transverse modes for different waveguide widths were simulated using Lumerical Mode Solutions. The results are presented in Fig 2.28. For the TE_0 mode, the cutoff waveguide width is 0.6 μm, while for the TE_{01} mode, the cutoff width is 2.2 μm.

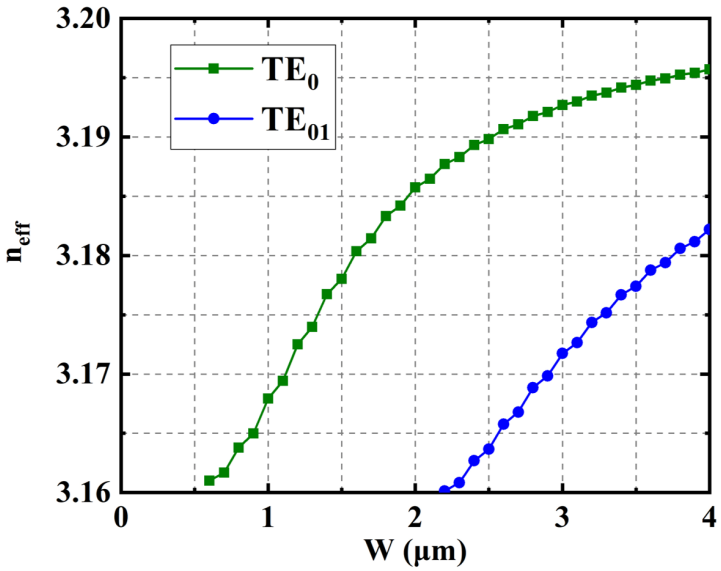

Fig. 2.28. Refractive index under different waveguide width W.

To achieve larger carrier injection and lower waveguide loss, the ridge waveguide width W is set to 2.5 μm, while the grating recess depth on each side needs to be set between 0.15

and 0.7 μm. As a result, in the cross-sectional area where the grating is etched, the waveguide width will range between 1.1 and 2.2 μm. Within this range, the TE_{01} mode will experience extremely high waveguide losses, making it unable to resonate effectively within the waveguide. Additionally, this width remains greater than the cutoff width of the TE0 mode, ensuring the transmission of this mode. Fig 2.29 shows the field intensity distribution for waveguide widths of 2.5 μm and 1.1 μm, respectively. The bottom part of the figure illustrates the projection of the field intensity and the waveguide profile.

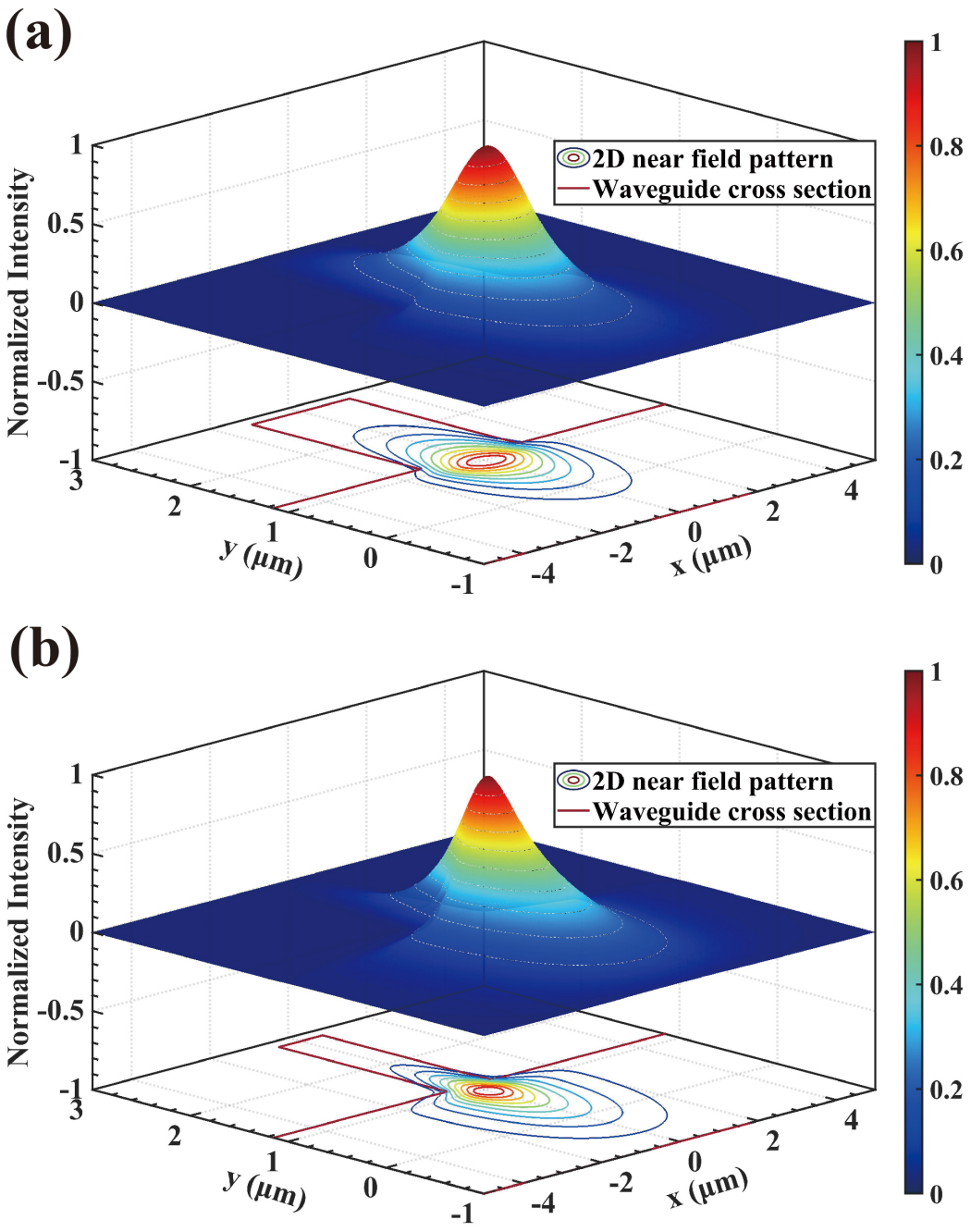

Fig. 2.29. Transverse mode diagram of (a) W=2.5 μm, (b) W=1.1 μm.

Table 2.7 grating coupling coefficient κ under different grating lateral recess depth

Ridge waveguide width (μm)	lateral recess depth (μm)	κ (cm^{-1})
2.5	0.1	30.70875
	0.2	67.99807
	0.3	113.7292
	0.4	170.01114
	0.5	238.92984
	0.6	321.31202
	0.7	413.60592

Based on Equation 2.6, the grating coupling coefficient κ was calculated for a ridge waveguide width of 2.5 μm, with the grating lateral recess depth varying from 0.1 to 0.7 μm. The results are shown in Table 2.7.

2.6 Chapter summary

In this chapter, it is first explained that the optical beat frequency between two different optical frequencies can generate a MMW or THz wave corresponding to their frequency difference. Subsequently, the passive TMM algorithm is introduced for designing gratings suitable for dual-wavelength generation. Then, the fundamental principles and filtering characteristics of three novel grating structures are detailed.

The two π phase shifts grating with equivalent chirp structure utilises two π phase shifts at symmetrical positions within the cavity, creating two transmission peaks within the reflection spectrum's stopband, corresponding to the two lasing wavelengths. The equivalent chirp, on one hand, separates the photon distribution of the two lasing wavelengths within the cavity, reducing mode competition, while also offering the ability to modulate the wavelength difference by adjusting the chirp rate. On the other hand, the chirp is equivalently realised by altering the micron-scale phase modulation period, significantly reducing fabrication complexity.

The second structure, sidewall grating with lateral modulation of the grating coupling coefficient, modulates the grating coupling distribution within the entire resonant cavity by controlling the degree of misalignment of the gratings on both sides within each period, shaping it into an inverse Gaussian curve. This modulation enhances the sidelobes on both sides of the stopband, providing sufficient reflection to create transmission gaps alongside

the central main stopband. In this structure, the spacing between the dual wavelengths is equal to the stopband width, allowing the dual-wavelength spacing to be adjusted by modulating the DFB cavity length and the grating coupling coefficient.

The third approach, Superimposed sampled Bragg grating**,** utilises the principle of superimposing gratings, integrating gratings with different output wavelengths on both sides of the ridge waveguide. By leveraging the characteristics of sampled Bragg gratings, the frequency precision is improved from 400 GHz to 1.17 GHz (assuming the highest pattern resolution is 0.5 nm), theoretically enabling coverage of the entire THz gap above 100 GHz.

Subsequently, the dynamic characteristics of the laser during dual-wavelength output were simulated using the carrier rate equations and the TWM algorithm. Unlike single-wavelength lasers, after experiencing population inversion and relaxation oscillations, the photons (or carriers) within the cavity maintain periodic oscillations. The output power at the laser's end facet undergoes amplitude modulation at the beat frequency. Additionally, the impact of end-facet reflection and the facet phase on the laser's output state was simulated. The simulation results suggest that, during the design, it is necessary to integrate a phase adjustment region at the one end facet to ensure the yield of the device.

Finally, the wafer structure used in this thesis is presented, along with the design parameters for the ridge waveguide width and grating lateral recess depth. Chapter 3 introduces the steps for device fabrication based on the simulation results.

Chapter 3: Device Fabrication Process

For the nanofabrication of semiconductor devices, the core process involves two critical pattern transfer steps. First, the designed pattern is transferred onto the mask (resist layer) through exposure and development. Then, depending on the requirements, the pattern is transferred from the mask onto the sample using etching or thin film deposition techniques.

This chapter introduces the process of fabricating testable laser bar strips from a 2-inch InP wafer.

3.1 Sample preparation and marker definition

The standard size of an InP-based wafer is typically 2 inches. If the entire wafer is processed at once, any errors or variations during the process could lead to significant waste of the wafer. Therefore, the wafer is first cleaved into multiple samples, each measuring 11x12 mm. Only one sample is processed at a time, reducing the risk of waste and allowing for more controlled and precise fabrication, Fig 3.1 shows the cleaved sample.

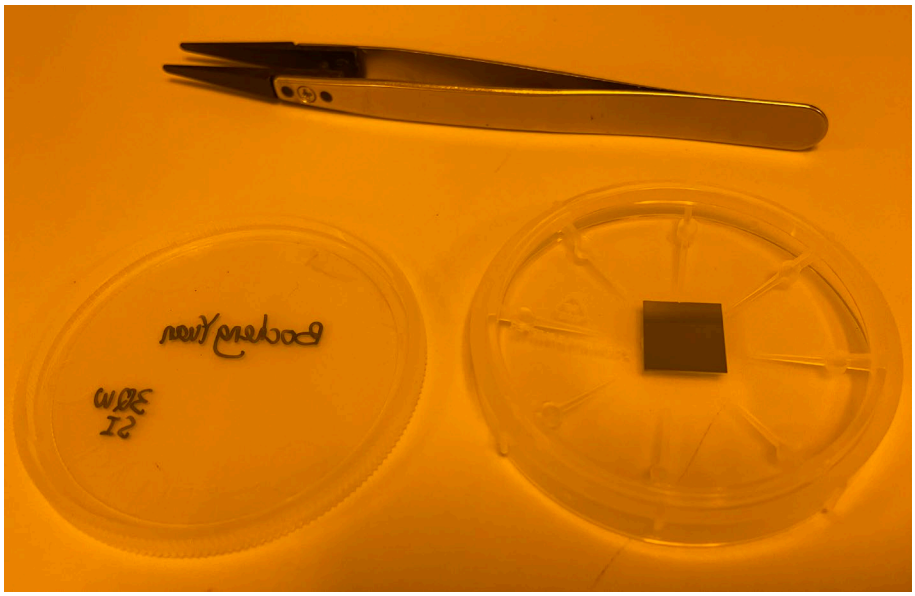

Fig. 3.1. Cleaved sample prepared for further processing.

Subsequently, the samples are cleaned using acetone, isopropanol (IPA), and deionized water (DI water), followed by drying the surface with nitrogen gas. The reason for this cleaning sequence is that acetone has excellent solubility, effectively dissolving most organic substances and evaporating quickly, leaving minimal residue on the sample surface. Acetone is used in the first cleaning step to remove most organic contaminants, preparing the sample for the following cleaning steps. IPA is miscible with acetone and can dissolve some polar

contaminants that acetone cannot remove. Additionally, IPA has a low surface tension, allowing it to penetrate small surface structures and evaporate easily, minimising residue on the surface. IPA also helps remove any trace residues left from the acetone cleaning process. Finally, DI water is highly purified, containing almost no ions or organic impurities, ensuring that it leaves no unwanted contaminants on the sample surface. DI water effectively removes any solvent residues from the previous cleaning steps, ensuring a clean surface. After the DI water rinse, samples are typically dried using nitrogen gas to prevent water spots from forming.

Since the sample processing workflow involves multiple electron beam (e-beam) exposures, each layer's mask pattern must be accurately aligned relative to the others. Therefore, it is necessary to first create alignment markers on the sample. These markers will be used to ensure proper alignment during each subsequent mask pattern writing process. Due to its high brightness and stable properties, Aurum (Au) is chosen as the material for the markers.

First, a layer of 15% 2010 PMMA (polymethyl methacrylate) is spin-coated onto the sample surface at a speed of 4000 rpm [126, 127]. Following this, the sample is baked on a hotplate at 180°C for 5 minutes. PMMA acts as a positive resist in lithography processes. This means that the exposed areas of PMMA become more soluble in the developer solution after e-beam exposure, allowing those regions to be washed away during the development process. The baking helps accelerate the evaporation of the resist solvents, making the resist layer more stable and uniform, which enhances the accuracy of subsequent exposure and development processes. At this spin speed, a 15% PMMA solution results in a film thickness of approximately 1.2 μm. Next, a layer of 4% 2010 PMMA is spin-coated onto the sample, following the same procedure as before, forming a 110 nm mask layer. The spin-coated sample is then exposed to an e-beam according to the pre-designed pattern, followed by development to reveal the pattern.

The developer for PMMA is a solution of MIBK (Methyl Isobutyl Ketone) and IPA in a 1:2.5 ratio. This mixture effectively dissolves the exposed PMMA, leaving the unexposed areas intact. The sample is immersed in the developer solution for 30 seconds at 23°C, then immediately rinsed in pure IPA for 30s to stop the development process and remove any residual developer. This step is crucial to prevent overdevelopment, which could lead to pattern distortion. The sample is then rinsed in DI water for 60 seconds to further remove any remaining IPA. Finally, the sample is dried using nitrogen gas to remove any remaining DI water.

The two-layer PMMA system naturally forms an undercut structure during development. The bottom layer (thicker, 15% PMMA) is more sensitive to the e-beam than the top layer (thinner, 4% PMMA). This results in the top layer being slightly more recessed than the bottom layer after development, creating an undercut structure. The undercut structure ensures that during metal deposition, the material deposited on the top surface of the PMMA is not connected to the material deposited on the sidewalls. This separation allows for easier and cleaner removal of the excess material when the PMMA is dissolved, resulting in a more defined and precise pattern on the substrate. After the lift-off process, there may still be traces of resist or other organic contaminants on the surface of the pattern. The sample was then subjected to O_2 ashing at 150W RF power for 150 seconds. This step effectively removes any residues by oxidising the organic material and converting it into volatile compounds such as CO_2 and H_2O.

For the metal deposition step, 30 nm of NiCr (Nickel-Chromium) is first deposited using a metal evaporation machine. NiCr is used as an adhesion layer in metal deposition processes to enhance the bonding between the Au layer and the InP surface. Subsequently, 100 nm of Au is deposited as a high-contrast identification marker.

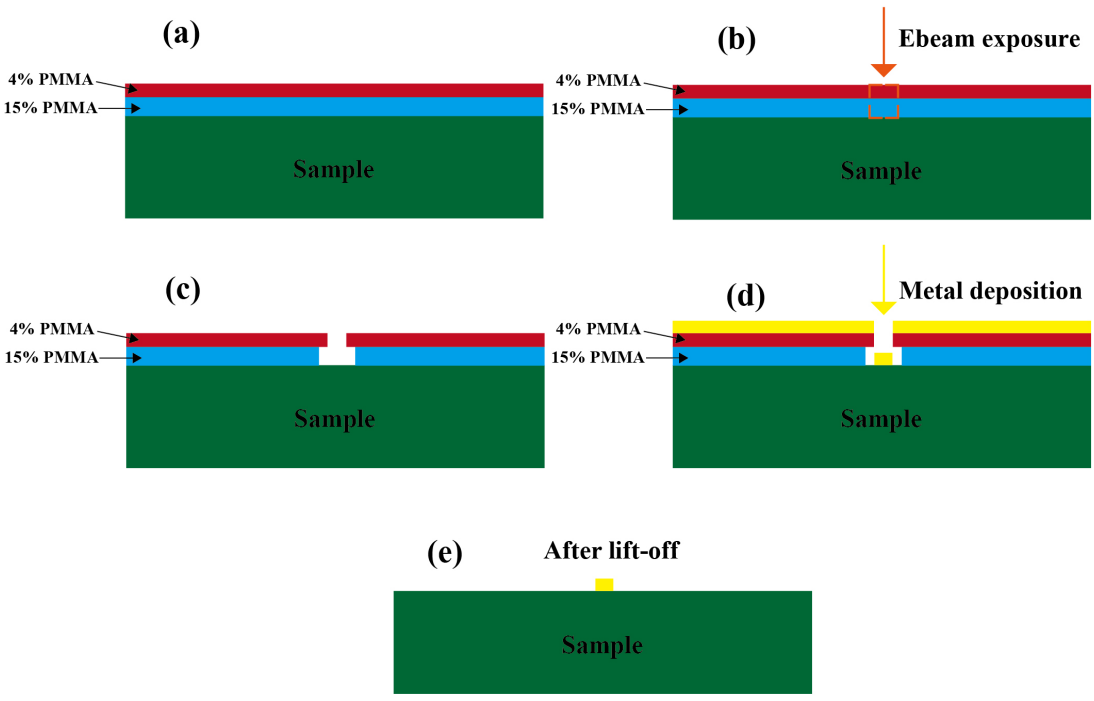

Fig. 3.2. Process flow of metal deposition and lift-off. (a) Double layer PMMA mask spin-coated, (b) e-beam exposure, (c) pattern after development, (d) metal deposition, (e) sample after lift-off.

After metal deposition, the sample is immersed in acetone in a 50°C water bath. The metal outside the patterned areas will be lifted off along with the PMMA, leaving only the

metal adhered to the sample surface in the exposed and developed patterned regions. This process completes the transfer of the mask pattern onto the sample surface.

Fig 3.3 shows the pattern of the markers on the sample, along with a microscope image of the markers after the lift-off process is completed. Note that the long metal line on the left side of the three crosses is used to observe the rotational misalignment between the marker pattern and the edge of the cleaved sample. Since InP has its own crystallographic orientation, the cleaving lines are always parallel or perpendicular to the crystal lattice. If the marker pattern is rotated by more than 1 degree relative to the crystallographic direction, the fabricated devices may have significant misalignment when cleaved into bar strips. This misalignment can result in incomplete devices and cleaved end facets that are not perpendicular to the ridge waveguide. Typically, if the rotational misalignment between the pattern and the sample edge exceeds 1 degree after development, the mask needs to be removed, and the process should be repeated to ensure proper rotate alignment.

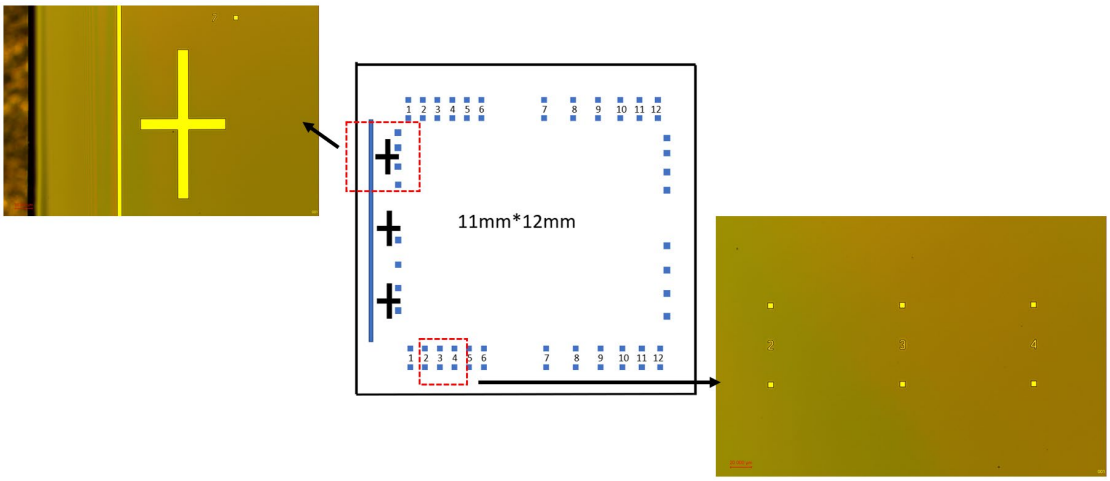

Fig. 3.3. Microscope image of the marker pattern.

3.2 Electrical Isolation and Waveguide Etching

3.2.1 Inductively coupled plasma dry etch

The patterning of electrical isolation and grating waveguides is achieved using inductively coupled plasma (ICP) etching [128-130]. ICP etching is a highly controlled process used in semiconductor fabrication for creating precise patterns on an epilayer wafer by removing material through plasma-based etching.

Fig 3.4 illustrates the basic setup of an ICP etching chamber, the top electrode is set for sustaining the plasma within the chamber. It is connected to an RF power supply, which

typically operates at 13.56 MHz. This RF energy generates a strong electromagnetic field that ionises the process gases, creating a dense plasma. Surrounding the chamber, the wire coil is used to induce the plasma by coupling the RF power into the chamber. This inductive coupling increases the plasma density, which is crucial for efficient etching with high precision and anisotropy. The plasma is composed of ionised gas particles, including ions, electrons, and neutral atoms which are essential for the etching process as it facilitates the removal of material from the substrate through chemical reactions and physical sputtering. The substrate is placed on the bottom electrode which can be biased to control the energy of the ions striking the sample surface, allowing for precise control of the etching profile. The substrate holder often includes a temperature control system, which may use cooling fluids or electrical heating elements. The chamber is connected to a vacuum pump and pressure control valve system, which maintains the required pressure environment necessary for plasma formation and removal of by-products.

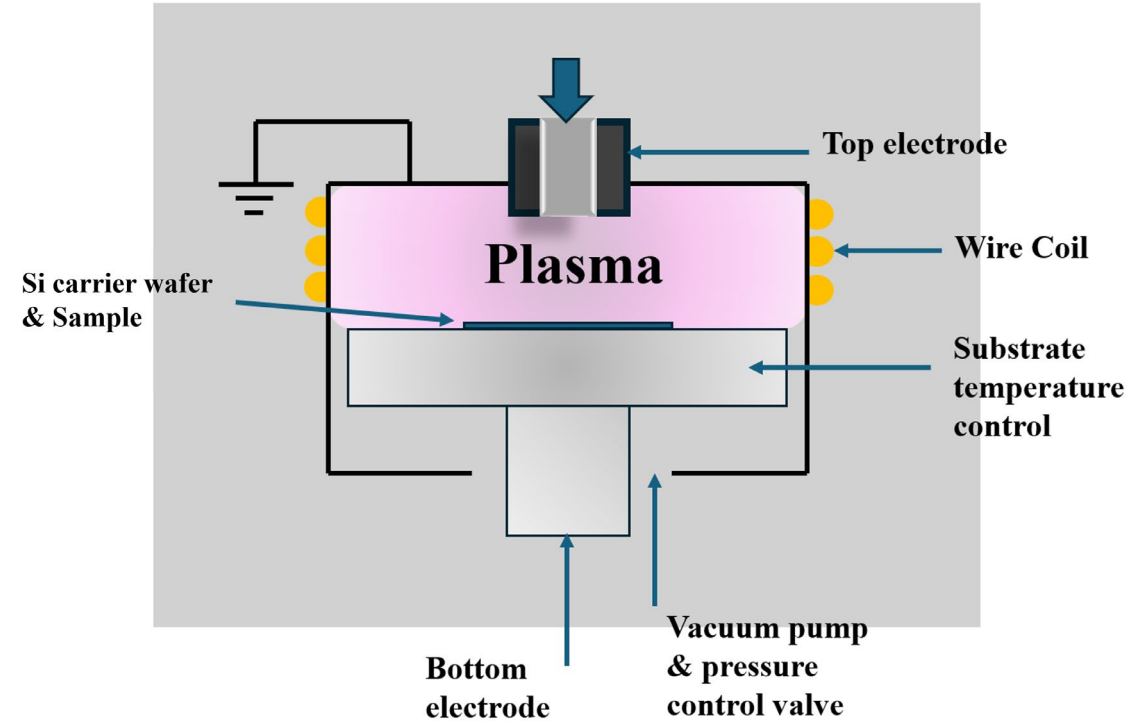

Fig. 3.4. ICP Chamber Schematic.

In an InP based material etching process, a gas mixture of Cl_2 (chlorine), H_2 (hydrogen), CH_4 (methane), and Ar (argon) is used. Chlorine is the main reactive species responsible for etching the InP material [131]. It reacts with the indium (In) and phosphorus (P) in the sample to form volatile by-products such as $InCl_3$ and PCl_3, which are easily removed from the chamber. H_2 can help in surface passivation by reacting with certain species on the substrate, which aids in controlling the etch profile and improving anisotropy. CH_4 contributes to the formation of volatile organic by-products when combined with chlorine. These by-products

can be pumped out, facilitating the clean etching of the material. CH_4 can also assist in improving the anisotropy of the etch by creating a passivating layer on the sidewalls, thus helping to achieve more vertical etch profiles. Ar is an inert gas that does not chemically react with the sample but is used to enhance physical sputtering during the etching process. It helps in the physical removal of material from the surface by providing kinetic energy to the ions in the plasma. Additionally, Ar aids in stabilising the plasma and ensuring consistent etching conditions [132-134].

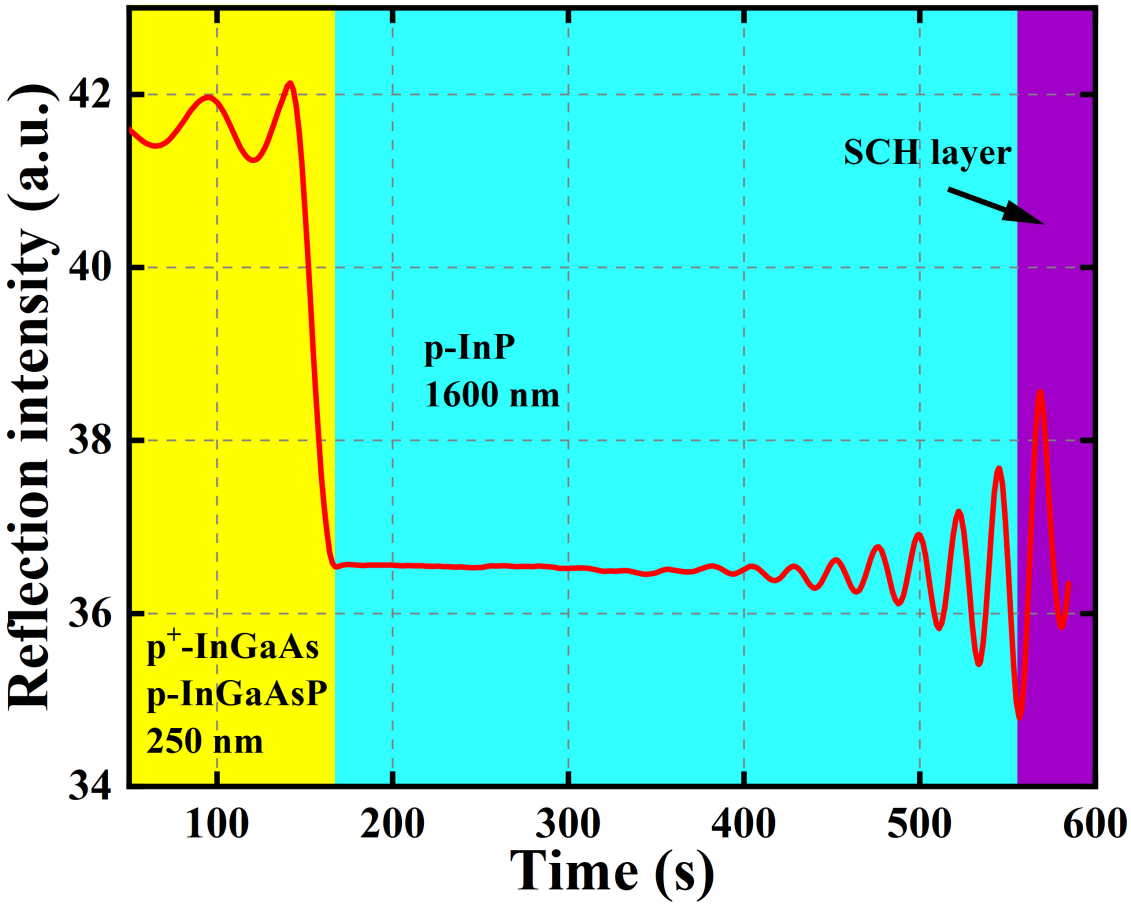

Fig. 3.5. Interferometer trace of 5 QWs wafer.

An interferometer is employed to monitor the etching depth. Its principle involves emitting a 670 nm light beam onto the sample surface and recording the changes in reflected light intensity over the etching duration. Since the wafer consists of multiple stacked layers, the reflected light intensity will vary as the etching progresses, due to interference effects between the different layers. Fig. 3.5 illustrates the interference curve observed during the etching process from the surface down to the completion of the ridge waveguide etching. The yellow region represents the portion that needs to be etched for electrical isolation, which includes a 200 nm p^+-InGaAs contact layer and a 50 nm p-InGaAsP layer (1.3Q). The cyan region corresponds to the upper p-InP layer, with a total thickness of 1.6 μm. Finally, the purple region indicates that the etching has entered the upper SCH layer.

3.2.2 Electrical isolation

Since our laser device consists of two parts, the DFB cavity and the EAM, each requires its own independent electrode. After the marker deposition is completed, the next step is to etch the electrical isolation region over the ridge waveguide. This etching process ensures that the two sections of the device are electrically isolated, allowing for separate control of the DFB cavity and the EAM.

For the electrical isolation region, the heavily doped InGaAs and InGaAsP layers (250 nm in total) on the top of the wafer need to be etched to ensures effective electrical isolation between the different sections of the device, typically reaching around 9 kΩ.

The mask for the electrical isolation pattern is composed of two layers of 15% 2010 PMMA, applied using a spin-coating speed of 4000 rpm, followed by baking at 180°C. Given that the etch selectivity between PMMA and InP in a chlorine-based etching recipe is typically larger than 1:1, the double-layer PMMA provides a total mask thickness of approximately 2.4 μm. This ensures that the mask will not be fully consumed during the etching process. The gas recipe used for the etching process will be detailed in the following subsection 3.2.4. After the dry etching is completed, the sample is immersed in acetone and placed in a 50°C water bath for 30 minutes to dissolve the remaining PMMA mask.

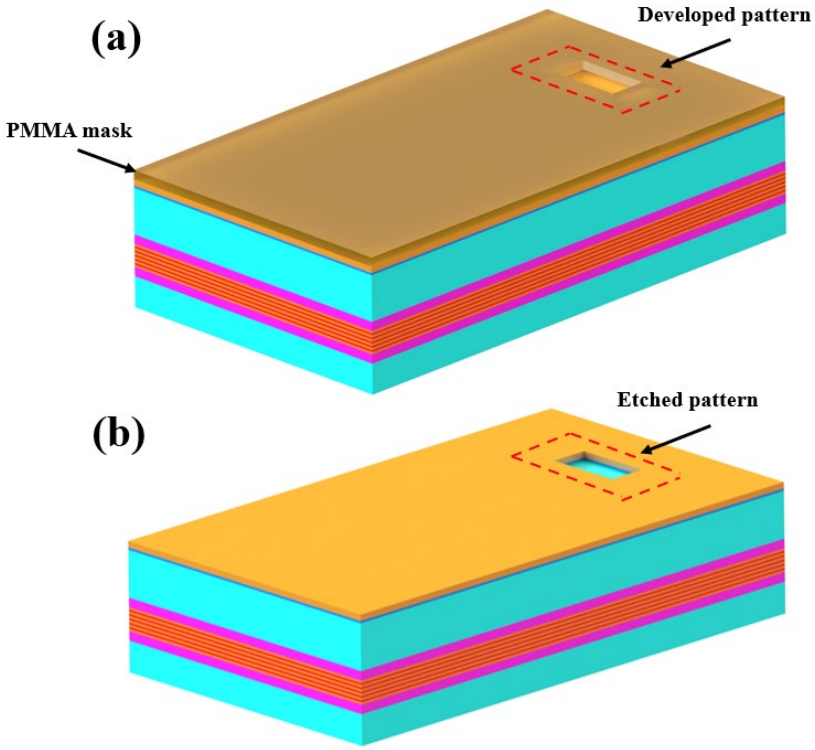

Fig. 3.6. Isolation dry etch process flow, (a) pattern after development, (b) pattern after etching and PMMA mask removal.

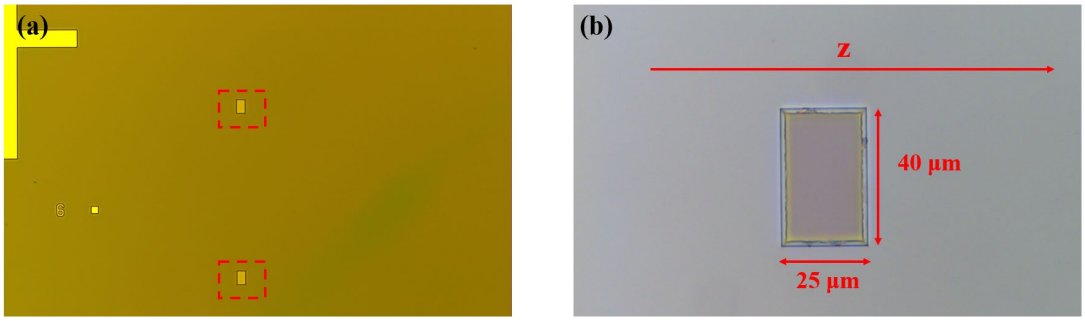

Fig. 3.7. Microscope images of (a) electrical isolation pattern after development, (b) electrical isolation pattern after etching and mask removal.

Fig 3.7(a) and (b) show the microscope images of the electrical isolation pattern after development and after the completion of dry etching, respectively. It is important to note that the length of the electrical isolation along the waveguide direction (z-direction) is set to 25 µm to provide sufficient isolation. The longitudinal length is 40 µm to ensure it fully covers the ridge waveguide. It can be observed that the sidewalls of the electrical isolation pattern exhibit slight scalloped or wavy edges. This may be due to the uneven erosion of the PMMA sidewalls during the etching process.

3.2.3 Sidewall grating waveguide

In current semiconductor DFB lasers, there are mainly two types of gratings, buried gratings (BG) and sidewall gratings [135-140]. For a BG design, the grating pattern is typically etched onto the InGaAsP layer either above or below the quantum wells. Since the optical field is primarily concentrated near the high-refractive-index quantum wells layer, the grating's position in a BG structure allows for strong coupling with the optical field. As a result, etching to a depth of 40-60 nm is usually sufficient to achieve a grating coupling coefficient of 200-300 cm^{-1}. In contrast, in a sidewall grating structure, the grating needs to be etched to a depth of nearly 2 µm, along with the waveguide, to achieve the same level of coupling coefficient as in the BG structure. Additionally, since sidewall gratings narrow the waveguide's width, this structure inherently results in larger waveguide loss.

However, the sidewall grating structure also offers two distinct advantages. First, it eliminates the need for a second epitaxial growth step, which simplifies the device fabrication process and reduces overall production costs. Additionally, since the grating and waveguide patterns are defined simultaneously through a single exposure and etching process, there is no alignment error between the grating and the waveguide. This makes the sidewall grating structure particularly suitable for the fabrication of complex gratings, such as Moiré gratings and superimposed gratings.

For example, in a BG structure, the grating is fabricated first, followed by a second epitaxial growth step. The waveguide pattern is then aligned and etched based on alignment marks. This second alignment step cannot be perfect, which can be detrimental when fabricating Moiré or superimposed gratings. The sidewall grating structure avoids this issue, ensuring precise alignment and better performance in these specialised applications.

For the grating and ridge waveguide patterns, HSQ (Hydrogen Silsesquioxane) is used as the hard mask material [141, 142]. HSQ is composed of a cage-like or network structure of silicon, oxygen, and hydrogen atoms. Its general chemical formula is $[HSiO_{3/2}]_n$, where the silicon atoms are bonded to oxygen atoms and hydrogen atoms, forming a highly cross-linked structure upon exposure. As a negative resist, HSQ becomes insoluble in the developer after exposure to an electron beam, meaning that the exposed areas remain on the sample surface while the unexposed areas are removed away during development. HSQ offers higher pattern resolution compared to PMMA and acts as a hard mask during etching. In the chlorine-based etching system for InP, the selectivity between the target material and the HSQ mask exceeds 5:1. Additionally, HSQ is resistant to lateral erosion, which helps reduce roughness in the etched waveguide and grating structures.

Before spin-coating HSQ, the sample needs to be exposed to an ultraviolet ozone cleaner for 5 minutes. The purpose of this step is to remove any residual resist and organic molecules from the surface, as well as to enhance the adhesion of the HSQ to the sample surface. Subsequently, the sample is spin-coated with HSQ at 2000 rpm, then placed on a hotplate at 90°C for 3 minutes to solidify the resist. At this stage, the thickness of the HSQ mask is approximately 600 nm. After the e-beam exposure is completed, the sample is developed using 25% TMAH (tetramethylammonium hydroxide). The sample is first immersed in 25% TMAH at 23°C for 30 seconds to develop the exposed HSQ pattern, then placed in DI water for 60 seconds to dilute the TMAH and stop the development reaction. Finally, the sample is immersed in IPA for 30 seconds, then dried with nitrogen gas. After development, the sample is first examined using a Scanning Electron Microscope (SEM) to assess the integrity of the pattern and check for any residual HSQ within the grating gaps. If the pattern is incomplete or residues are present, the HSQ mask can be removed using a hydrofluoric acid (HF) treatment, and the patterning process can be repeated.

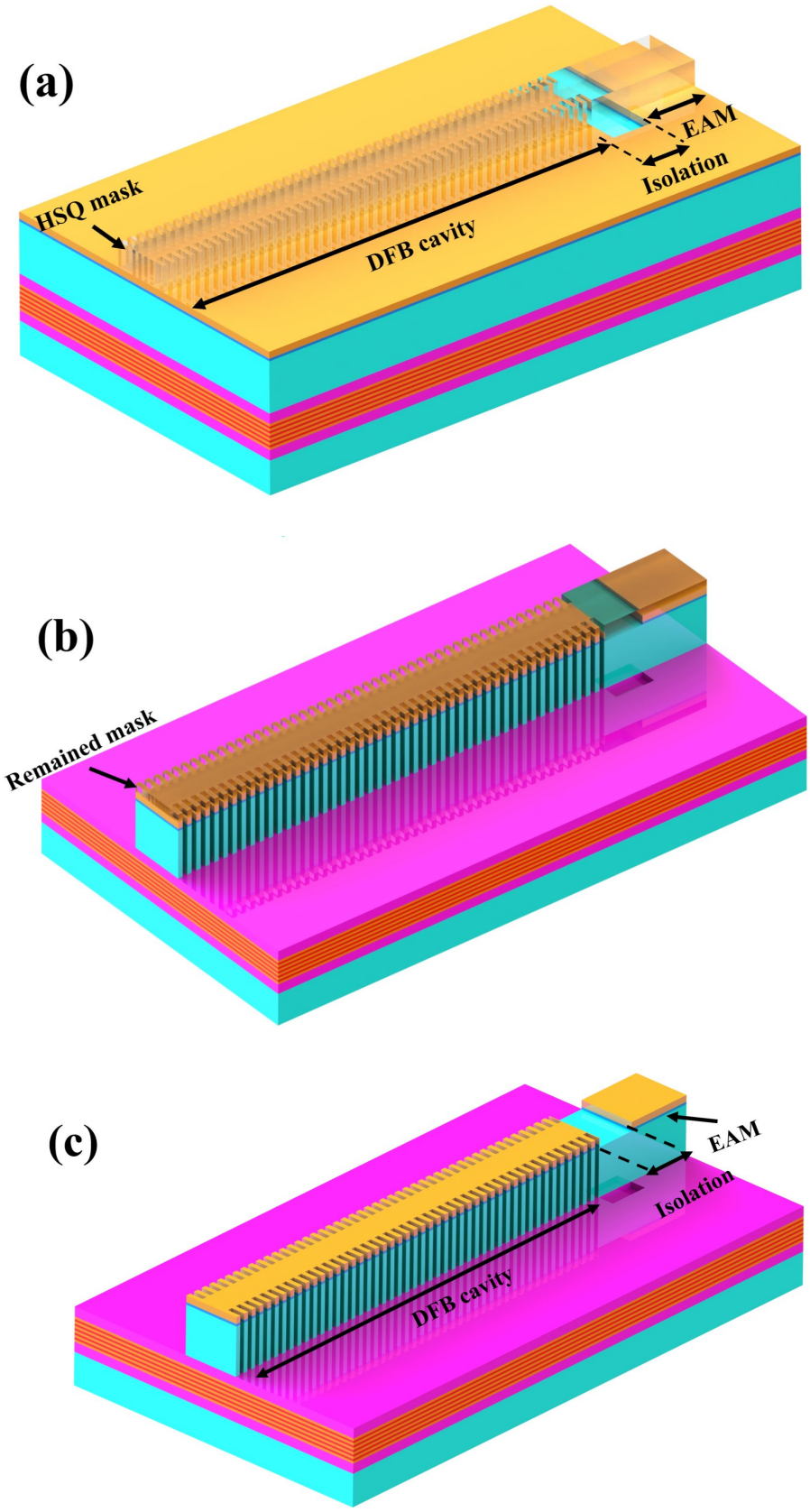

Fig. 3.8. Waveguide definition process, (a) after HSQ mask development, (b) after ICP dry etching, and (c) after removal of remaining HSQ mask.

With the grating and waveguide masks prepared, the sample is placed into the ICP system for dry etching. The complete interferometric monitoring curve for the etching

process is shown in Fig 3.5. It is important to note that after the complete etching of the 1.6 μm p-InP layer, the process needs to continue briefly to reach the target etch depth (1.92 μm). Additionally, due to the non-uniform distribution of the electric field on the sample surface, the etch rate near the edges is slightly higher than at the centre. However, the overall etch depth variation is minimal, ranging between 1.9 μm and 2 μm. The gas recipe used for the dry etching process is detailed in Section 3.2.4. After the dry etching is completed, the remaining HSQ mask is removed using a 6:1 Buffered Oxide Etch (BOE) solution for 3 min at room temperature, preparing the sample for the next processing step.

3.2.4 Optimization of grating dry etching

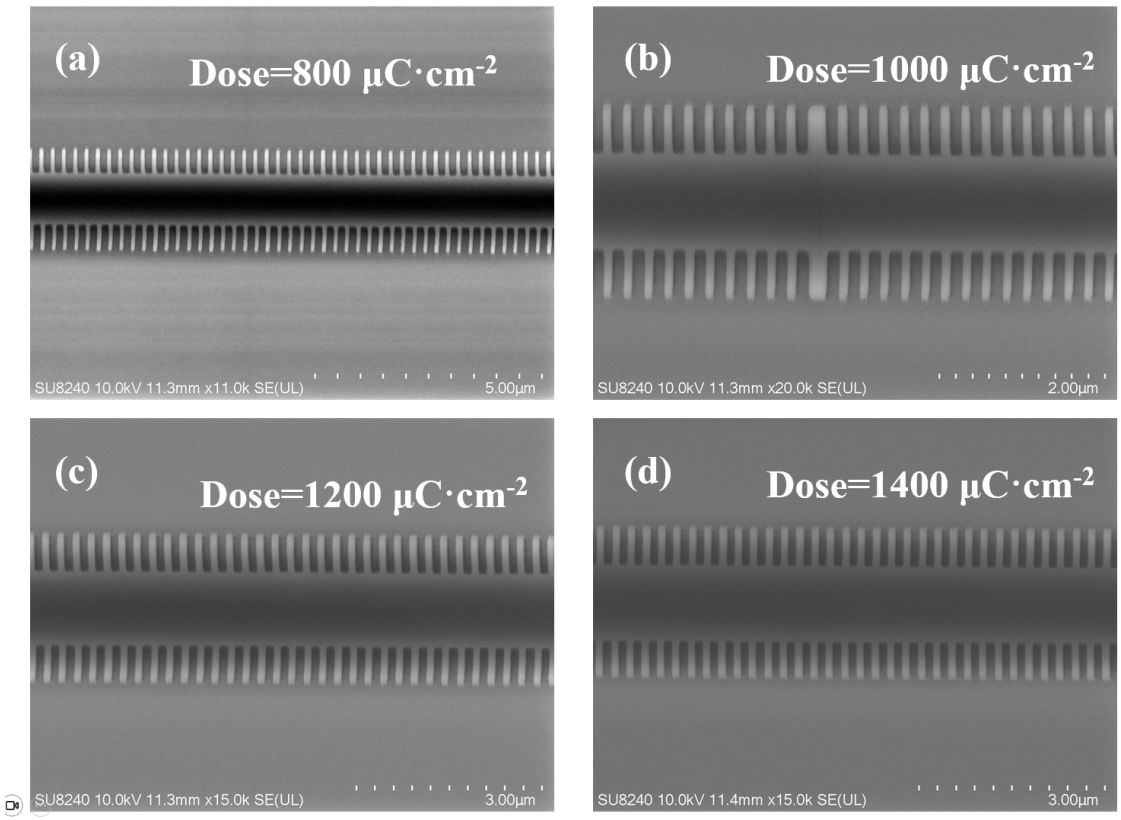

Fig. 3.9. The developed HSQ mask under different e-beam doses.

The grating and ridge waveguide are the core components of the laser. Given that the grating features have dimensions smaller than 200 nm, this etching step is particularly critical.

At JWNC (James Watt Nano-fabrication Centre), advanced EBL machines, along with appropriate Proximity Effect Correction (PEC) schemes, can achieve pattern resolutions beyond 0.5 nm on HSQ resist. Based on this capability, once users have designed their patterns, the first step is to determine the correct electron beam exposure dose. As a negative resist, when the exposure dose is insufficient, the edges of the HSQ mask pattern may be

overly dissolved during development, leading to widened grating gaps or even breaking of the mask pattern. On the other hand, if the dose is too high, the mask pattern may not fully develop, leaving residual resist in the gaps, which can adversely affect the structure after dry etching. As shown in Fig3.9(a), it is evident that at a dose of 800 $\mu C \cdot cm^{-2}$, the grating wall is too narrow. However, in Fig 3.9(c) and 3.9(d), the grating pattern is intact, but there is noticeable residual resist in the gaps. Therefore, a dose of 1000 $\mu C \cdot cm^{-2}$ is selected for the grating and waveguide patterns in this thesis. As shown in Fig 3.10, with a dose of 1000 $\mu C \cdot cm^{-2}$, the grating mask pattern is complete, with sharp edges and no residual resist in the gaps.

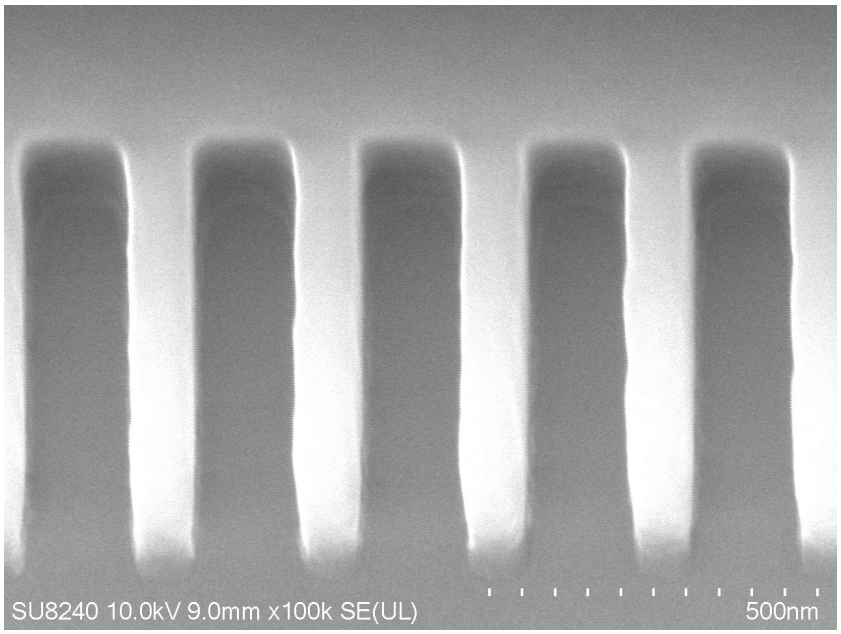

Fig. 3.10 Enlarged HSQ grating mask details with 1000 $\mu C \cdot cm^{-2}$ dose.

For the dry etching process, the Oxford ICP 300 Cobra etcher is used here. The reaction chamber is maintained at a temperature of 60°C and a pressure of 5 mTorr. During etching, the ICP power is set to 750 W, while the power applied to the platen is 100 W. For etching the InP/AlGaInAs system, a mixture of Cl_2, H_2, CH_4, and Ar gases is used, with the roles of each component described in Section 3.2.1. It is noted that Ar is typically not used for etching InP-based quantum well materials due to potential ion damage during dry etching. However, in this case, since the size of the grating grooves is only around 128 nm while the target etching depth is nearly 2 μm, the aspect ratio is excessively high. Therefore, Ar is required to optimize the etching profile. In this process, Cl_2 and Ar primarily perform the etching task, which correspond to chemical etching and physical etching, respectively. During testing, it was found that the grating etch pattern is sensitive to the flow rate of Cl_2. The likely reason is that changing the Cl_2 flow rate alters the ratio of chemical to physical etching. Additionally,

the Cl_2 concentration in the chamber affects the formation and removal of chlorine-containing by-products due to shifts in chemical equilibrium.

After creating the HSQ mask on the wafer, it was cleaved into four sections. Each section was then etched under different Cl_2 flow rates, with the etching endpoint set to the characteristic point at the SCH layer, as indicated in Fig. 3.5. Table 3.1 presents the specific etching recipes used for each section.

Table 3.1 Dry etch gas recipe

Section No.	Cl_2	H_2	CH_4	Ar	Etch time
a	8 sccm	15 sccm	10 sccm	10 sccm	510 s
b	10 sccm				550 s
c	12 sccm				600 s
d	14 sccm				635 s

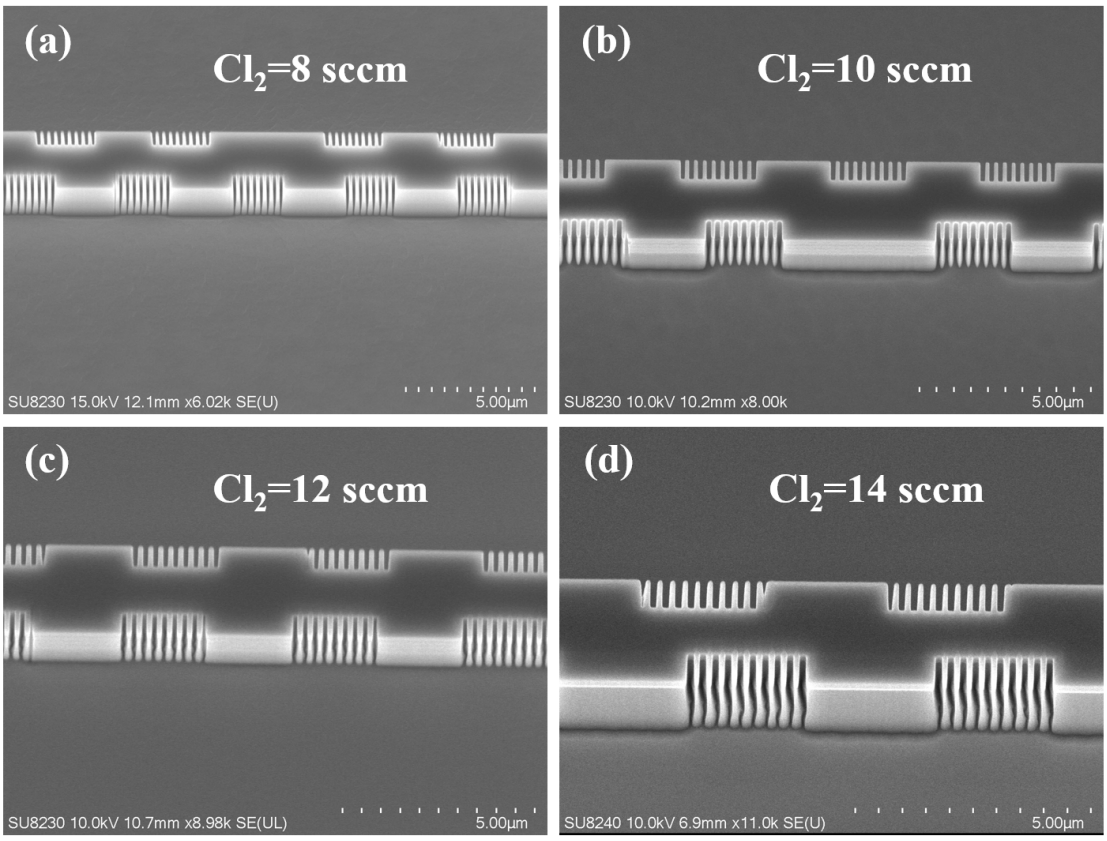

Fig. 3.11 Etched grating waveguide pattern under different Cl_2 flow rates.

As shown in Fig. 3.11, when the Cl_2 flow rate is set to 8 sccm, a significant RIE-lag effect is observed at the bottom of the grating, which shows that the etched grating trenches are narrower than the designed width. In Fig. 3.11(b), At a Cl_2 flow rate of 10 sccm, the

grating trenches were etched all the way to the bottom, with clear visibility, and the grating walls exhibited high verticality. When the Cl_2 flow rate is further increased to 12 and 14 sccm (corresponding to Fig. 3.11 (c) and (d) respectively), the verticality of the grating decreases, and irregular scalloping is observed inside the grating trenches. Therefore, a Cl_2 flow rate of 10 sccm is identified as the optimal etching condition here.

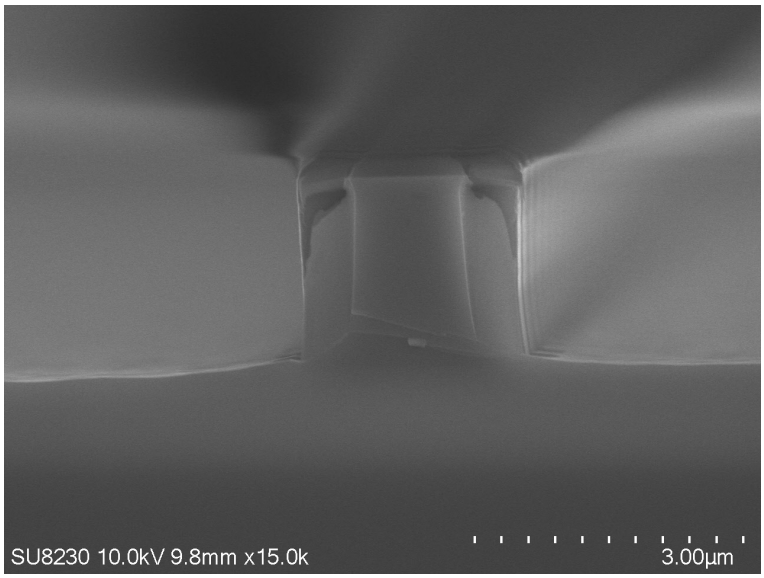

Fig. 3.12 Cross view of the etched grating waveguide under a Cl_2 flow rate of 10 sccm.

Fig. 3.12 is an SEM image of the grating cross-section. It shows that, although the RIE-lag effect has left a portion of the grating trench incompletely etched, the pattern is still sufficient for the grating to function effectively.

3.3 Insulating layer deposition

After completing the etching of the grating and waveguide and removing any residual HSQ mask, an insulating thin film needs to be deposited on the surface of the sample. The purpose of depositing the insulating thin film is twofold. First, the insulating film provides electrical isolation between the device and other areas, ensuring that, after opening contact windows, the current is injected only into the ridge waveguide, thereby improving injection efficiency. Meanwhile, it helps reduce parasitic capacitance in the device, leading to improved modulation speed. Besides, the insulating film acts as a protective layer for the ridge waveguide and grating, enhancing structural stability and preventing oxidation when exposed to air.

Here, the insulating thin film is composed of silicon dioxide (SiO_2) and passivated HSQ. First, a 200 nm thick layer of SiO_2 is deposited using PECVD (Plasma-Enhanced Chemical

Vapor Deposition) at 300°C [143, 144]. The advantage of using PECVD is its good gap-filling capability, particularly in the grating gaps, ensuring uniform coverage and effective insulation. As shown in Fig 3.13, after the first PECVD process, the waveguide surface is covered with a layer of SiO_2, and the grating gaps are uniformly filled. Next, a layer of HSQ is spin-coated onto the sample surface at a speed of 4000 rpm. The sample is then placed in an oven at 180°C and baked for 1 hour to ensure complete curing of the HSQ. Since HSQ initially adheres to the sample surface in liquid form, it transforms the stepped profile of the ridge waveguide into a smooth curved surface. This smoothing reduces the complexity of subsequent metal deposition for the top electrode, making the process easier. Finally, an additional 100 nm thick layer of SiO_2 is deposited on the sample surface using PECVD to further stabilise the overall structure.

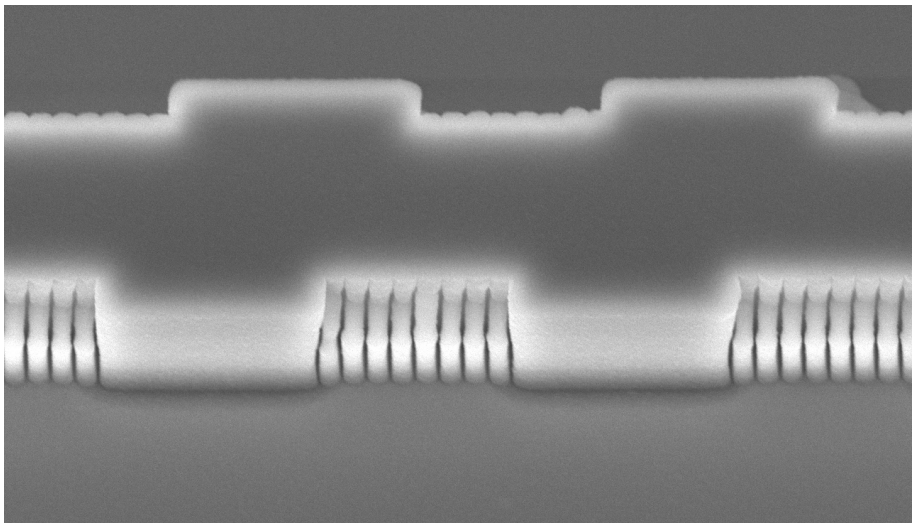

Fig. 3.13. SEM image of the grating waveguide after first 200 nm PECVD SiO_2 deposition.

3.4 Contact window opening

After completing the deposition of the insulating layer on the sample surface, the next step is to perform a "window opening" process in the areas where current injection is required. This involves etching away the insulating layer in these specific regions to expose the underlying ridge waveguide for subsequent metal contact deposition.

Similar to the electrical isolation step, a mask is first created using two layers of 15% PMMA. The areas that need to be etched are then exposed and developed to define the regions where the insulating layer will be removed. For etching the insulating layer, a Reactive Ion Etching (RIE) system is used [145]. In RIE, the plasma is generated by applying RF power directly to the substrate electrode (which also serves as the bottom electrode). This

RF power ionises the gases in the chamber, creating plasma. Although ICP typically offers higher etch anisotropy and aspect ratios, RIE is adequate for this task because the window opening patterns are usually on the micron scale size.

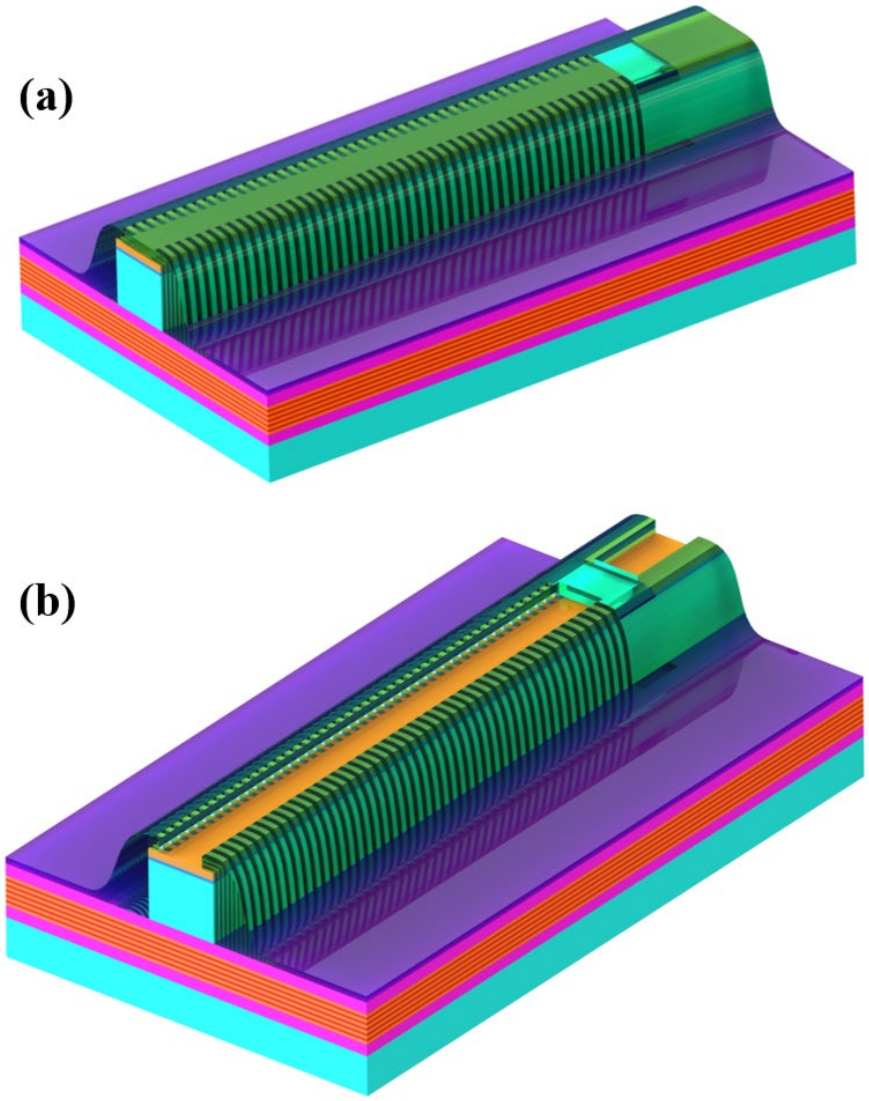

Fig. 3.14. Schematic of the sample (a) protected by insulating layer, (b) after window opening.

It's important to note that the width of the window opening should be slightly smaller than the width of the ridge waveguide to ensure that the top electrode does not connect to the regions on either side of the ridge waveguide. In this case, with the ridge waveguide width set at 2.5 μm, the window opening width is set to 1.3 μm.

CHF_3 (Trifluoromethane) and Ar are the reactive gases used for etching SiO_2, with flow rates of 25 sccm and 15 sccm, respectively. The reaction chamber is set at a pressure of 30 mTorr, with a temperature of 20°C, and an RF power of 150 W. Under these conditions, the etch rate for SiO_2 is approximately 22 nm per minute, while the etch rate for cured HSQ is

slightly higher. The etch depth is monitored using an interferometer. Since this recipe has minimal reactivity with top p^+-InGaAs, the monitoring curve will show no further changes once the SiO_2 etching is complete. After the SiO_2 etching is complete, the residual PMMA mask is removed by processing the sample with O_2 at a flow rate of 50 sccm in the same reaction chamber environment for 5 minutes.

3.5 P-contact electrode deposition

After the window opening process is complete, the next step is the evaporation of the top P-electrode. Similar to the metal evaporation process used for the marker, three layers of PMMA are spin-coated onto the sample. The first two layers have a concentration of 15%, while the final layer has a concentration of 4%. The spin speed is set to 4000 rpm. Each layer is baked to harden, the first layer is baked for 4 minutes, the second for 5 minutes, and the final layer for 6 minutes.

Compared to the metal marker deposition steps, an additional layer of 15% PMMA is used here. This is because, during the spin-coating of the resist, the raised ridge waveguide area tends to have a thinner resist layer compared to the flat regions. The use of three layers of PMMA ensures that a sufficiently thick resist layer covers the ridge waveguide, which is crucial for a successful lift-off process.

After exposure and development are completed, the sample is first treated with an O_2 asher (150 W for two minutes) to remove any residual PMMA in the developed pattern. Following this, to reduce the contact resistance of the device, the sample is immersed in a 1 HCl (hydrochloric acid):5 H_2O solution for 90 seconds. The diluted HCl etches away the oxidised layer on the surface of the p+-InGaAs, ensuring a cleaner surface for subsequent metal deposition and improving the electrical contact quality.

Subsequently, layers of 30 nm Ti (Titanium), 30 nm Pt (Platinum), and 240 nm Au are sequentially deposited using thermal or electron-beam evaporation [146, 147]. Ti acts as an adhesion layer, ensuring that the subsequent metal layers bond well to the underlying semiconductor material. Pt serves as a barrier layer to prevent diffusion between the titanium and gold layers, maintaining the integrity of the metal stack. Au provides excellent conductivity and oxidation resistance, forming the main conductive layer for the top electrode. Similarly, after the metal deposition is complete, the sample is placed in a 50°C water bath with acetone to facilitate the lift-off process.

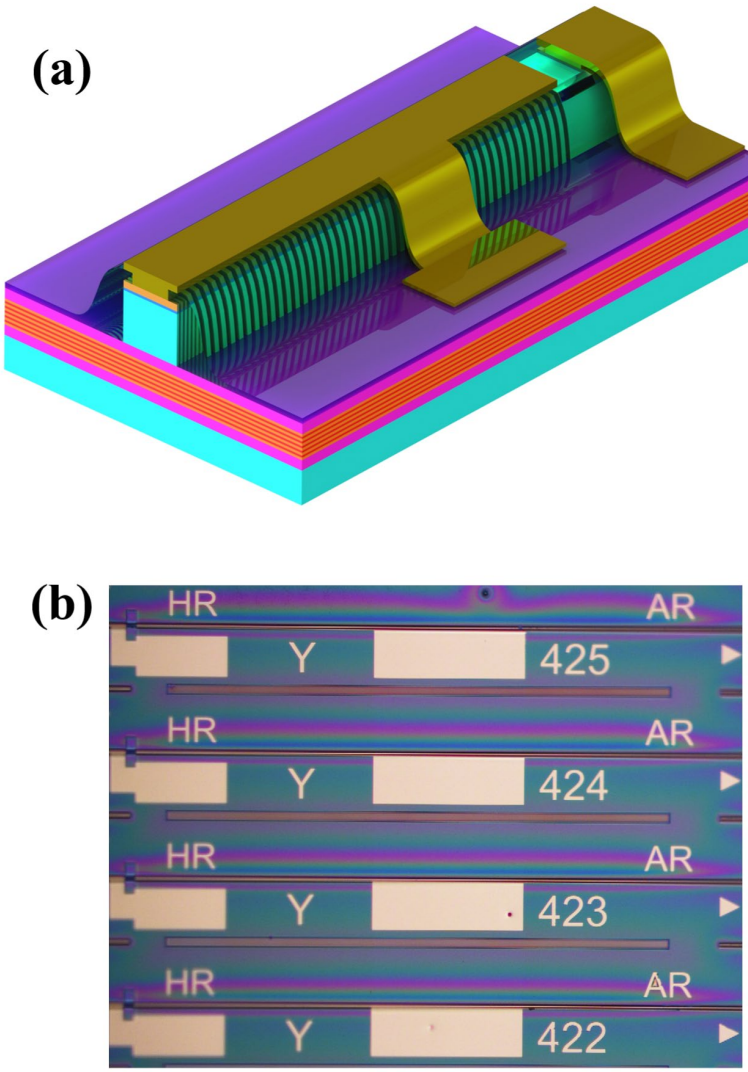

Fig. 3.15. (a) Schematic device after P-contact electrode deposition, (b) microscope image of the fabricated sample.

3.6 Thinning, N-contact electrode and cleaving

To further reduce the device's electrical resistance and improve thermal conductivity, the next step involves thinning the sample. First, a 9 µm alumina suspension is poured onto frosted glass to serve as a physical thinning substrate. The sample is then subjected to the thinning process using this setup. The entire thinning process is performed manually, the alumina suspension acts as an abrasive material, enabling controlled and uniform thinning of the sample to achieve the desired thickness while maintaining the integrity of the device. Given that the initial wafer thickness is 370 µm and the target device thickness is approximately 200 µm, the total thinning required is around 170 µm. When approximately 10 µm of the target thinning thickness remains, the 9 µm alumina suspension is replaced

with a 3 µm alumina suspension which is used for polishing the bottom surface of the sample, ensuring a smoother and more uniform finish.

After polishing is completed, the next step is the deposition of the N-contact electrode. This process does not require a mask, the metal is directly deposited across the entire backside of the wafer. The N-contact electrode consists of a metal stack with the following layers, Au/Ge (Germanium)/Au/Ni (Nickel)/Au with thicknesses of 14/14/14/11/240 nm, respectively [148, 149].

Ge and Si, which is used for doping n-type InP, are both group IV elements. When deposited and subsequently annealed, Ge diffuses into the n-InP, increasing the local doping concentration at the interface. This helps in reducing the Schottky barrier height, facilitating the formation of an ohmic contact. The first thin layer of Au serves multiple roles. It acts as a medium to carry the Ge into the semiconductor during annealing and helps in the diffusion process. Additionally, Au provides good electrical conductivity and forms a stable contact with the underlying layers. Ni acts as a diffusion barrier, preventing the intermixing of the Au and Ge layers with the subsequent Au layers. Ni also improves the adhesion of the contact to the semiconductor and enhances the overall stability of the contact. The final thick layer of Au provides excellent electrical conductivity and serves as the primary contact layer for external connections. Au is also resistant to oxidation, ensuring long-term stability of the contact.

The sample will then undergo an annealing process at 380°C for 1 minute. This annealing step is designed to improve the quality of the metal-semiconductor interface, enhance dopant activation, and reduce contact resistance, thereby optimising the electrical performance of the device [150, 151].

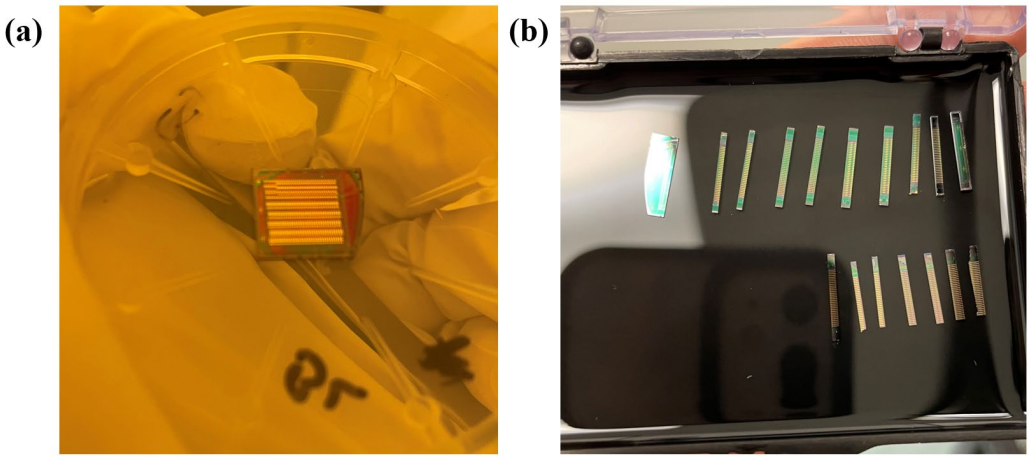

Fig. 3.16. (a) Sampled after annealing, (b) cleaved laser bars.

Once the annealing process is completed, the fabrication process for the entire sample is nearly finished. The final step involves cleaving the sample along the crystallographic direction and the designed length to form bar strips, exposing the device end facets, which will then be ready for testing.

3.7 Chapter summary

This chapter introduced the device fabrication process, which consists of the following sequential steps, marker deposition, electrical isolation etching, grating and ridge waveguide etching, insulating film deposition, contact window opening, P-electrode deposition, wafer thinning, N-electrode deposition, annealing, and cleaving.

The most challenging and critical step in the process is the etching of the grating and ridge waveguide. In this chapter, an optimal recipe is provided for this fabrication step.

Chapter 4: Experimental results

In this chapter, the experiment setups and results for three types of dual-wavelength lasers and their arrays will be presented, including measurements of optical spectra, output power, frequency spectra, and autocorrelation trace.

4.1 Laser testing platform

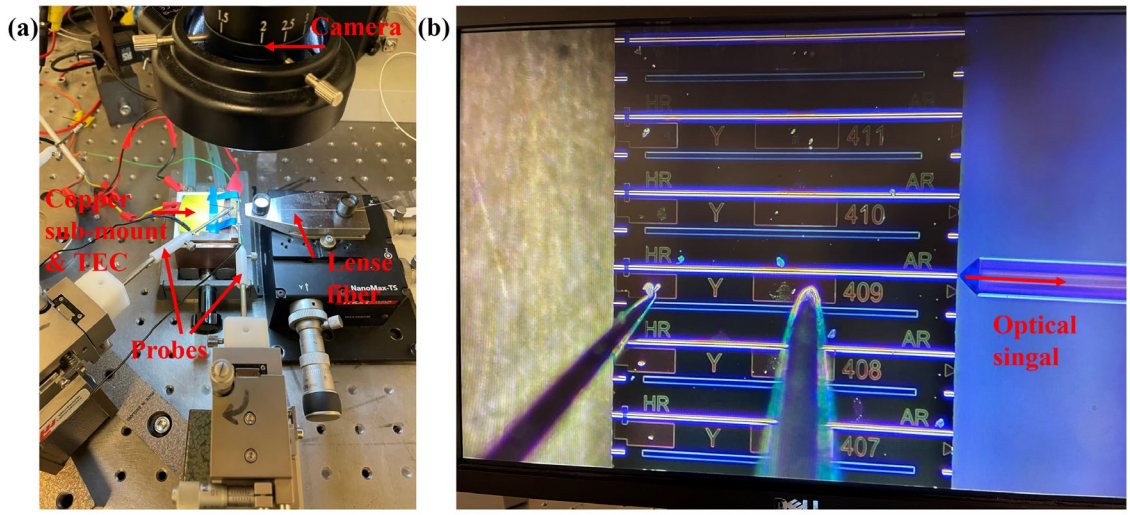

Fig. 4.1. (a) Image of the testing platform setup, (b) image from the microscope camera.

As shown in Fig 4.1(a), the cleaved laser bar is placed on a copper sub-mount. The copper sub-mount can be connected to ground as needed to directly ground the backside of the laser. Below the sub-mount, a semiconductor thermoelectric cooler (TEC) is secured with thermal adhesive, allowing for temperature tuning. Additionally, a thermistor is attached to the setup to monitor and provide temperature feedback. The backside of TEC is connected to a water-cooled heat sink using thermal adhesive to effectively dissipate heat.

A microscope camera system is positioned above the laser bar to observe the setup and apply probes. The laser's optical signal is emitted from the facet and coupled into a lensed fibre as shown in Fig 4.1 (b). The coupled optical signal is then directed coupled to different testing instruments according to the experimental requirements.

During testing, all instruments, including the current source, spectrometer, and optical power meter, are controlled by LabVIEW programs. This system automatically adjusts the experiment conditions and collects the corresponding data.

4.2 Two π phase shifts grating with equivalent chirp structure

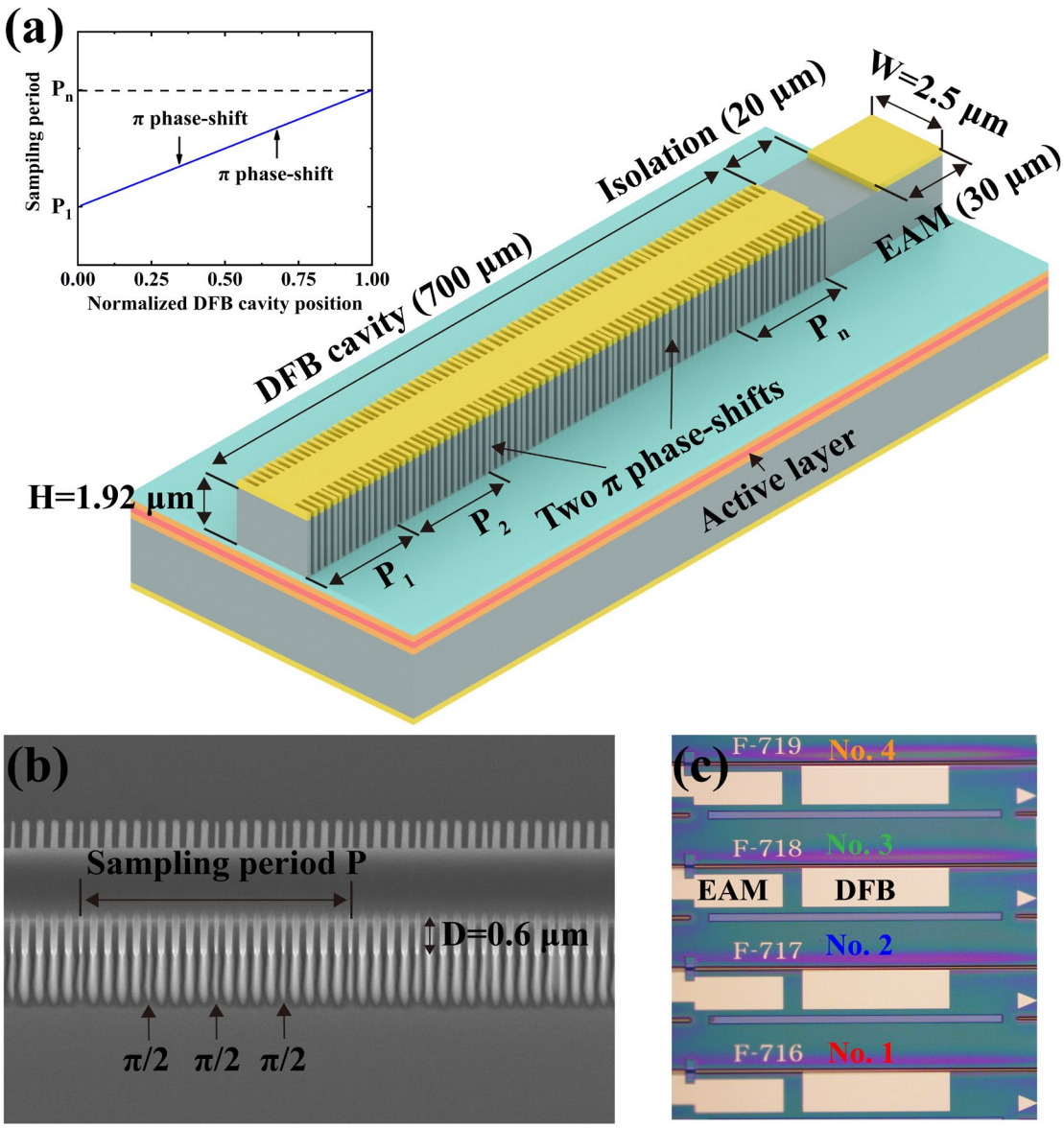

Fig. 4.2. (a) Schematic of the proposed device, the inset shows the sampling period distribution along the cavity. (b) SEM image of the etched ridge waveguide and 4PS sidewall grating. (c) Microscope image of the DWL array.

The first demonstrated array is based on two π phase shifts and an equivalent chirp structure. The epitaxial structure of the device emitting at 1.55 μm is based on an AlGaAsIn-InP heterostructure as reported in section 2.5, and the fabrication process is the same as described in chapter 3. A schematic of the fabricated device is shown in Fig 4.1(a). The device comprises an EAM section (30 μm), and a DFB section (700 μm), separated by an electrical isolation (20 μm). In Chapter 2, the effect of the end-facet phase on dual-wavelength lasing

was explained. The integrated EAM at the device's end-facet is used to tune the phase relationship of the two lasing modes. By applying different reverse biases, the EAM primarily induces differential absorption for the two lasing wavelengths, thereby influencing the overall optical feedback. Additionally, the refractive index in this region changes, and together, these two factors adjust the phase relationship of the feedback light [152-154]. The ridge waveguide width W is 2.5 μm and the height H is 1.92 μm; the effective refractive index of the guide mode (TE_0) is estimated to be 3.19. Both sidewalls have the same uniform seed grating with a period of 257 nm and a recess depth D of 0.6 μm.

As shown in the inset in Fig 4.2(a), the sampled periods are linearly modulated along the DFB laser cavity to achieve the equivalent chirp modulation, the chirp rate being defined as the ratio of the difference between the first and last sampling period (P_n-P_1) to the length of the DFB cavity. Two π phase shifts are introduced at positions 1/3 and 2/3 along the length of the DFB cavity to ensure dual-wavelength lasing. Fig 4.2(b) is a SEM image of the etched ridge waveguide and 4PS sidewall grating. In the 4PS structure, the grating in each sampling period being evenly divided into four sections, with each adjacent grating section subjected to a π/2 phase shift. Compared to a conventional SBG in which half of the sampling period has no grating, the 4PS structure retains a high grating coupling coefficient in $+1^{st}$ order channel, while suppressing the 0^{th} order reflection. Fig 4.2(c) is a microscope image of the fabricated four DWLs array. The four devices (No.1 to No.4) have the same structure but different chirp rates of 30 nm/mm, 50 nm/mm, 70 nm/mm, and 90 nm/mm, respectively. After fabrication, the laser chip was cleaved into bars, with both facets left uncoated.

Testing of the devices was carried out under continuous-wave (CW) conditions, with the laser array mounted on a copper heat sink at 20 °C. The optical outputs were measured from the DFB facet using an OSA with 0.06 nm resolution bandwidth (RBW). Fig. 4.3 depicts the operational characteristics of the device with a chirp rate of 30 nm/mm, with the EAM biased at –1.7 V (V_{EAM}=−1.7 V). It can be observed that the device exhibits a favourable dual-mode operation state when the DFB injection current (I_{DFB}) is within the range of 45-81 mA, and due to the presence of facet reflections, the device experiences mode hopping at 82 mA [155].

Fig. 4.4(a) shows the power margin (PM) between λ_1 and λ_2, sidemode suppression ratio (SMSR), and wavelength spacing (Δλ) under different I_{DFB}. When I_{DFB} exceeds 55 mA, the PM remains within 3 dB, and it is less than 0.5 dB when I_{DFB} is between 70-80 mA; a lower PM is beneficial for improving the quality of the beating signal. When I_{DFB} is larger than 45 mA, the SMSR consistently remains above 30 dB. The wavelength separation, Δλ, falls in the range of 0.539 nm to 0.551 nm, with a variation of 0.012 nm. Considering that this

variation is smaller than the RBW of the OSA, the Δλ is independent of the injection current, implying that the beat signal's centre frequency is relatively stable. Fig. 4.4(b) displays the measured spectrum when V_{EAM}=−1.7 V and I_{DFB}=75 mA. The results are consistent with the simulation, clearly showing the presence of two lasing modes and two FWM signals. It should be noted that significant FP modes are also observed in the spectrum due to the presence of facet reflections.

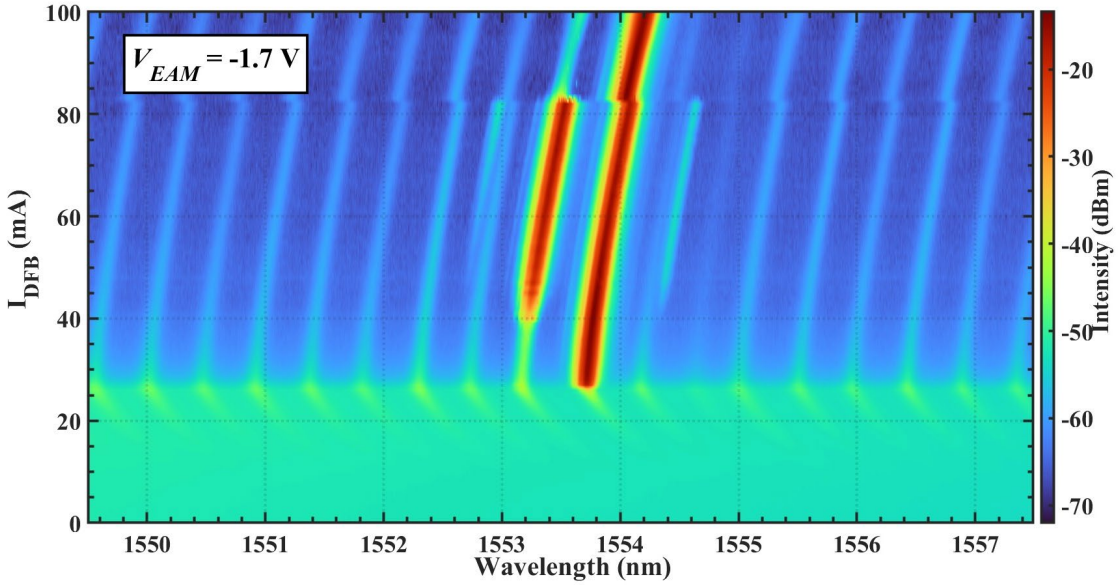

Fig. 4.3. 2-D optical spectrum map of a laser with 30 nm/mm chirp rate when V_{EAM}=−1.7 V.

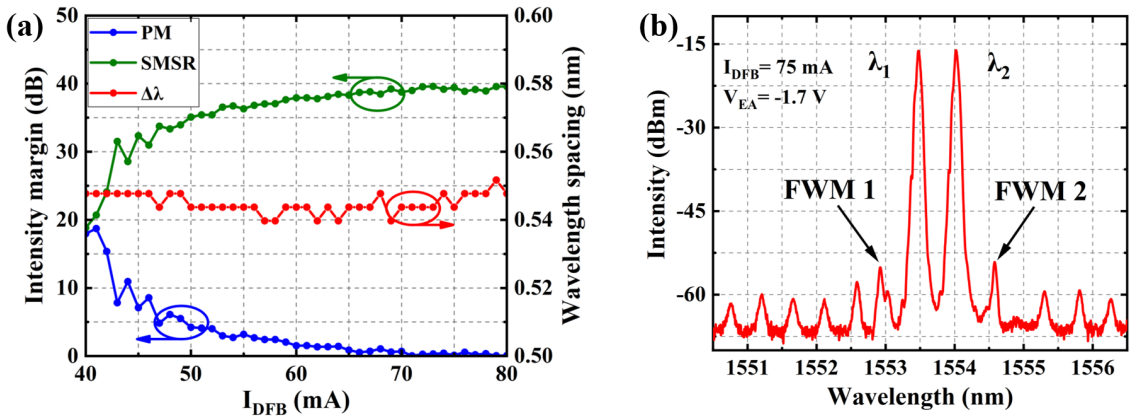

Fig. 4.4 (a) PM, SMSR, and Δλ versus I_{DFB}. (b) Measured optical spectrum of the laser when I_{DFB}=75 mA, V_{EAM}=−1.7V.

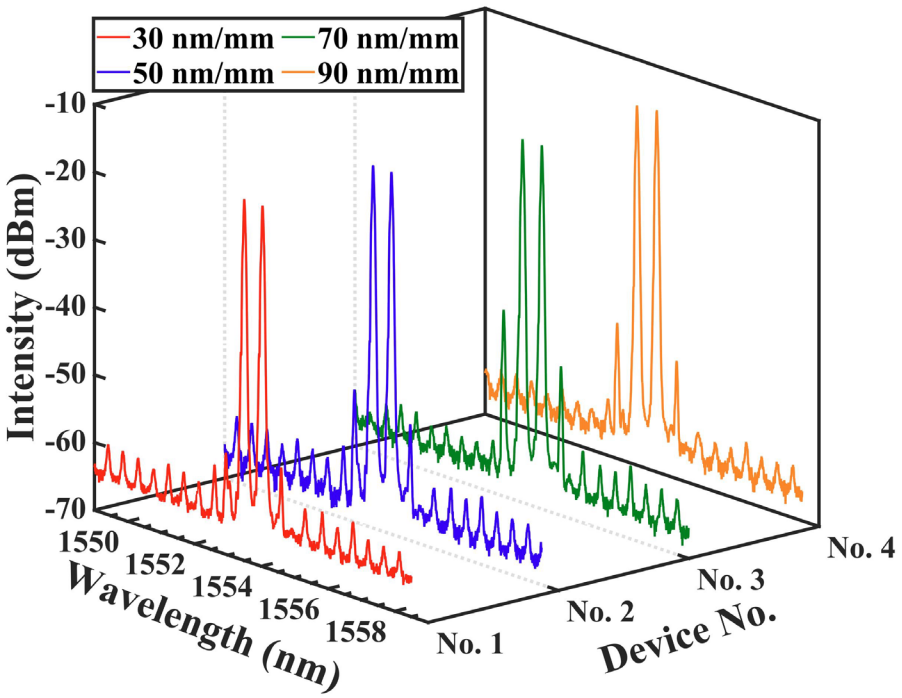

Fig. 4.5 Measured optical spectrum of the DWLs with different chirp rates.

Table 4.1 Parameters of the array

Device No.	Chirp rate	I_{DFB}	V_{EAM}	Δλ
No. 1	30 nm/mm	75 mA	−1.7 V	0.539 nm
No. 2	50 nm/mm	98 mA	−1.2 V	0.549 nm
No. 3	70 nm/mm	128 mA	−0.6 V	0.575 nm
No. 4	90 nm/mm	145 mA	−1.9 V	0.595 nm

The measured spectra and operating parameters of the array are shown in Fig. 4.6 and Table 4.1, respectively. Fig. 4.5 shows typical spectra of the four devices with different chirp rates, each demonstrating good dual-mode characteristics with clear visibility of the FWM signals. Meanwhile, due to the facet reflection caused by cleaving, each device exhibits FP modes in the spectrum. However, these FP modes have a minimal impact on the beat frequency signal as the power ratio between the main modes and the FP modes is higher than 45 dB.

According to Table 4.1, a larger chirp rate results in a larger wavelength difference, which is consistent with the simulation results shown in Fig. 2.11 (d). Additionally, it can be observed that devices with larger chirp rates require higher injection currents to achieve stable dual-wavelength lasing. This phenomenon can be attributed to an increase in chirp rate leading to an increase in the threshold gain margin between λ_1 and λ_2. As a result, the device requires a higher injection to compensate for the weaker mode, thereby achieving equal output power for λ_1 and λ_2.

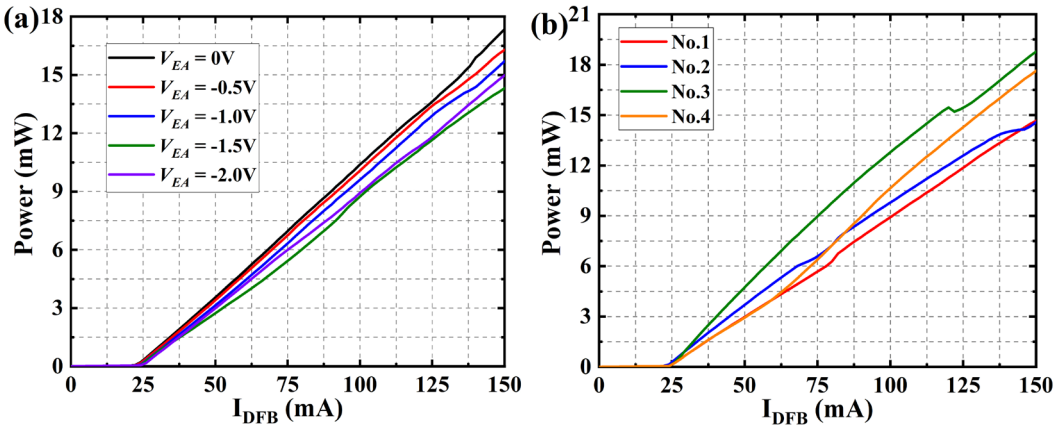

Fig. 4.6 (a) Measured P-I curves of the device with 30 nm/mm chirp rate under different V_{EAM}, (b) P-I curves of the devices with different chirp rate for values of V_{EAM} shown in Table 4.1.

Fig. 4.6 (a) shows typical power-injection current (*P-I*) characteristics from the DFB output side under different V_{EAM} with a scan step of 2 mA. The threshold current and output facet slope efficiency with 0 V applied to the EAM section were 24 mA and 13.8% W/A, respectively. When the EAM reverse voltage was increased from 0 V to –1.5 V, the threshold current was unchanged, but the slope efficiency was reduced as a result of increase in interband and exciton absorption. With a further increase of the reverse voltage to –2.0 V, the DFB laser became optically isolated from the facet reflection and the slope efficiency increased, with the threshold current still unchanged. This indicates that the DFB laser was working as an independent cavity and the partitioning electrical slot prevented electrical coupling between the DFB and EAM sections. Fig. 4.6 (b) shows the *P-I* curves of the 4 devices under the V_{EAM} values shown in Table 4.1. Within the limit of 2 mA scanning steps, the threshold currents of the different devices are the same at 24 mA. However, the four devices exhibit different slope efficiencies which can be attributed to the fact that the devices operate at different V_{EAM}, and the different grating coupling coefficients resulting from different chirp rates also affect the efficiency [156]. It can be seen that there are some kinks in the P-I curves, which are indicative of mode hopping phenomena. For example, in the *P-I* curve of device No. 1 (red line in Fig. 4.6(b)), a kink is observed at 82 mA, corresponding to the mode hop seen in Fig. 4.3.

The RF signal was measured using a PD connected to an electrical spectrum analyser (ESA), as shown in Fig.7. The optical signal was coupled by a lensed fibre from the front facet of the device. The fibre was connected to an erbium doped fibre amplifier (EDFA) via an optical isolator and polarisation controller (PC). The optical isolator prevents amplified light from being reflected back to the device through the lensed fibre. The amplified optical signal was converted into an electrical signal by a PD (u^2t Photonics XPDV2020R 50 GHz)

and then sent to an external mixer (Keysight 11970V) via a coax-to-rectangular waveguide connector. The function of the diplexer is to separate/combine the LO/IF signal for the ESA (Keysight N9020B).

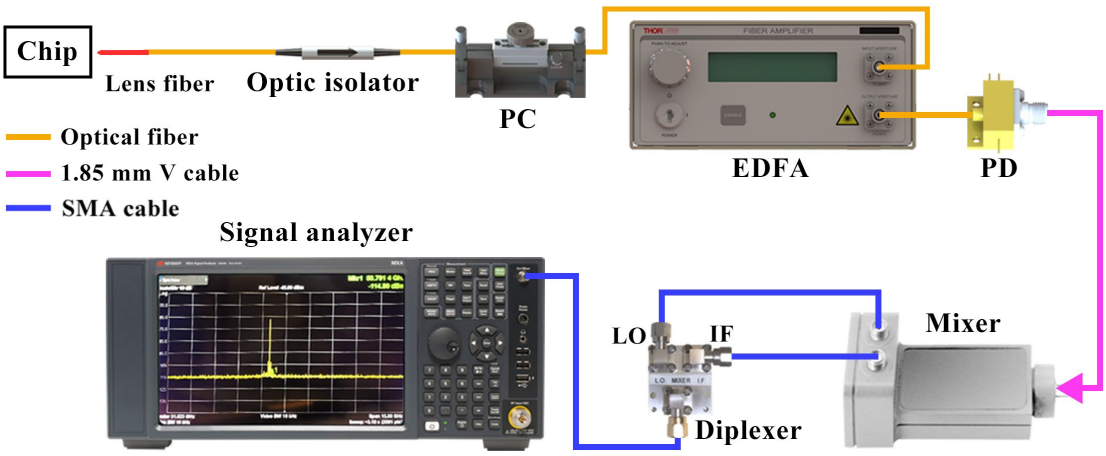

Fig. 4.7 Schematic of the RF signal measurement system.

Fig. 4.8 (a) shows the RF signals of the array measured under the conditions shown in Table 1. The ESA was set with an RBW of 100 kHz and a scanning range of 15 GHz. Consistent with the simulation results, the device with a higher chirp rate has an RF signal at a higher frequency. The variation of the RF linewidth with I_{DFB} is shown in Fig. 4.8 (b). Since the RF signal is generated by beating λ_1 and λ_2, the linewidth of the signal is primarily influenced by three factors. One factor is the PM between λ_1 and λ_2, and when the PM is too large, the beat signal will become poor or even undetectable. The second factor is that the linewidth of the optical signal tends to decrease as the injection current increases [157]. The third factor is the facet reflection from the DFB side (up to 30%), which can induce self-injection effects in the device, also leading to a reduction in linewidth [158]. Fig. 4.8 (c) shows the fitted linewidth of the device with 70 nm/mm chirp rate under V_{EAM}=−0.6 V, I_{DFB}=128 mA. During the linewidth measurement, the ESA was set with an RBW of 51 kHz and a scanning range of 80 MHz, and the –3 dB linewidth was obtained by measuring the –20 dB bandwidth and dividing it by $\sqrt{99}$ to reduce the measurement error [159]. The performance of the device was also assessed as a function of heat sink temperature over the range from 10 °C to 30 °C in steps of 2 °C. From Figs 4.8 (d) and (e), it is evident that within this temperature range, the device maintains dual-wavelength operation.

It is important to note that, despite the increase in effective refractive index of the waveguide due to the rising temperature causing both modes to experience a redshift, the $\Delta\lambda$ remains constant. This is because the two lasing wavelengths are generated within the same DFB cavity and the rate of temperature-induced wavelength shift is the same for both wavelengths. The increase in temperature leads to a redshift in the gain peak, causing an imbalance in gain between the two modes and an

increase in PM. According to Fig. 4.8 (f), the RF frequency decreases slightly with increasing temperature due to the overall redshift of the two lasing wavelengths (Considering that the wavelength difference remains constant, but the central wavelength continues to increase). The relationship between the beat frequency and the central wavelength λ_c can be calculated by Eqn. 4.1 when $\Delta\lambda$ remains constant. The deterioration in the RF signal-to-noise ratio (SNR) is caused by the increased PM. The RF signal frequencies and lowest measured linewidths of the array at 20 °C are shown in Table 4.2.

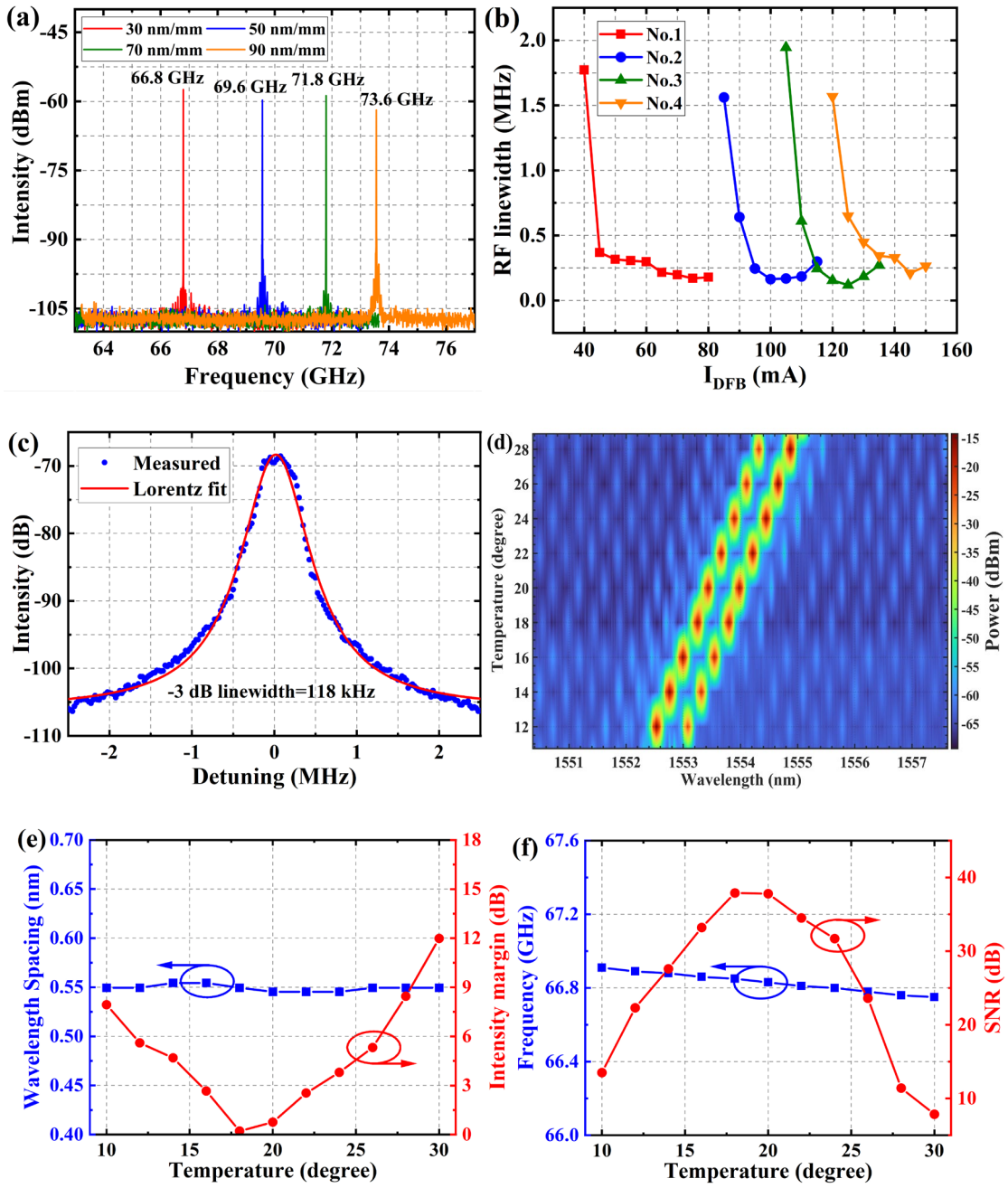

Fig. 4.8. (a) Measured RF signals of the DWL array, (b) RF signal linewidth of the array versus I_{DFB}, (c) fitted linewidth curve of the device with 70 nm/mm chirp rate, (d) 2-D optical spectrum, (e) wavelength spacing and PM, (f) RF frequency and SNR versus TEC temperature of the device with 70 nm/mm chirp rate under I_{DFB}= 75 mA and V_{EAM}= −1.7 V.

$$f = \frac{c \cdot \Delta\lambda}{(\lambda_c + 0.5\Delta\lambda)(\lambda_c - 0.5\Delta\lambda)} \tag{4.1}$$

Table 4.2 RF signal frequency and linewidth

Device No.	I_{DFB}	V_{EAM}	Frequency	Linewidth
No. 1	75 mA	−1.7 V	66.8 GHz	170 kHz
No. 2	98 mA	−1.2 V	69.6 GHz	164 kHz
No. 3	128 mA	−0.6 V	71.8 GHz	118 kHz
No. 4	145 mA	−1.9 V	73.6 GHz	210 kHz

In summary, the 4PS structure allows for the implementation of a chirped grating by modulating the sampling period on the micron scale while still maintaining a relatively high grating coupling coefficient. The chirped grating helps to mitigate mode competition within the laser cavity, enabling the device to generate two stable longitudinal modes. By adjusting the chirp rates in the design, different wavelength spacings between the modes can be achieved.

The resulting RF signals range from 66.8 GHz to 73.6 GHz, with linewidths measured between 118 kHz and 210 kHz. These experimental results highlight the potential of this device as a compact, highly integrated millimetre-wave source, suitable for various applications requiring stable and continuous millimetre-wave signals.

4.3 Sidewall grating with lateral modulation of the grating coupling coefficient

The test results of the lateral modulation of the grating coupling coefficient structure are presented in this subsection. Considering that previous simulation results indicated that the wavelength spacing in this structure is related to both the DFB cavity length and the fundamental grating coupling coefficient, the results for an array of eight devices are presented here. These devices consist of four different fundamental coupling coefficients and two different cavity lengths, providing a comprehensive comparison of the effects on wavelength spacing.

The epitaxial structure of the laser is the same as that described in Section 2.5. The isolation grooves with a depth of 250 nm were first etched by ICP, providing electrical isolation between the DFB, EAM and curved waveguide sections. In this case, the curved

waveguides at both the front and rear facets are designed to reduce facet reflections, thereby weakening the FP mode strength. Additionally, the curved waveguide at the front facet can also function as a semiconductor optical amplifier (SOA). Then, the first-order gratings with a period of 244 nm and the 2.5-μm-wide ridge waveguide with a height of 1.92 μm were defined by EBL with a resolution of 0.5 nm using HSQ resist in a single step. After developing, the resist patterns were transferred to the sample by ICP using Cl_2-CH_4-H_2-Ar etch gases. After the deposition of a further SiO_2 layer, a 1.5-μm-wide contact window was opened on top of the ridge waveguide, and p- and n-metal contacts were deposited on both the top highly doped InGaAs contact layer and substrate sides respectively. As a final step, the sample was cleaved into individual laser bars with two facets uncoated.

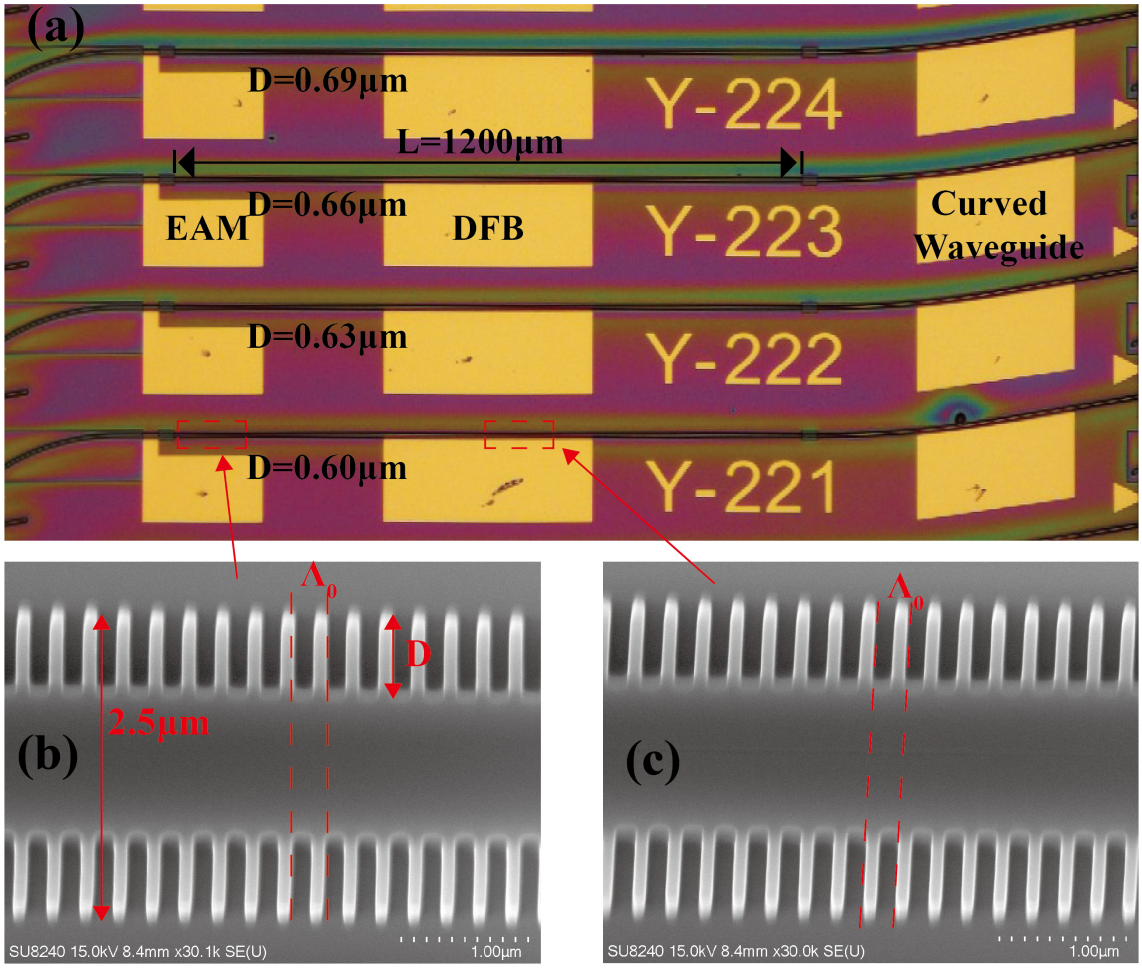

Fig. 4.9. (a) Microscope image of the dual-wavelength DFB laser array with *L*=1200 μm, (b) SEM image of the grating at the beginning of the DFB cavity, (c) SEM image of the grating at the middle of the DFB cavity.

A microscope image of the dual-wavelength DFB laser array with *L*=1200 μm is shown in Fig. 4.9 (a). Each device comprises an EAM section (30-μm-long), a DFB section, and two curved waveguides on the rear and front facets with electrical isolation grooves (30-μm-long) between them. The tilts of the curved waveguides at the front and rear facets are 10°

and 30° and their radius are 2000 μm and 800 μm, respectively. The curved waveguides reduce the facet reflection, therefore the FP modes are greatly suppressed. The SEM images of the HSQ mask patterns at the beginning and the center of the cavity of the DFB section are shown in Fig. 4.9 (b) and (c) respectively. At the beginning of the grating, i.e., $l = 0$, the gratings on both sidewalls are aligned. At the middle of the grating, $l = \Lambda_0/2$ and the gratings on the sidewalls are antisymmetric.

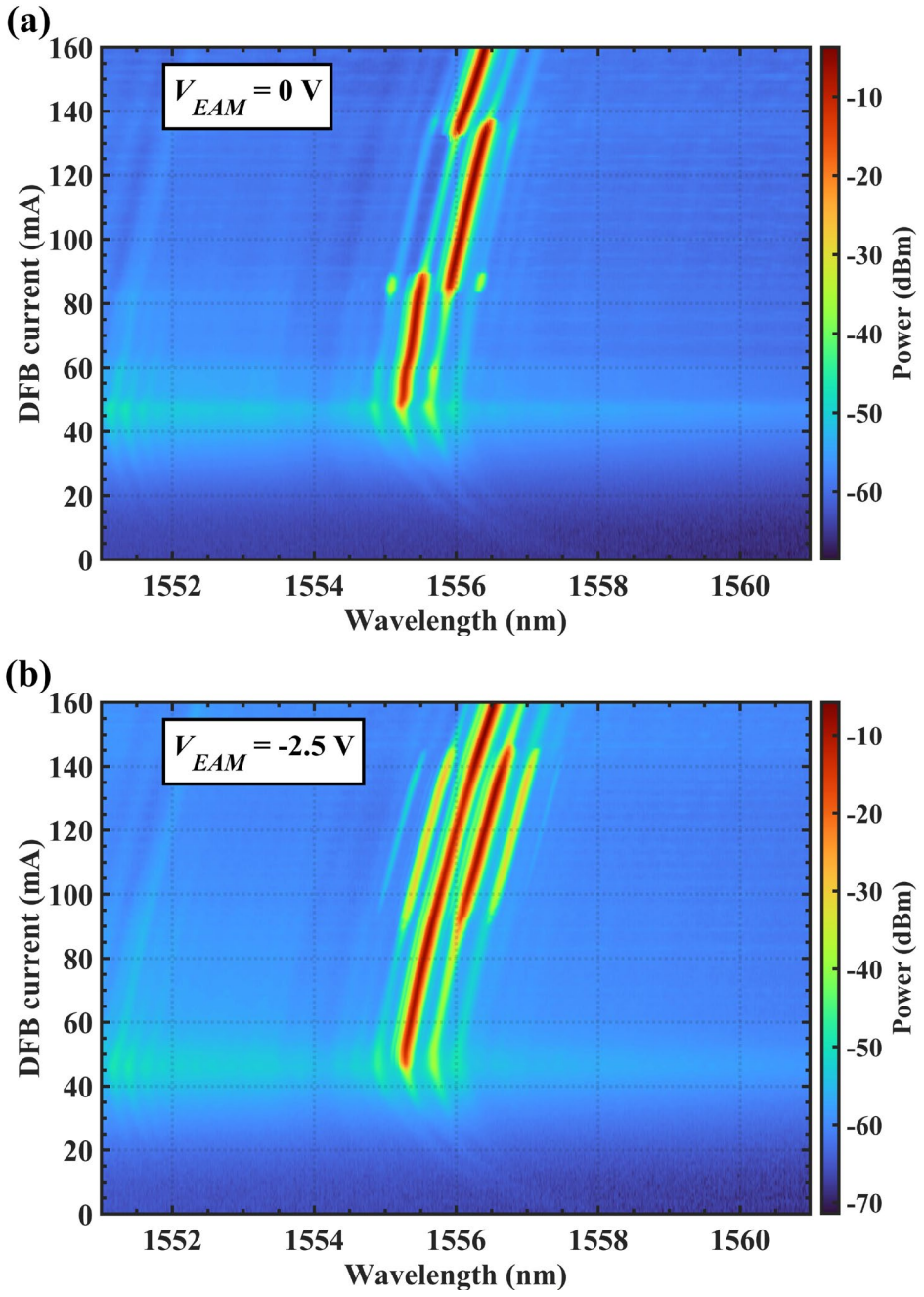

Fig. 4.10. 2-D optical spectrum map of a laser with L = 1200 μm, D=0.6 μm when the EAM reverse voltage is set to 0 V (a), and –2.5 V (b).

During testing, the chip was placed directly on a grounded heatsink, with the TEC temperature set to 20°C. The optical outputs were measured from the front facet with the

injection current in the front curved waveguide was maintained at 30 mA to reduce material absorption. It is important to note that the injection current into the front curved waveguide can alter the overall gain spectrum of the device, which in turn affects the laser's output state. Therefore, during testing, the injection current to the front curved waveguide was kept constant. The optical spectra of a device with $D = 0.6$ μm and $L = 1200$ μm when the DFB injection current (I_{DFB}) changes from 0 mA to 160 mA are shown in Fig. 4.10.

In Fig. 4.10 (a), it can be seen that good dual wavelength operation occurs only over the limited DFB current range 84 mA – 89 mA when V_{EAM}=0 V. This is because there is severe competition between the two modes λ_1 and λ_2. When one of the modes has a higher gain, the other mode is easily suppressed. The integrated EAM has different absorption coefficients for different wavelengths and the absorption edge will be redshifted with V_{EAM}. Once a suitable V_{EAM} is applied to the EAM, λ_1 and λ_2 will be absorbed to different degrees, thus establishing a new equilibrium state where both λ_1 and λ_2 experience the same gain and therefore emit approximately the same optical power. In addition, the EAM section enhances the coupling between the two lasing modes, improves phase locking and stabilizes the mode beating frequency through the mechanism of nondegenerate FWM based on the carrier-density pulsation and spectral-hole burning effects [74]. As shown in Fig. 4.10 (b), the device operates in a good dual wavelength lasing condition for DFB currents from 93 mA to 145 mA with –2.5 V applied to the EAM. The current range for the dual wavelength operation condition is significantly improved compared with that for V_{EAM}=0 V.

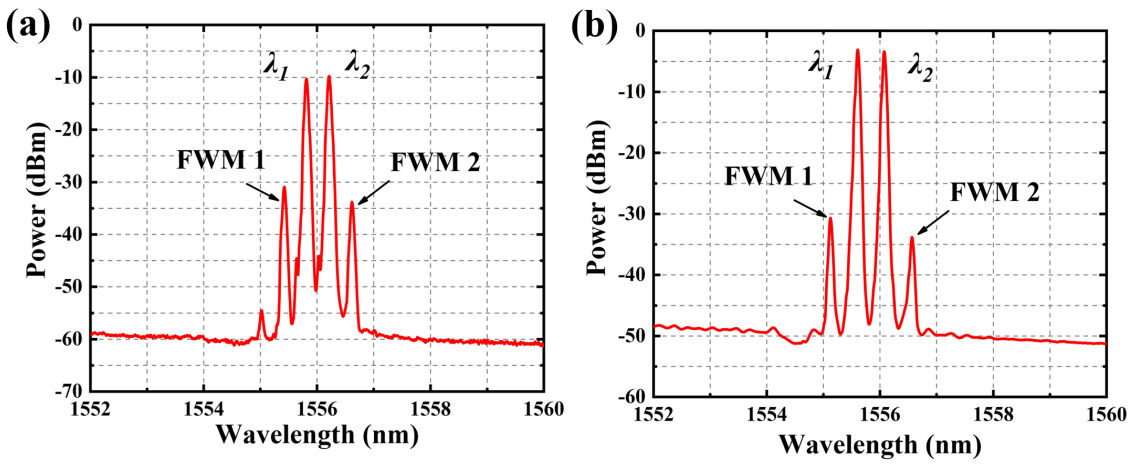

Fig. 4.11. The spectra of the devices with DFB cavity lengths of (a) 1200 μm operating at I_{DFB}=105 mA, V_{EAM}=-2.5V, and (b) 1000 μm, I_{DFB}=112 mA, V_{EAM}=-1.1V, with a fixed D=0.6 μm.

Fig 4.11 shows the spectra of two devices with cavity lengths of (a) 1200 μm and (b) 1000 μm (D=0.6 μm) during dual-wavelength output states. It can be observed that the

device with a shorter cavity length has a larger Δλ. The specific parameters are provided in Table 4.3.

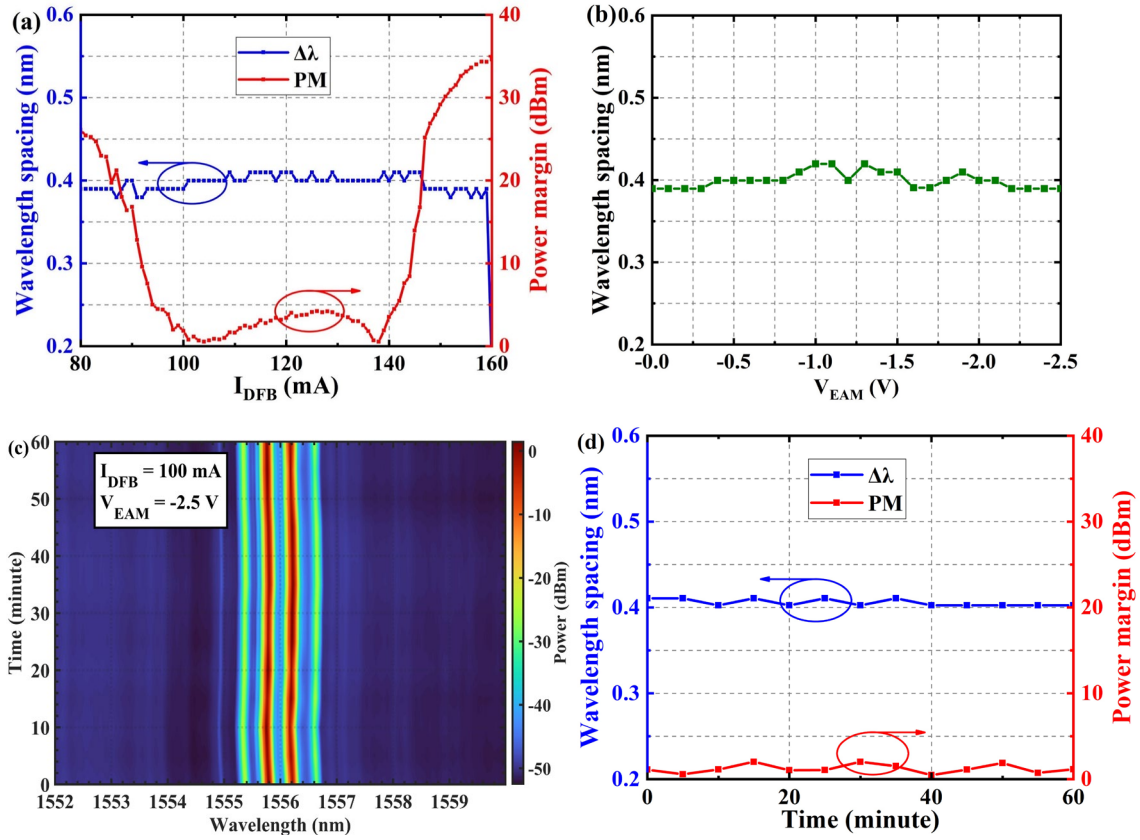

Fig. 4.12. (a) $\Delta\lambda$ and power margin between λ_1 and λ_2 versus I_{DFB} when V_{EAM} is –2.5 V. (b) $\Delta\lambda$ versus V_{EAM}. (c) One-hour 2-D spectral scan of a laser at time intervals of 5 min when L = 1200 μm, D=0.6 μm. (d) Δλ and power margin between λ_1 and λ_2 versus time.

The characteristics of the device with a cavity length of 1200 μm and D=0.6μm under different injection currents are shown in Fig 4.12. As shown in Fig. 4.12 (a), $\Delta\lambda$ remains equal to 0.4 nm with fluctuations within the OSA RBW when I_{DFB} is increased from 80 mA to 160 mA. The PM is at a low level when I_{DFB} is increased from 100 mA to 150 mA, and overall is less than 4 dBm over this range. The minimum PM is 0.4 dBm when I_{DFB} is 104 mA. The $\Delta\lambda$ under different V_{EAM} is shown in Fig. 4.12 (b). During the measurement, $\Delta\lambda$ was recorded when the PM reached its lowest value for each value of V_{EAM}. The fluctuations in $\Delta\lambda$ are also within the OSA RBW. A continuous scanning spectrum of the device over a period of 1 hour at 5 min intervals is shown in Fig. 4.12 (c). The small drift of λ_1 and λ_2 is caused by the noise of the DC sources driving the DFB laser and the front curved waveguide, and of the voltage source driving the EAM, and environmental influences such as temperature fluctuations and mechanical vibration. Temperature fluctuations inside the device would be suppressed after the device is packaged. In Fig. 4.12 (d), during the 1-hour

measurement, $\Delta\lambda$ remains 0.4 nm with fluctuations within the OSA RBW and the PM remains less than 2.1 dB.

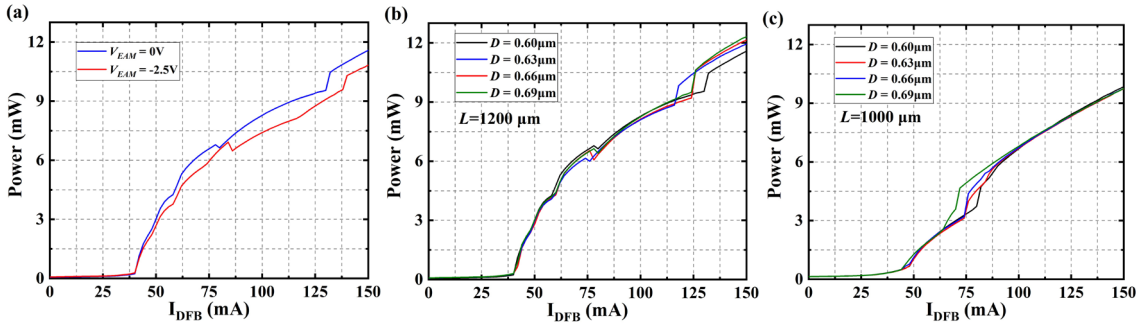

Fig. 4.13. Measured *P-I* curves for (a) *L*=1200 μm, *D*=0.6 μm, (b) a laser array with different *D* values when *L*=1200 μm, V_{EAM}=0 V, (c) a laser array with different *D* values when *L*=1000 μm, V_{EAM}=0 V.

Fig. 4.13 shows the measured *P-I* characteristics from the front facets of the devices with a I_{DFB} scanning step of 2 mA and the injection current in the front curved waveguide kept at 30 mA. As shown in Fig.4.13 (a), the device with *L*=1200 μm has a threshold current of 40 mA. When $V_{EAM}$is 0 V, there are two discontinuities at 80 mA and 128 mA, which arise because the main lasing mode jumps between λ_1 and λ_2. The discontinuities are consistent with the results shown in Fig. 4.10 (a). Similarly, when –2.5 V is applied to the EAM, the two discontinuities occur at 86 mA and 144 mA, respectively. When V_{EAM} is increased from 0 V to −2.5 V, the threshold current is unchanged, but the slope efficiency is reduced slightly due to the increased absorption in the EAM. The slope efficiencies are 0.103 W/A and 0.096 W/A when V_{EAM} is 0 V and −2.5 V, respectively. As shown in Fig. 4.13 (b) and (c), a decrease in κL results in an increase in the threshold current to 48 mA when *L* is reduced from 1200 μm to 1000 μm [156]. Compared to *L*=1200 μm, there is a lower slope efficiency of 0.09 W/A when *L*=1000 μm.

By properly adjusting I_{DFB} and V_{EAM}, a series of stable RF signals from different devices were captured by the ESA within a scanning range of 14 GHz and at a resolution of 50 kHz. the 8 RF signals from 8 devices with different *L* and *D* can be observed in Fig. 4.14 (a). The parameters of the RF signals and the operating conditions of the laser arrays are shown in Table 4.3. When *L*=1200 μm, as *D* increases, the frequency of the RF signal *f* increases from 50.04 GHz to 53.71 GHz. As a result of *L* decreasing to 1000 μm, higher values of *f* from 57.11 GHz to 59.73 GHz are observed, behaviour consistent with the earlier simulations. The device (*L*=1200 μm, *D*=0.6 μm) was operated over a period of 1 hour under I_{DFB} =105 mA and V_{EAM}=-2.5 V, and the recorded frequency and RF intensity as a function of time (recorded at 5 min intervals) are shown in Fig. 4.14 (b), (c). During the one hour

measurement, the RF frequency was 50.04 GHz with a drift of less than 25 MHz. Meanwhile, the RF intensity exhibited a variation of less than 5.5 dBm. The frequency drift is caused by temperature fluctuations inside the device and the intensity variation is due to changes of the PM. This phenomenon would be suppressed by packaging the device.

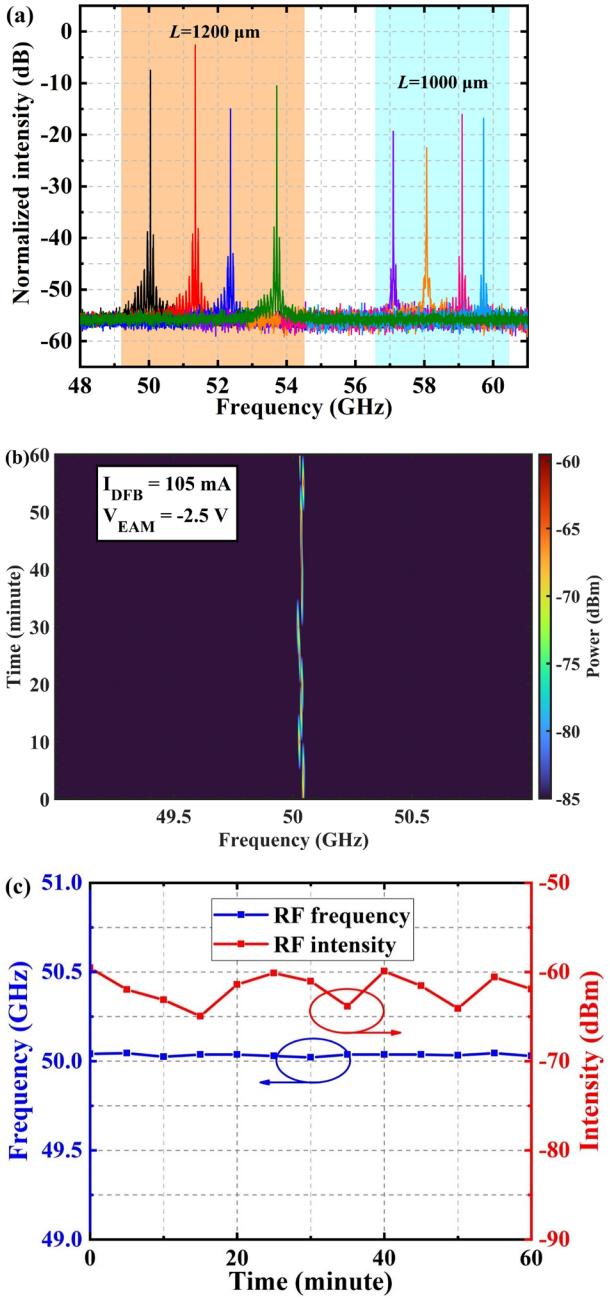

Fig. 4.14. (a) Measured RF spectrum from laser arrays with different *D* values for *L*=1200 μm and 1000 μm, respectively. (b) RF spectral scan over 1 hour at intervals of 5 min for a device with *L*=1200 μm, *D*=0.6 μm. (c) RF frequency and intensity versus time.

Table 4.3 Parameters of the array and RF signal frequencies

L (μm)	D (μm)	I_{DFB} (mA)	V_{EAM} (V)	f (GHz)	$SMSR$ (dB)
1200	0.60	105	–2.5	50.04	31.3
	0.63	100	–2.1	51.35	35.5
	0.66	103	–2.3	52.37	28.0
	0.69	102	–2.3	53.71	27.3
1000	0.60	112	–1.1	57.11	25.9
	0.63	109	–0.9	58.07	25.3
	0.66	120	–1.4	59.14	27.3
	0.69	118	–1.5	59.73	30.4

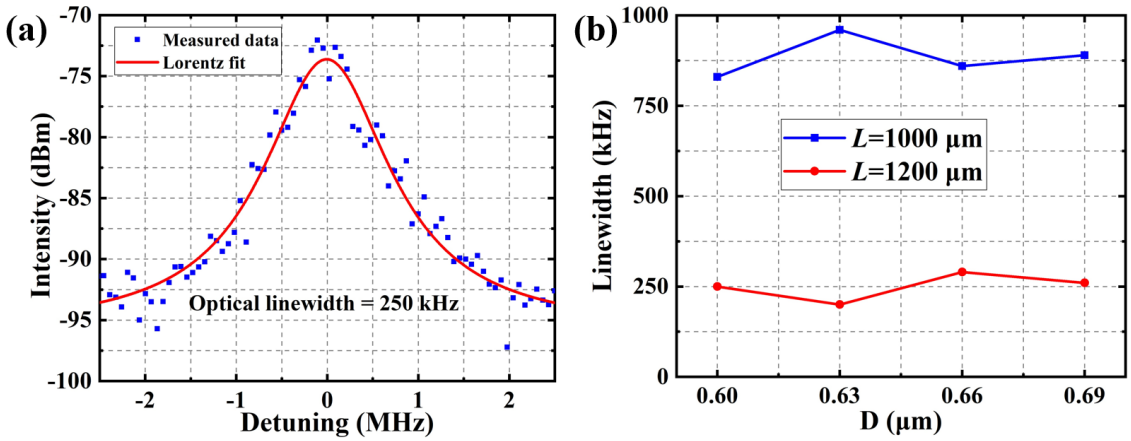

Fig. 4.15. (a) RF spectrum of DFB laser with L=1200 μm, 100 MHz scanning range and 20 kHz resolution when I_{DFB}=102 mA, V_{EAM}=–2.5 V. (b) Optical linewidths of the array.

Through experiments, it was found that RF signals can be obtained under a range of V_{EAM} in one device. The optical linewidth under different V_{EAM} can be obtained by measuring the –20 dB bandwidth of the RF signal, and the measured results of a device with L=1200 μm, D=0.6 μm are shown in Fig. 4.15 (a). When taking the measurements, the scanning range of the ESA was 200 MHz, and the resolution bandwidth was 20 kHz. After fitting to a Lorentzian profile, the optical linewidth is equal to the value of the –20 dB bandwidth divided by $\sqrt{99}$. As shown in Fig. 4.15 (b), when the L is reduced to 1000 μm, the linewidth of the device increases to around 850 kHz, a change consistent with the description in [160].

It is noted that the dual-wavelength operation of the lasers in this subsection is achieved by utilising the side lobes on both sides of the main reflection stopband. Theoretically, the wavelength difference should be larger than the spacing between the two transmission peaks

within the stopband. However, due to the longer cavity length, which narrows the width of the main reflection stopband, the resulting frequency is lower compared to devices with two π phase shifts.

Additionally, the linewidth of the devices with this structure is larger than that of the two π phase shifts structure devices with a cavity length of 750 μm, which is contrary to the usual trend where longer cavity lengths result in narrower linewidths [160]. This is because the curved waveguide at the front of these devices reduces the facet feedback strength, thereby suppressing the linewidth narrowing effect caused by self-injection [161, 162].

4.4 Superimposed sampled Bragg grating based on sidewall grating

Due to the structural characteristics, both types of devices introduced earlier operate below 100 GHz. In this section, the array based on superimposed sampled gratings, covering frequencies from 0.1 to 1 THz will be experimentally demonstrated.

In this subsection, the array is divided into two groups. The first group consists of four devices with frequencies ranging from 300 GHz to 1 THz. Due to the lack of high-speed PD for the THz band, the frequencies of this array are characterised using an autocorrelator, and the THz intensity is measured by a thermal radiation detector.

The second group of devices operates in the frequency range of 135-180 GHz. For this array, by redesigning the fabrication process, Ground-Signal-Ground (GSG) electrodes were applied to the EAM region, allowing the frequency information to be directly read from the EAM area using a high-speed GSG probe and a mixer. Due to the rapid attenuation of the signal strength as the frequency increases, signals above 150 GHz were obscured by noise, but frequencies of 135 GHz and 150 GHz were successfully detected. This method is being proposed and applied to dual-wavelength laser chips for the first time.

4.4.1 An array with a beat frequency ranging from 300 GHz to 1 THz.

Based on the principles described in Section 2.3.3, we designed and fabricated a DWL array with a frequency range of 300 GHz to 1 THz. The grating parameters for this array are shown

in Table 4.4. A schematic of the fabricated DWL using C-SBG technology is illustrated in Fig. 4.16(a).

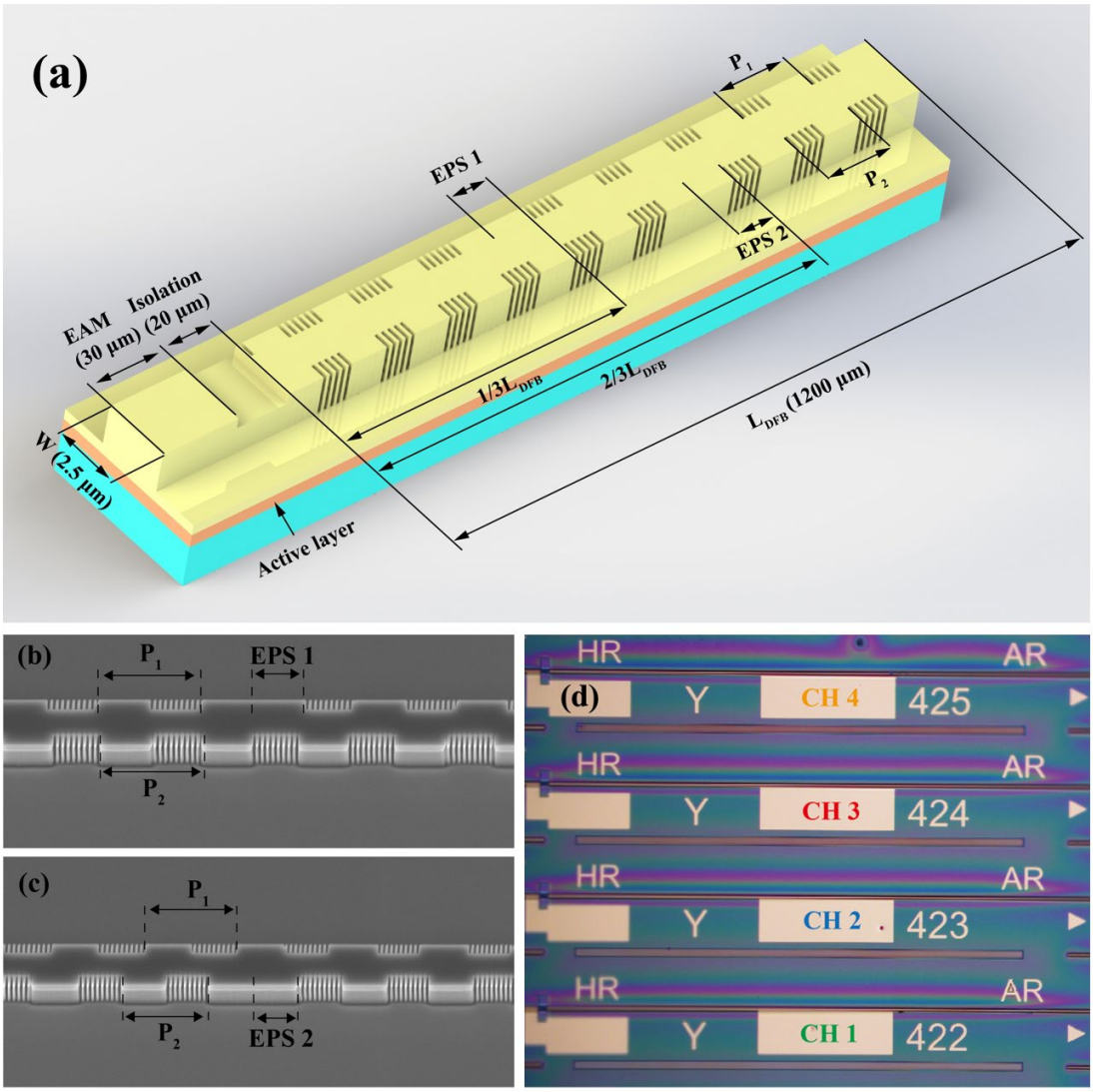

Fig. 4.16. (a) Schematic of the proposed DWL based on C-SBG, and SEM images of EPS 1 (b) and EPS 2 (c), (d) microscope image of the DWL array.

Each device comprises an EAM section (L_{EAM}=30 μm) located at the left facet, and a DFB laser on the right (L_{DFB}=1200 μm), separated by a 20 μm long electrical isolation groove. The 2.5 μm wide ridge waveguide (W=2.5 μm) and grating pattern are defined by EBL with a resolution of 0.5 nm using HSQ resist in a single step. Both sidewalls have the same uniform seed grating with a period of 257 nm and 0.6 μm recess depth; the two lasing wavelengths are then determined by the sidewall grating sampling periods P_1 and P_2. Two EPSs are inserted at 1/3 L_{DFB} on the upper and 2/3 L_{DFB} on the lower sidewall respectively, to ensure both sides operate in SLMs. It should be noted that, as photons tend to concentrate

around the phase shift sections, separating the two EPS sections will lead to the dispersion of peaks in the photon distributions of the two wavelengths, thereby mitigating mode competition. Figs. 4.16 (b) and 4.16 (c) depict SEM images of EPS1 and EPS2, respectively. Fig. 4.16 (d) displays microscope images of the DWL array with varying separation frequencies (300 GHz-1THz). It is noted that, although the HR (High Reflectivity) and AR (Anti-Reflective) coated facets were pre-marked on the chip, during actual testing, both facets remained in their cleaved, uncoated state. The output power and phase of the two longitudinal modes could be adjusted by varying the V_{EAM}, allowing the device to operate in dual-wavelength output conditions. Here, we note that all results are measured from the DFB side. The threshold current is approximately 38-40 mA, and the output power is around 13.4-13.9 mW with I_{DFB} at 200 mA and V_{EAM} at 0 V.

Table 4.4 Grating parameters of the 300 GHz - 1 THz array

Device No.	Λ_0	P_1	P_2	Designed beat frequency
CH1	257 nm	4.611 μm	4.766 μm	300 GHz
CH2			4.847 μm	450 GHz
CH3			4.931 μm	600 GHz
CH4			5.170 μm	1 THz

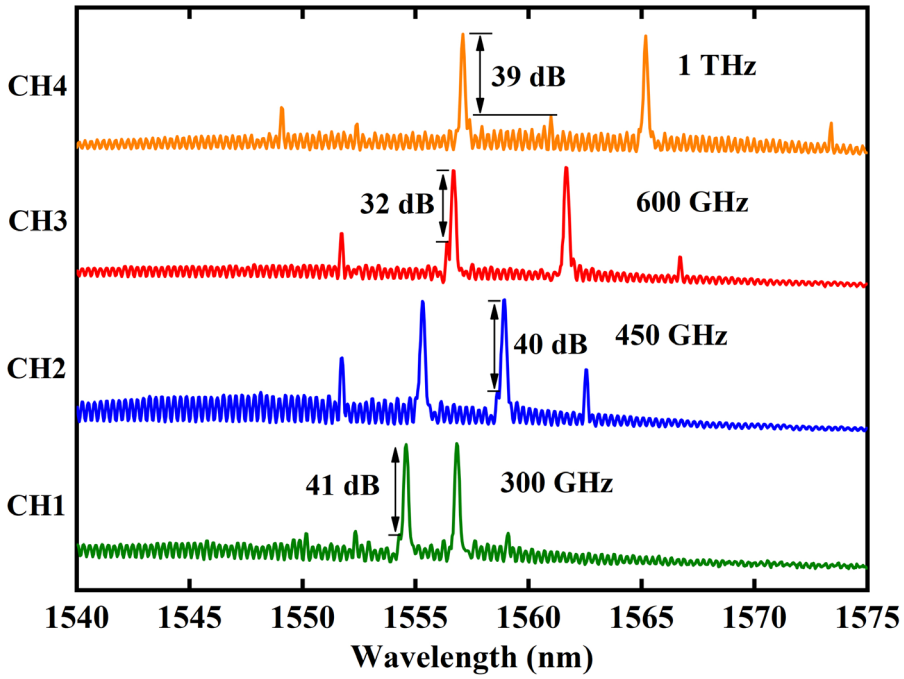

Fig. 4.17. Measured optical spectra of 300 GHz – 1 THz array.

Fig. 4.17 shows the measured optical spectra of the devices. Each device exhibits dual-wavelength lasing with relatively uniform intensities and strong FWM signals for appropriate values of I_{DFB} and V_{EAM}. The frequency spacings between the two lasing modes are designed to be 300 GHz, 450 GHz, 600 GHz, and 1 THz.

Here, due to the lack of high-frequency photodetectors in the laboratory, an autocorrelator (Femtochrome Research Inc, FR-103XL) is used to characterise the time-domain output during the experiments. An autocorrelator is an instrument used to measure the pulse width of ultrashort laser pulses. It is based on autocorrelation techniques, utilizing the pulse itself to measure its temporal characteristics, making it particularly suitable for picosecond and femtosecond pulse measurements. The autocorrelator first splits a laser pulse into two beams of equal intensity. This is typically done with a beam splitter, dividing the incident ultrashort laser pulse into two paths: one as a reference pulse, and the other for introducing a time delay. One of the pulse beams passes through a delay line, where the optical path is adjusted by precisely moving a mirror to introduce different time delays. The two pulse beams will later be recombined with different delays. After passing through the delay line, the two beams are directed to a nonlinear crystal (such as a second-harmonic generation (SHG) crystal). In this crystal, the two pulses interact to produce a second-harmonic signal. The intensity of the second-harmonic signal depends on the temporal overlap of the two pulses. Specifically, when the two pulses fully overlap, the second-harmonic signal is strongest; when there is a delay between them, the second-harmonic signal weakens. The second-harmonic intensity is detected by a photomultiplier tube, and the changes in signal strength are recorded as a function of the time delay. This intensity versus delay function forms the autocorrelation curve, providing insight into the pulse width and temporal characteristics. By analysing the autocorrelation curve, it is possible to determine the duration of the target pulse and gain insights into its time-domain behaviour.

During testing, the laser output was directly coupled into the autocorrelator via an optical fibre. The measured autocorrelation (AC) traces shown in Fig.4.19 indicate that the devices produce sinusoidal outputs. The reciprocal of the average periods of the AC traces corresponds to the optical frequency separation shown in Fig. 4.18. The frequency information obtained from the Fourier transform of the AC traces is shown in Table 4.5. Compared to the designed values, the measured frequency deviation is <15 GHz, primarily due to the constrained autocorrelator resolution and fabrication errors. Details of the measurement conditions and results are shown in Table 4.5. Every device demonstrates stable dual-wavelength operation within an I_{DFB} range of 140 mA to 250 mA.

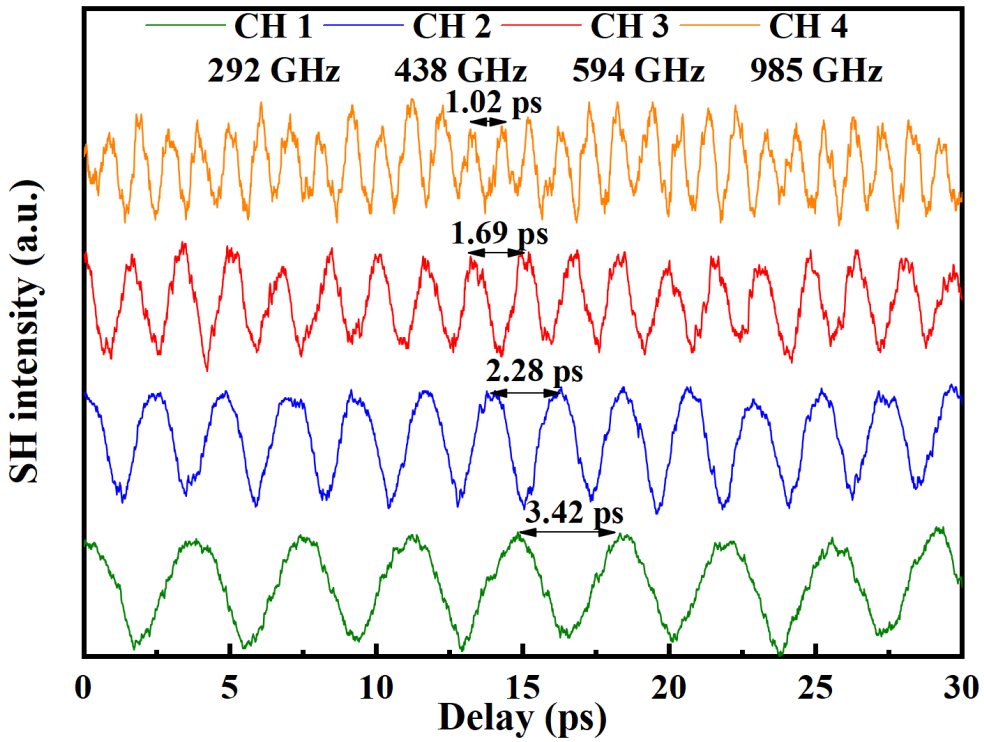

Fig. 4.18. Measured AC traces of 300 GHz – 1 THz array.

Table 4.5 Devices measured condition and results

Device	I_{DFB}	V_{EAM}	AC period	Frequency
CH 1	168 mA	-1.4 V	3.42 ps	292 GHz
CH 2	156 mA	-0.6 V	2.28 ps	438 GHz
CH 3	180 mA	-3.2 V	1.69 ps	594 GHz
CH 4	196 mA	-1.1 V	1.02 ps	985 GHz

To characterise the generated THz power, the dual-wavelength optical signal is amplified and then input into a photoconductive antenna (PCA), which converts the signal into THz radiation. The THz power is subsequently recorded by a thermal radiation detector (Golay detector) [163].

Fig 4.19 shows the experimental setup. Considering the low THz radiation conversion efficiency of the photoconductive antenna (PCA), the optical signal is first coupled out through a lensed fibre and amplified to 20 mW using an EDFA. The amplified signal is then focused onto the PCA's active region through another lensed fibre. After the PCA converts the dual-wavelength signal into THz radiation, the THz beam first passes through an optical chopper, fixed at 20 Hz, before being collected and measured by a Golay detector. Since some of the 1550 nm light can pass through the PCA and cause a response in the Golay

detector, an A4 sheet of paper is placed between the detector and the chopper to block the optical signal. The purpose of the chopper is to sample the THz signal, allowing the system to distinguish between environmental noise and the signal to be detected.

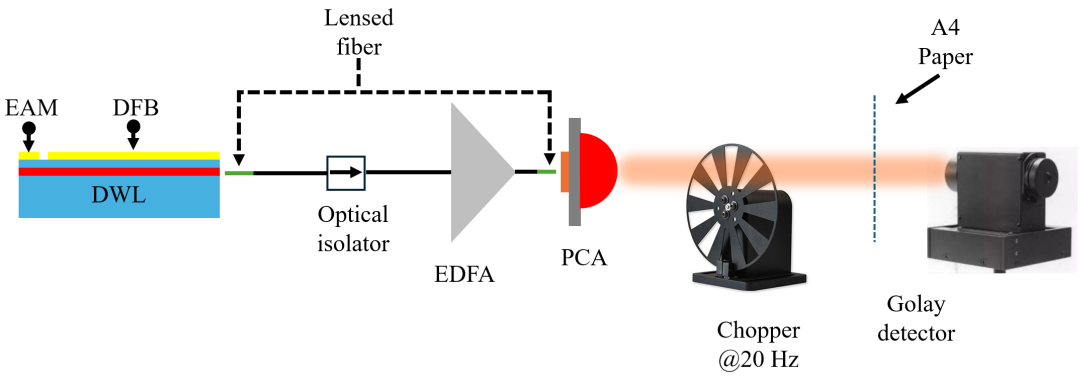

Fig. 4.19. Schematic of THz detection.

In this setup, the PCA used is the PCA-180-05-10-1550-h from BATOP, which has an absorption rate of 25% for light in the 1550 nm wavelength band. The light absorption area is a rectangular window measuring 5 μm × 10 μm. The lensed fibre can focus the light spot to a 2.5 μm radius at a 10 μm focal distance, therefore, in this setup, it is assumed that the entire light beam is incident on the PCA's active region. Considering that the PCA's THz radiation has a half-divergence angle of 15 degrees and the Golay detector has an aperture diameter of 11 mm, when the distance between the Golay detector and the PCA antenna is 5 cm, the THz radiation beam will have a diameter of 26.8 mm. This means that only about 17% of the THz energy can enter the Golay detector. It is important to note that due to the use of the chopper, the actual signal appears as a 20 Hz waveform in the Golay detector software. When reading the THz signal, only the difference between the peaks and troughs of the waveform is used to determine the THz signal intensity.

Fig 4.20 shows the results of the Golay detector's power output as a function of injection current for four different lasers. The results indicate that once the laser current exceeds the threshold, the detector begins to respond. Additionally, the power of higher-frequency signals is lower, as the PCA's response decreases with increasing frequency. For the four devices operating in the 300 GHz to 1 THz range, the maximum THz power detected was between 27 nW and 73 nW. Considering that only 17% of the power was collected by the detector, the actual emitted THz radiation power ranges from approximately 160 nW to 430 nW. With the optical power limited to a maximum of 20 mW incident on the active area, and considering the PCA's 25% light absorption efficiency, the actual THz radiation conversion

efficiency of the PCA for 1550 nm light is calculated to be around 10^{-5}. This matches the data provided by BATOP.

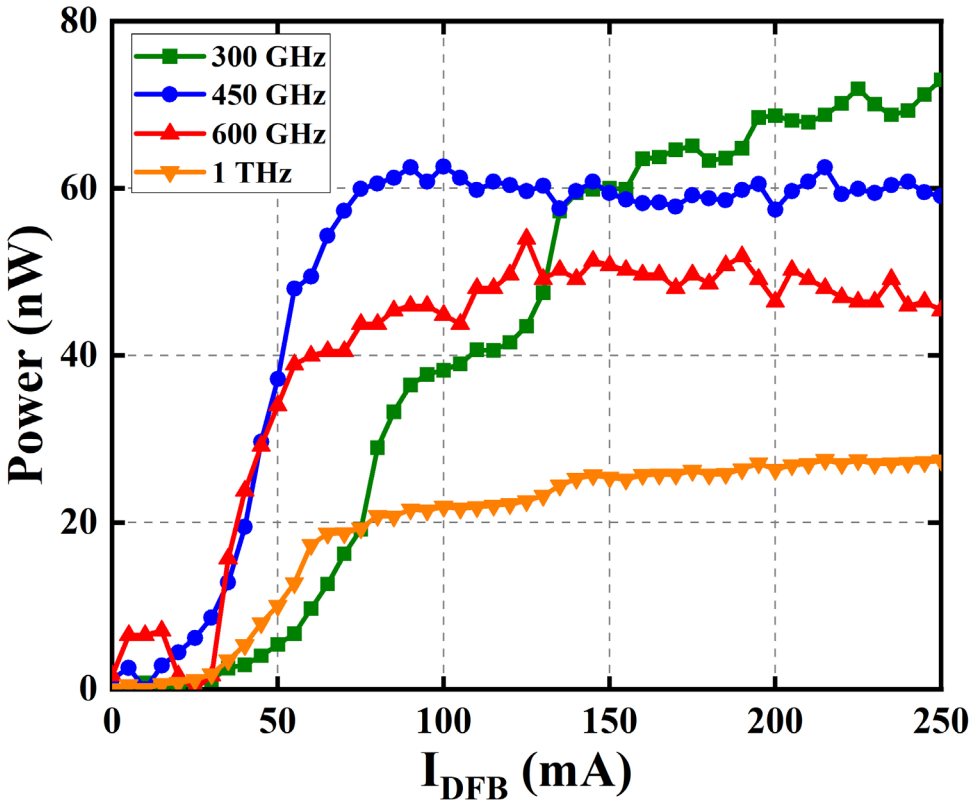

Fig. 4.20. THz radiation power versus injection currents of the array.

4.4.2 An array with a beat frequency ranging from 135 GHz to 180 GHz.

To enable direct reading of the device's frequency information on an ESA, a novel approach is proposed, utilising the EAM section at the laser's end facet to detect the RF signal generated by the device. It's important to note that if the EAM is functioning solely as a phase modulator, theoretically, it can operate under reverse bias, forward bias, or even with current injection. However, only when the EAM is under reverse bias can it act as a photodetector, where the quantum wells in reverse bias serve as a photo-absorptive element [164-166].

Since the overall structure includes a thick p-doped region, the response of the reverse-biased EAM to high-frequency signals will be limited due to the significantly slower drift velocity of holes compared to free electrons. This characteristic would reduce the high-frequency response of the reverse-biased EAM [167-170].

In this approach, the reverse bias for the EAM is applied using a probe along with an integrated Bias-T on the probe. The DC port of the Bias-T is connected to the reverse bias

voltage, while the RF port is directly connected to the mixer and ESA. Based on this, the fabrication process needs to be modified so that the negative electrode, like the positive electrode, is also positioned on the top surface of the laser. This process is accomplished by etching a two-step ridge waveguide (TSRW).

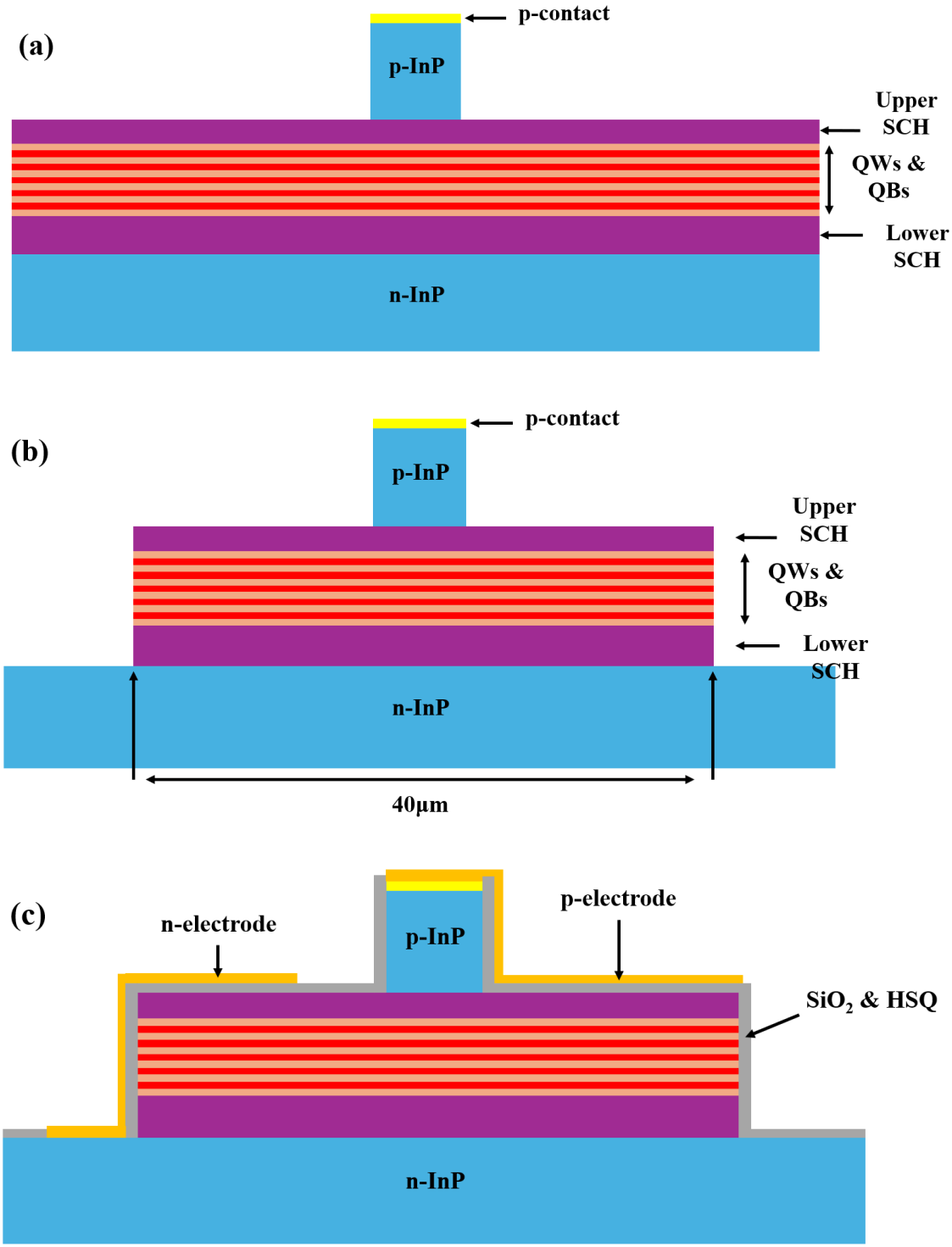

Fig. 4.21. Schematic of the modified device, (a) after etching grating and waveguide, (b) TSRW etching, (c) metal deposition of p- and n- electrode.

As shown in Fig 4.21 (a), the etching of the grating and waveguide, along with the previous steps, is the same as for standard devices. After completing the grating and waveguide etching, HSQ is used as a mask to protect a 40 μm wide area on both sides of the ridge waveguide. A second dry etching step is then performed to etch the unprotected regions down to the n-InP buffer layer as shown in Fig. 4.21 (b). Subsequently, the processes for insulating layer deposition, window opening, and electrode deposition are carried out. During the window-opening step, it is crucial to open the window on the ridge waveguide for the p-electrode and etch part of the n-electrode region as well. The schematic of the electrode deposition is shown in Fig 4.21 (c). Fig 4.22 shows the SEM cross-sectional image of the fabricated device.

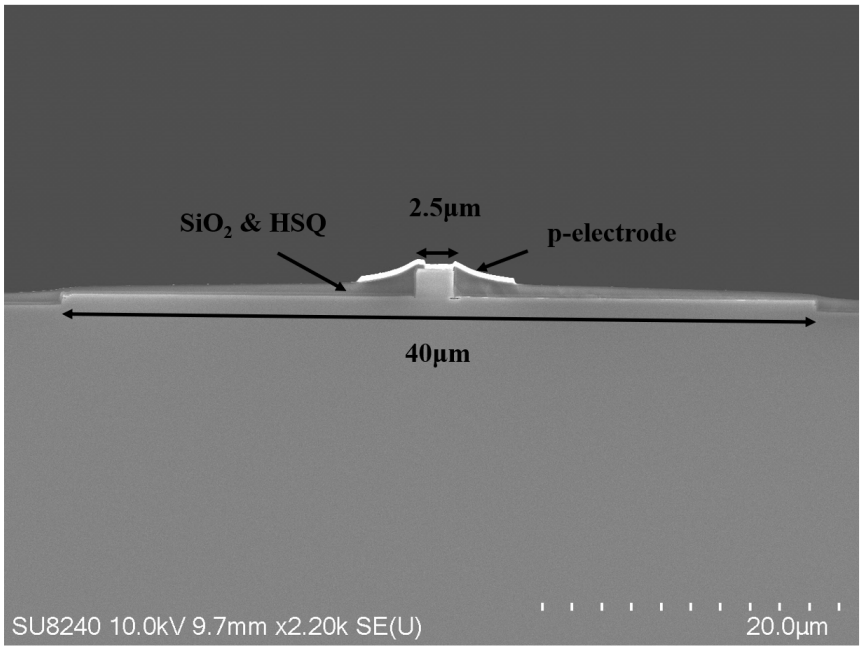

Fig. 4.22. SEM cross-sectional image of the fabricated device.

The second key point is that to directly obtain the RF signal from the EAM section, the wavelength spacing of the device's dual wavelengths must be minimized due to the limited frequency response range of the EAM. In this structure, to prevent the overlap of the two reflection spectra, the grating recess depth is reduced to 0.4 μm, and the DFB cavity length is increased to 2 mm. Additionally, the length of the EAM was increased to 60 μm, while the width of the electrical isolation remained unchanged at 25 μm.

An advantage of reducing the recess depth is that it facilitates the etching of the grating pattern as it will mitigate the RIE lag effect. As shown in Figure 4.23, when the recess depth is reduced to 0.4 μm, the grating exhibits excellent verticality and uniformity, with the grating grooves clearly visible and well-defined.

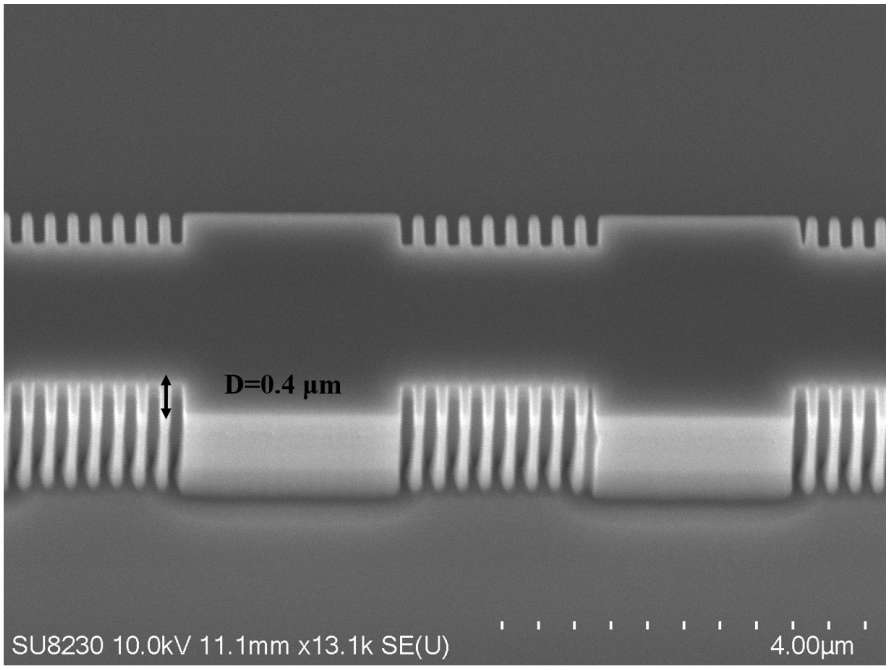

Fig. 4.23. SEM image of the fabricated C-SBG sidewall gratings.

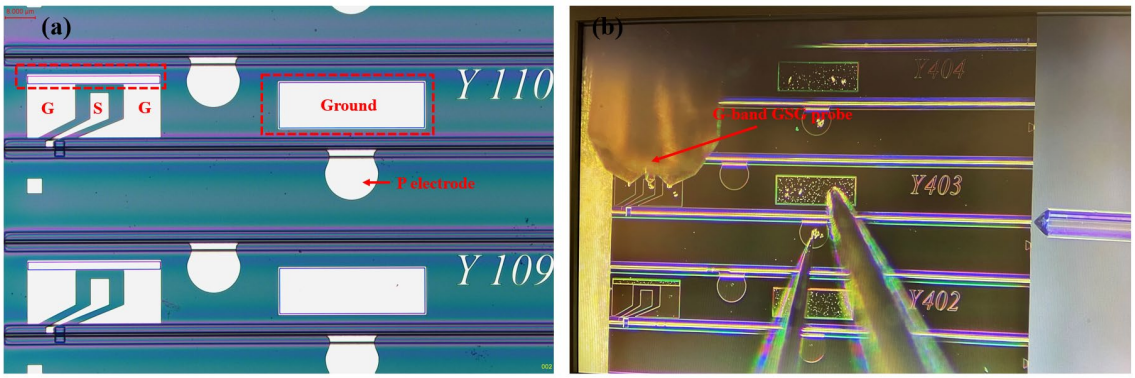

Fig. 4.24. Microscope images of (a) fabricated device electrode, (b) experimental probe set up.

Fig 4.24 (a) shows the fabricated electrodes, with the red dashed boxes highlighting the window-opening areas for the EAM and DFB negative electrodes. The width of the GSG electrode configuration, slot-signal-slot, is the standard 40 µm-60 µm-40 µm, designed to match the probe spacing for the G-band (140-220 GHz) measurements. Fig 4.24 (b) shows a microscope image of the device with the probes connected to the laser.

A laser array covering a frequency range of 135-180 GHz was designed with 5 GHz intervals. Unfortunately, some devices were damaged during fabrication. The spectra and status data of the remaining functional devices are shown in Fig 4.25 and Table 4.6, respectively.

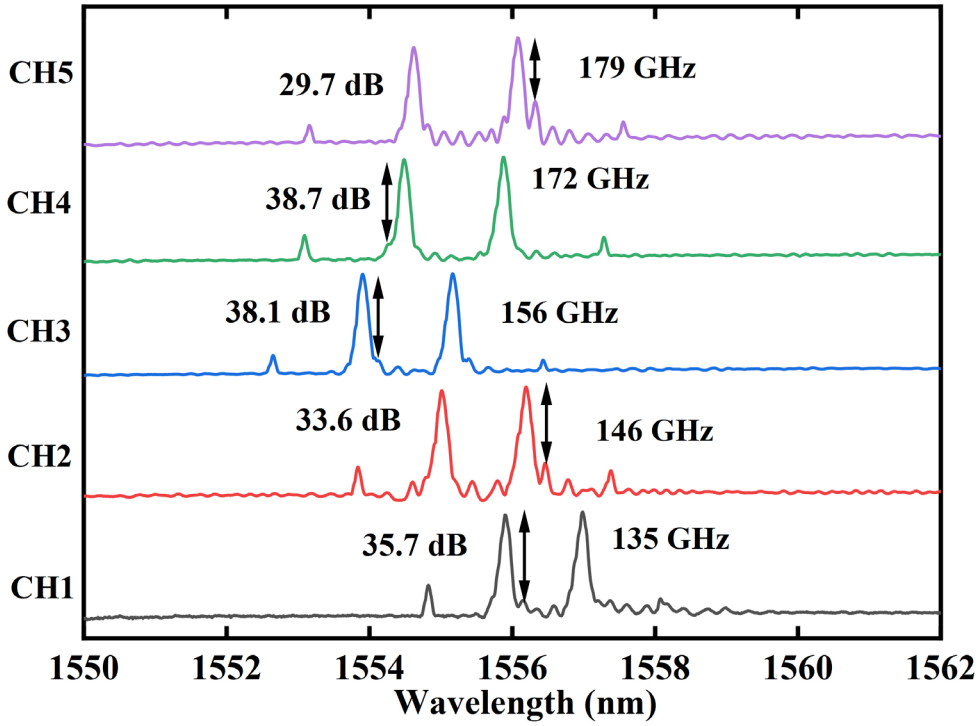

Fig. 4.25. Measured optical spectra of the 135-180 GHz array.

Table 4.6 Designed and measured parameters of 135-180 GHz array.

Device No.	Λ_0 (nm)	P_1 (μm)	P_2 (μm)	I_{DFB} (mA)	V_{EAM} (V)	Designed beat frequency (GHz)	OSA measured beat frequency (GHz)
CH1			4.584	238	-3.0	135	135
CH2			4.590	192	-1.8	145	146
CH3	257	4.513	4.595	162	-1.6	155	156
CH4			4.603	182	-2.0	170	172
CH5			4.609	188	-2.2	180	179

As shown in Fig 4.25, the designed devices achieved good dual-wavelength lasing, with all devices exhibiting an SMSR higher than 29.7 dB. The lasing wavelengths were measured using an OSA, and the corresponding beat frequencies were calculated, as presented in Table 4.6. The maximum discrepancy between the beat frequencies calculated from the OSA data and the designed frequencies was 2 GHz. This may be due to the OSA's limited resolution of 0.06 nm.

The setup for measuring the frequency is relatively simple, as shown in Fig 4.26(a). A constant current source is used to pump the DFB section of the laser, with the optical output from the DFB port connected to an optical isolator and an OSA for monitoring the spectrum. A G-band GSG probe is applied to the EAM section, and the integrated Bias-T on the probe has two ports: a DC port and an RF port. The DC port is connected to a constant voltage source to provide reverse bias to the EAM section. The RF port is first connected to a G-band mixer (M05HWDX, OML) and then to an ESA (Keysight, N9020B).

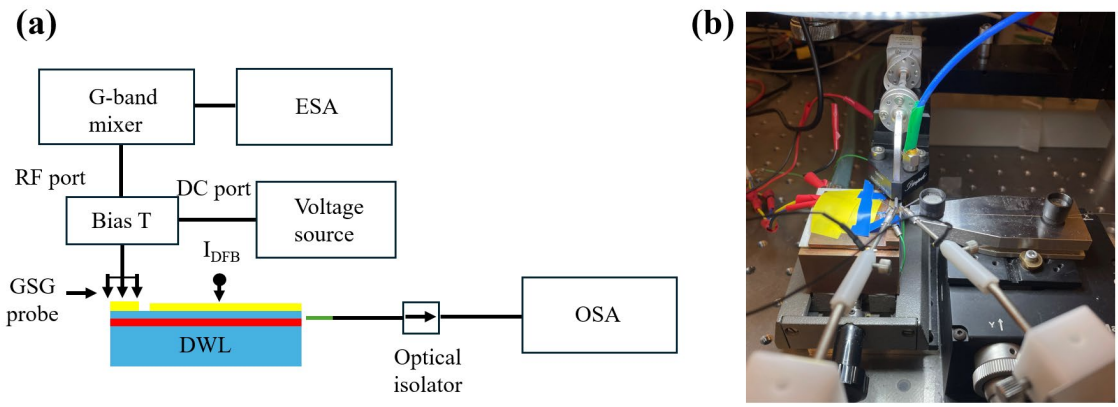

Fig. 4.26. (a) Schematic of the RF frequency measurement setup, (b) photograph of the setup.

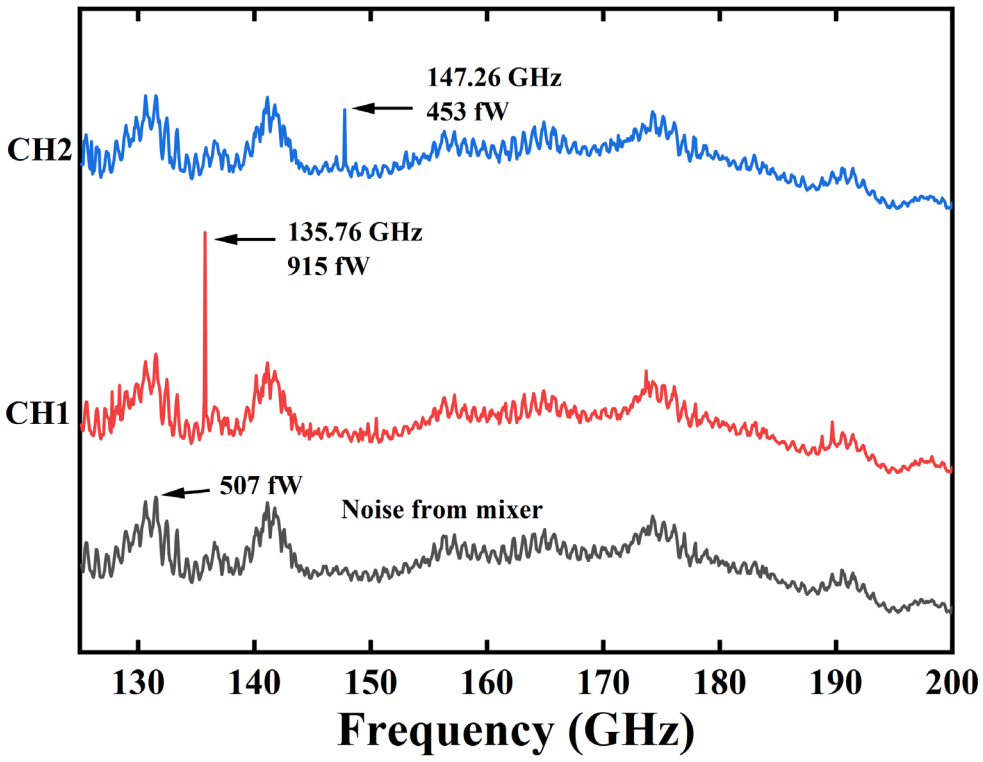

Fig. 4.27. Measured RF frequency spectra.

Due to the limited conversion capability of the EAM at high frequencies, the y-axis was set to a linear scale during testing to enhance data visibility. The measurement results from CH1 and CH2 are presented in Fig. 4.27. During the test, the resolution was configured to 100 kHz, and all data represents the average of 100 samples rather than a single capture.

For better comparison, the noise from the mixer was recorded first with the laser turned off, as shown by the black line in Fig 4.27. The peak noise power was 507 fW. The red curve represents the data measured from CH1 under its optimal operating condition (as indicated in Table 4.6), where the frequency detected in the EAM is 135.76 GHz, which matches both the OSA-calculated value and the design frequency. The peak power in this state was 915 fW. As for CH2, operating at 147.26 GHz, exhibited a peak power of 453 fW. Clearly, as the frequency increases, the EAM's response further decreases, and the peak power for CH2 is actually lower than the highest noise peak. However, since the noise level around 147 GHz is relatively low, the frequency data for CH2 can still be measured. Unfortunately, at higher frequencies, the noise becomes stronger and the EAM's response diminishes further, causing the frequency spectra of other devices to be overwhelmed by the noise, making it impossible to detect their frequencies. Even when considering that only a portion of the THz signal can enter the GSG probe due to impedance matching, the measured signal power in this experiment still shows a difference of several orders of magnitude compared to the signal power generated by the PCA. This is attributed to the inherently low relaxation oscillation frequency of the EAM part, resulting in significant signal attenuation at higher frequencies. Additionally, the lack of impedance matching between the EAM and the GSG probe in this experiment led to a large portion of the signal not being efficiently coupled into the probe.

However, this experiment directly demonstrates the ability of dual-wavelength devices to generate THz signals and directly characterise their frequencies. In the field of THz generation through optical beating, this experiment is the first to propose and demonstrate a method that uses the device itself, without the need for an external PD, to produce THz signals.

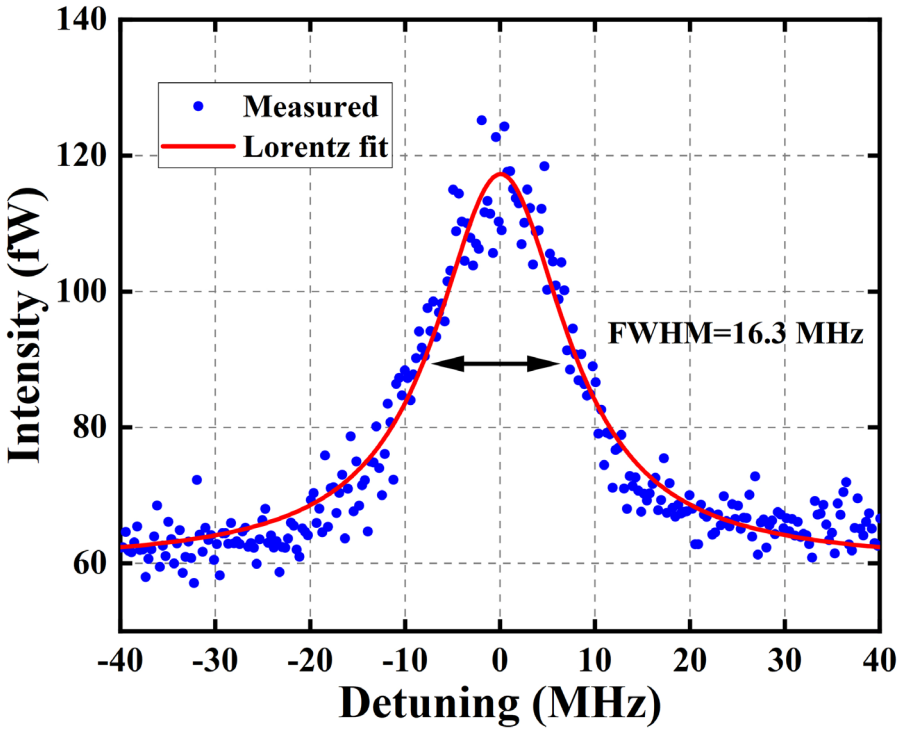

Fig. 4.28. Measured linewidth of CH1.

Fig 4.28 shows the linewidth of the 135 GHz signal generated by CH1. After Lorentzian fitting, the Full Width at Half Maximum (FWHM) of the signal is 16.3 MHz. During testing, the resolution of the ESA was set to 100 kHz, and the data was averaged over 100 scans.

It is noted that this linewidth result is two orders of magnitude larger than the millimetre-wave linewidths presented in the previous sections. Two potential reasons for this are: first, the longer device may experience poor temperature control, causing frequency drift in the signal. Second, the RF signal from the probe may feed back into the EAM region, disrupting the overall gain and refractive index within the cavity, thereby introducing additional noise into the signal [171-173].

4.5 Chapter summary

In this chapter, the test results for three different types of device arrays, fabricated based on the structures introduced in Chapter 2, are presented. The two π phase shifts and lateral coupling coefficient modulation structures were confirmed to be suitable for generating millimetre-wave signals. By controlling parameters such as the chirp rate, cavity length, and fundamental coupling coefficient, the devices were able to produce RF signals at different frequencies, with the linewidths of the millimetre-wave RF signals being less than 1 MHz.

The devices based on the superimposed SBG structure were confirmed to cover the 0.1-1 THz frequency range. The frequency and THz radiation power of the 300 GHz-1 THz array were characterised by an autocorrelator and a Golay detector, respectively. Testing showed that the beat frequencies of the devices matched the designed values, and the THz radiation power generated by the PCA was around several tens of nanowatts. For the 135 GHz-180 GHz array, an innovative approach was used by employing a reverse-biased EAM to detect the beat frequency signals. Signals at 135 GHz and 147 GHz were successfully detected and characterised, marking the first time this method has been proposed and demonstrated.

In summary, the experimental results confirm that the designed dual-wavelength laser arrays are capable of generating signals in both the millimetre-wave and THz bands. In the next chapter, the use of optical injection locking will be introduced to improve the quality of the beat frequency signals, potentially narrowing the linewidth to below 1 Hz.

Chapter 5: Obtaining high-quality RF signals through optical injection locking

From Equation 2.2, If the noise from the PD is ignored, the beat frequency noise is mainly influenced by the time-dependent drift of the lasing wavelengths and the phase fluctuations between the two lasing modes.

Optical injection is a method that can simultaneously lock both the frequency and phase of the injected laser. Theoretically, once injection is complete, the operating frequency and phase of the injected device will be identical to that of the injected signal. In other words, the quality of the beat frequency signal from the injected device can match that of the injection source [174-177].

5.1 Optical injection locking system setup

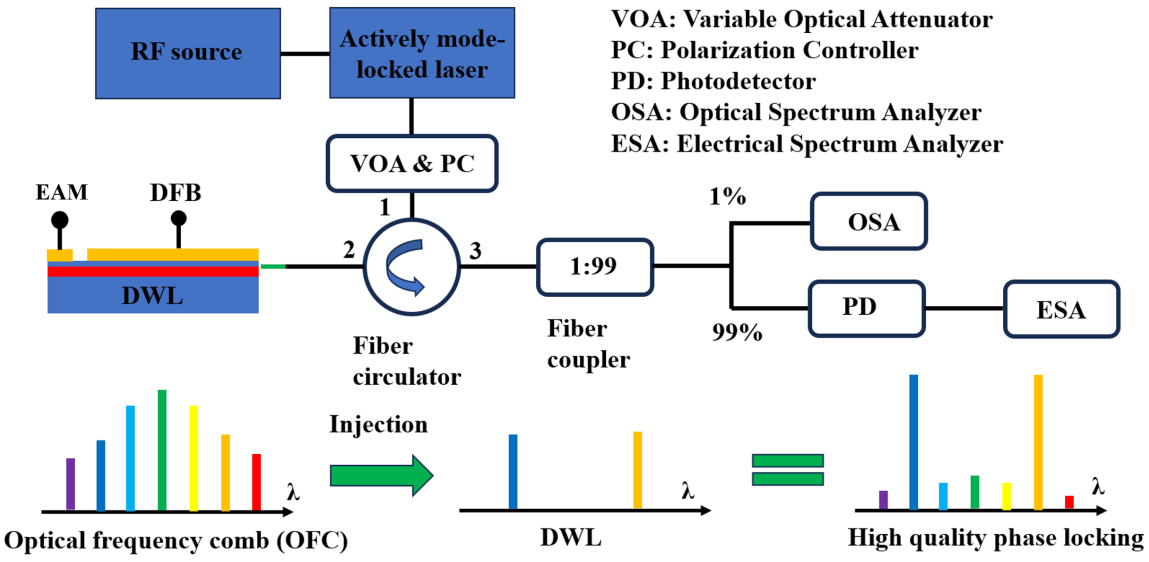

Fig. 5.1. Schematic of injection-locking of the DWL system.

Here, an optical frequency comb (OFC) is used as the injection source to lock the frequency and phase of the fabricated DWL. The OFC is provided by an actively mode-locked fibre laser (UOC series, Pritel Inc). The OFC has a tunable central wavelength range

of 1530-1565 nm, with a frequency tunable from 1 to 20 GHz (with partial continuous tuning in this range). During operation, the OFC requires an external RF source for active locking.

The generated OFC signal passes through a variable optical attenuator (VOA) and a polariser controller (PC) before being injected into the DWL through a fibre circulator from the DFB facet. The VOA and PC are used to control the intensity and polarisation of the injected signal, respectively. Subsequently, the locked optical signal is split into two parts: 1% of the signal is directed to an OSA for spectral observation, while the remaining 99% is sent to a PD connected to an ESA to monitor the frequency information.

To achieve complete injection locking, the first step is to align the two optical wavelengths of the OFC with the output wavelengths of the DWL, minimizing frequency detuning as much as possible. Additionally, the injection power must be controlled so that the noise fluctuations on either side of the frequency signal observed on the ESA are minimised, then the system has reached the injection locking state.

5.2 Ultra-narrow RF linewidth

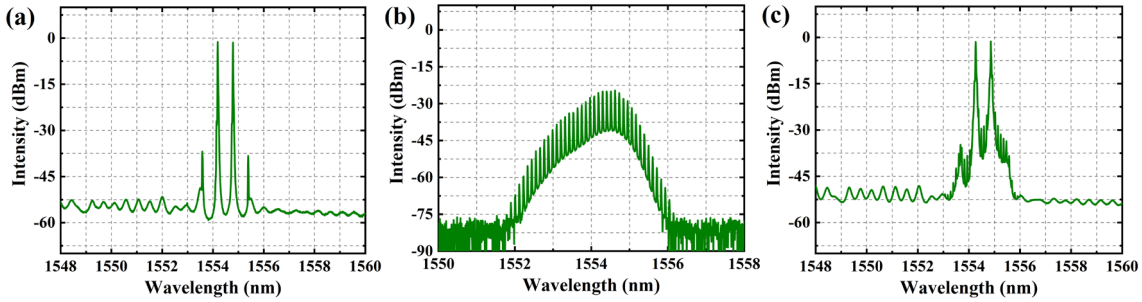

Fig. 5.2. (a) Measured spectrum of the DWL at DFB current of 98 mA and EAM voltage of –1.2 V before injection, (b) measured spectrum of the OFC with frequency spacing of 13.55 GHz, (c) measured DWL spectrum after injection.

First, we perform injection locking on the millimetre-wave device. The selected DWL is based on the two π phase shifts with equivalent chirp structure. Under an injection current of 98 mA and an EAM reverse bias of -1.2 V, the device's beat frequency without injection is 67.75 GHz, and the output spectrum is shown in Fig 5.2(a). First, we attempt to use the fifth sub-harmonic of the OFC for injection, where the frequency spacing of the OFC is set to 13.55 GHz (one-fifth of 67.75 GHz). The optical spectrum of the OFC is shown in Fig 5.2(b). After adjusting the wavelength, power, and polarization to achieve the locked state, the resulting optical spectrum is shown in Fig 5.2(c).

At this point, the optical power of the OFC measured from port 2 of the fibre circulator is 73 μW, and the laser's own output power is 10.8 mW, so that the injection ratio is 0.65%.

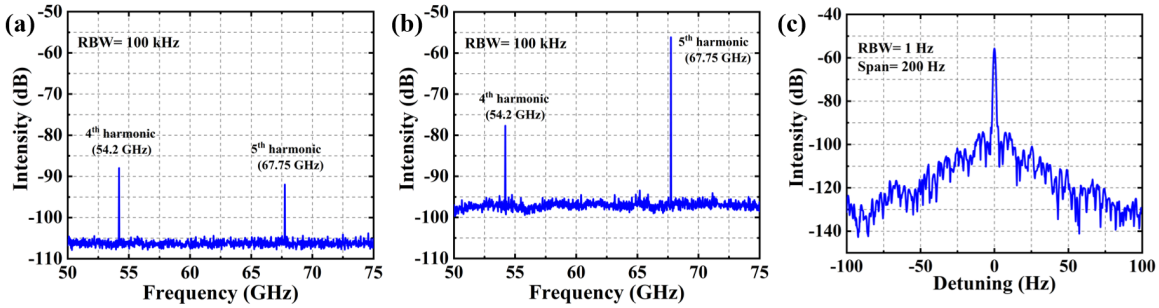

Fig. 5.3. (a) Measured frequency spectrum from the OFC when the frequency interval is 13.55 GHz (5×), (b) measured frequency spectrum after the injection locking, (c) spectrum with 1 Hz RBW and 200 Hz span at center frequency of 67.75 GHz.

As shown in Fig 5.3(a), the fifth sub-harmonic of the OFC aligns exactly with 67.75 GHz. Additionally, as the harmonic order increases, the signal strength decreases. That is, the strength of the fifth harmonic signal is lower than that of the fourth harmonic. In Fig. 5.3(b), as injection locking is completed, the fifth sub-harmonic is significantly amplified, with its strength surpassing that of the fourth harmonic. This suggests that, once injection locking is achieved, the DWL acts as both a filter and an amplifier within the system. At the same time, by setting the ESA's centre frequency to 67.75 GHz, with a span of 200 Hz and an RBW of 1 Hz, it can be observed that the 67.75 GHz RF signal has an extremely narrow linewidth. Given that 1 Hz is the limit of the ESA's resolution, the actual signal linewidth is likely below 1 Hz. It is important to note that, according to the experimental data from Section 4.2, in the free-running state, the beat frequency linewidth of the DWL exceeds 100 kHz. This indicates that the injection locking system significantly reduces the device's beat frequency linewidth.

From the results, it is evident that optical injection into the DWL performs a process of frequency multiplication and amplification of the external RF signal. As shown in Fig 5.3, a 5x frequency multiplication has already been achieved. The next experiment attempts a 30x frequency multiplication through injection.

As shown in Fig. 5.4, the frequency spacing of the OFC is set to 2.255 GHz, with its 30x multiple being 67.65 GHz, resulting in some detuning from the DWL frequency. Despite this, the injection process can still be achieved by increasing the injection ratio. At this point, the OFC output power is 145 μW.

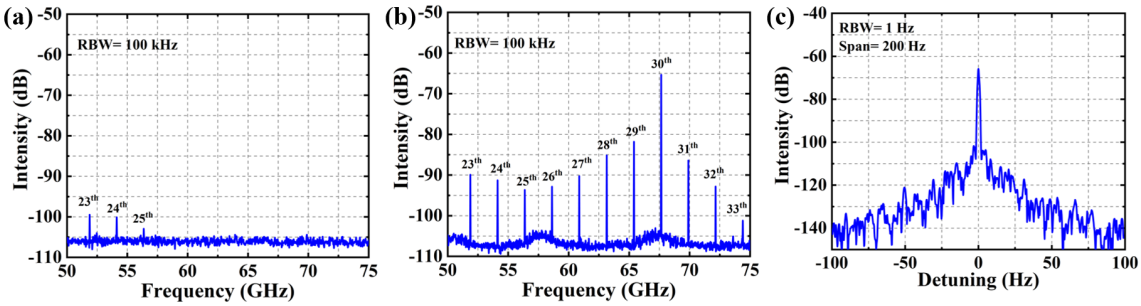

Fig. 5.4. (a) Measured frequency spectrum from the OFC when the frequency interval is 2.255 GHz (30×), (b) measured frequency spectrum after the injection locking, (c) spectrum with 1 Hz RBW and 200 Hz span at center frequency of 67.75 GHz.

Fig. 5.4 (a) shows the frequency spectrum of the OFC itself, where it is noted that the 30x signal (67.65 GHz) is not detectable. After completing the injection locking process, the 30x signal is significantly amplified, as seen in Fig 5.4(b), and its intensity surpasses that of other harmonics. Additionally, it is observed that signals on either side of the 30x harmonic are also amplified. This occurs because the DWL has a certain optical linewidth, allowing neighbouring wavelengths of the OFC to experience some degree of gain as well. Similarly, in Fig 5.4 (c), with the ESA's span set to 200 Hz and the RBW set to 1 Hz, it can be observed that the signal has a 3 dB linewidth of 1 Hz.

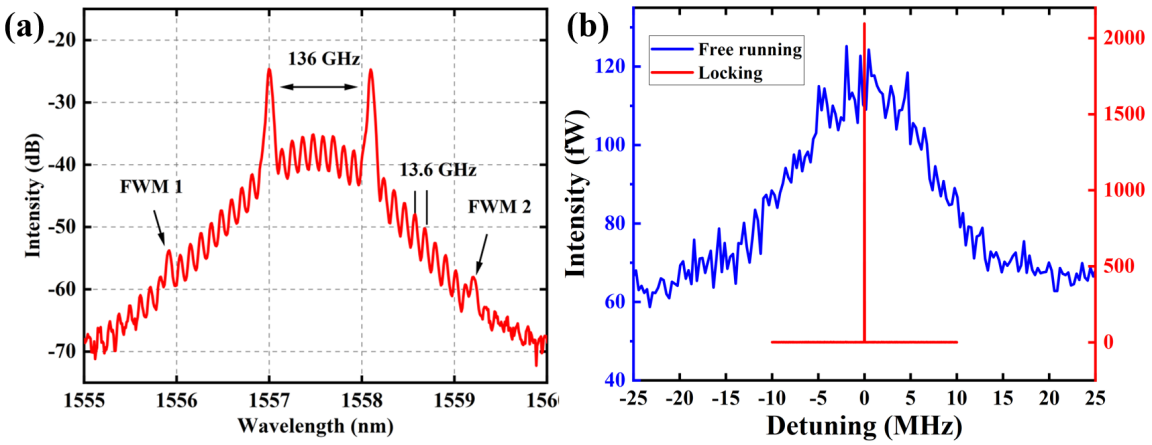

Fig. 5.5. (a) Optical spectrum of the 136 GHz device after injection with OFC frequency interval is 13.6 GHz (10×), (b) Measured 136 GHz signal linewidth with and without locking.

Similarly, a high-quality THz signal can also be obtained by using OFC injection for the 136 GHz device. During the injection process, the OFC frequency spacing is set to 13.6 GHz, which is one-tenth of the target frequency. Fig 5.5(a) shows the spectrum after the injection locking is completed. Notably, two FWM signals also correspond to the wavelengths of the

OFC. At this point, the laser's output power is 6.4 mW, while the OFC's output power is 503 μW. After the injection is completed, the frequency spectral changes are shown in Fig 5.5(b). The data in the injected state were obtained with the ESA set to a span of 20 MHz and an RBW of 1 kHz. It can be observed that after the 136 GHz signal is locked, its peak power significantly increases, reaching 2270 fW, and the linewidth is drastically narrowed to the 1 Hz level (Fig. 5.6). This represents a substantial improvement compared to the 16.3 MHz linewidth in the free-running state, demonstrating a remarkable enhancement.

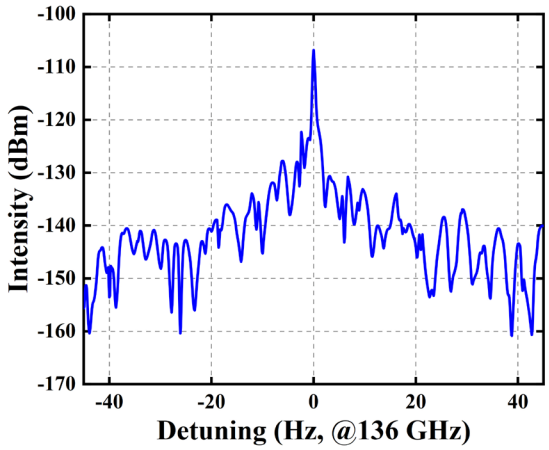

Fig. 5.6. Spectrum with 1 Hz RBW and 200 Hz span at center frequency of 136 GHz.

5.3 SSB phase noise

Furthermore, by using the built-in functions of the ESA, the single-sideband (SSB) phase noise of the RF signal in the locked state can be measured. This provides a detailed analysis of the signal's phase stability and noise performance.

SSB phase noise represents the noise power density as a function of frequency offset from the carrier, expressed in dBc/Hz. It quantifies how much noise is present in a signal's phase at a given frequency offset from the carrier. Essentially, SSB phase noise describes the purity of an oscillator or signal source, indicating the extent to which the signal deviates from an ideal, pure periodic wave.

The analysis of the SSB phase noise was conducted on the 67.75 GHz DWL. Optical injection locking was performed by setting the OFC frequency spacing at four different sub-harmonic levels: 5× (13.55 GHz), 10× (6.775 GHz), 20× (3.3875 GHz), and 30× (2.255 GHz), corresponding to different sub-harmonics for the DWL beat frequency. This allowed for a comparison of phase noise performance across varying degrees of sub-harmonic injection locking. As shown in Fig 5.7, the blue line represents the phase noise of the intrinsic frequency of the OFC (i.e., the fundamental harmonic), the red line shows the phase noise

of the 67.75 GHz signal in the locked state, and the green line is calculated based on the blue line, taking into account the relationship between the phase noise of the frequency comb and the harmonic order, as expressed by the following equation,

$$L(f)_N = L(f)_1 + 20log_{10}(N) \tag{5.1}$$

Where, $L(f)_1$ represents the phase noise of the first harmonic, and $L(f)_N$ represents the phase noise of the Nth sub-harmonic. This relationship shows that the phase noise increases with higher sub-harmonic orders.

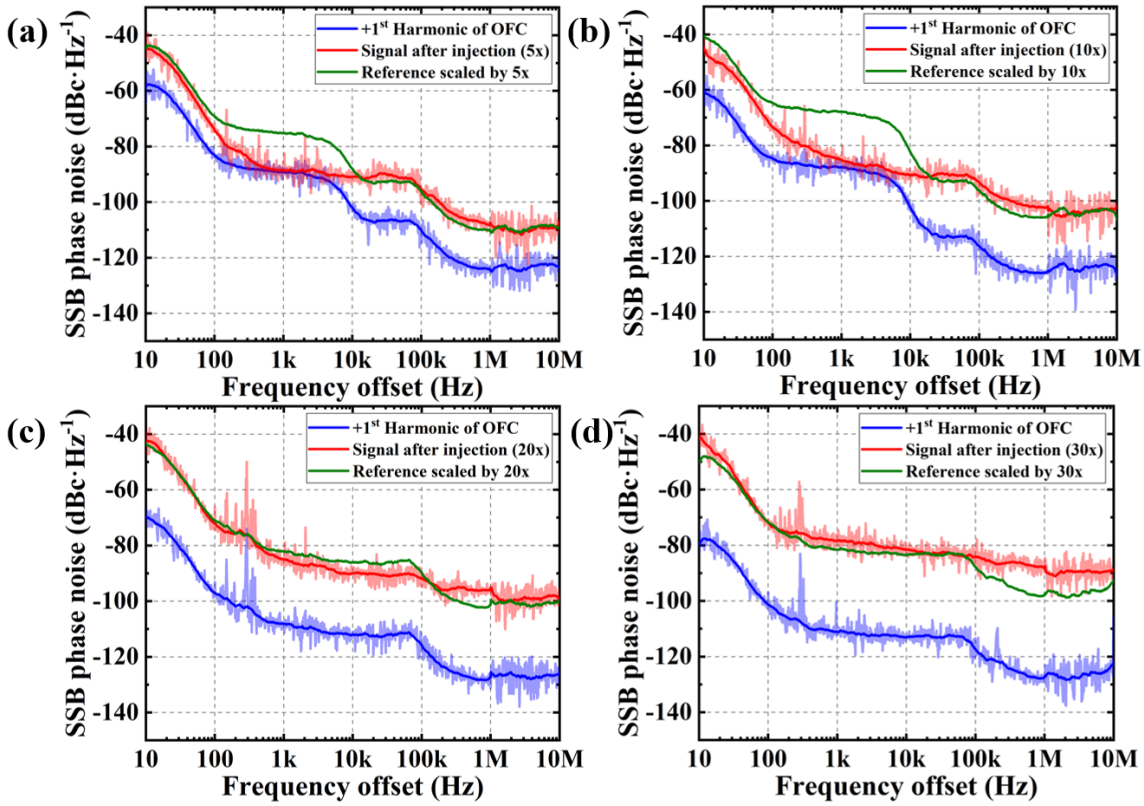

Fig. 5.7. SSB phase noise analysis when the OFC's frequency interval is set as 5× (a), 10× (b), 20× (c) and 30× (d) sub-harmonics of the DWL beat frequency (67.75 GHz).

For the 5x and 10x frequency multiplications, shown in Fig 5.7 (a) and (b), the red and green lines completely overlap in the 10 kHz to 10 MHz range. This confirms the successful completion of injection locking, also indicating that during this process, the phase noise degradation is solely due to the harmonic multiplication (as Equation 5.1), no additional noise was introduced by the system. It is found that in the 100 Hz to 10 kHz range, the red line shows lower noise than the green line. Considering that in this frequency band, the OFC's noise mainly stems from mechanical vibrations and 1/f noise, this could be due to the bandwidth and power limitations of the injection locking process. As a result, the noise at these offset frequencies may not be fully transferred to the DWL, leading to reduced noise in the locked state.

In Fig 5.7 (c), when the OFC frequency spacing is set to 3.3875 GHz, no additional noise is observed in the 100 Hz to 10 kHz range for the intrinsic frequency signal. As a result, the overall overlap between the green and red lines is quite good.

In Fig 5.7(d), due to a certain frequency detuning, the DWL was not fully locked, resulting in the red line showing slightly higher noise than the green line in the 100 kHz to 10 MHz range. This can also be observed from the fluctuations in the noise floor seen in Fig 5.4 (b).

Overall, the results show that the injection locking process successfully multiplies the external RF signal's frequency without introducing additional phase noise. Notably, previous studies have reported using an OFC to inject two independent single-wavelength lasers to generate high-quality RF signals [178, 179]. However, in both of these studies, the measured SSB phase noise exceeded the predicted values for OFC frequency multiplication. This discrepancy may be due to the use of two independent lasers, each requiring its own external current source, which introduces additional noise. Furthermore, the temperature disturbances across the two chips could also increase noise levels. In summary, injecting and locking a single DWL appears to offer a distinct advantage in terms of noise control.

5.4 Chapter summary

In this chapter, the experiment demonstrated that optically injecting an external OFC into the DWL narrowed the RF signal's linewidth to the 1 Hz range. This experiment highlighted several key features:

First, within the allowable frequency detuning range, only a minimal injection ratio is required to achieve locking. In the demonstrated results, the injected OFC energy was consistently below 500 μW. In contrast, techniques such as actively mode-locked lasers, where an external RF signal is directly applied to the saturable absorber or gain region, typically require much higher RF injection power (significantly larger than 1 mW) to achieve locking [180]. Additionally, when injecting RF signals using microstrip lines or coplanar waveguides, extra impedance matching is often needed to achieve optimal performance. Optical injection, however, does not require such impedance matching, making it simpler and more versatile in terms of application.

Secondly, based on the phase noise results, the optical injection of the OFC into a single DWL does not introduce additional noise while achieving frequency multiplication and

amplification. This characteristic has not been reported when locking two independent lasers for RF frequency generation. The reasons include that the DWL requires fewer external power sources and has better thermal stability. Another potential reason is that when the phases of the two wavelengths are locked, the device operates in a period one oscillation state [181, 182], resulting in smaller noise fluctuations compared to the noise generated by two independently excited wavelengths from separate devices.

In conclusion, this experiment provides a method in the optical domain for generating high-quality RF signals, significantly expanding the application potential and scope of DWL chips.

Chapter 6: Future discussion

The entire thesis presents the design approach, simulation results, and experimental outcomes for DWL systems generating beat frequencies in the MMW and THz range. The experiments successfully validated the generation of signals in the 50 GHz to 1 THz range. Furthermore, the experiments demonstrated that optical injection locking based on OFC can produce signals with quality that matches or even surpasses those generated by conventional electronic methods for MMW and THz. Given the extremely low loss in optical fibre transmission and the development of technologies like RoF (Radio-over-Fiber), the DWL chip discussed in this thesis holds both research value and practical application potential. In the future, DWL chips could be explored and researched in the following areas:

1. **Higher Beat Frequency:** For frequencies above 1 THz, the superimposed sampled Bragg grating (SBG) structure remains suitable. By tuning the sampling period in coordination with the seed grating period, this structure can easily cover a lasing wavelength range spanning several tens of nanometers. The challenge lies in ensuring that the quantum well structure provides a flatter gain profile. Currently, the material gain spectrum of conventional MQW structures have a 3 dB bandwidth of approximately 6-8 nm, which corresponds to less than 10 THz. When there is a significant difference in material gain between the two lasing wavelengths, the phenomenon of "the stronger gets stronger" may occur, where only the higher gain mode lases at a given time. To address this, modifying the quantum well composition or introducing an asymmetric MQW structure to achieve a flatter gain spectrum could further extend the applicability of THz DWL devices. Of course, for frequencies above 1 THz, if the challenge of operating temperature can be addressed, QCL may present a superior solution due to their higher output power and the fact that they do not require external PD.
2. **Hybrid Integration of Frequency Comb and DWL:** Currently, it appears that after OFC injection, the primary source of system noise is the OFC itself. The lowest noise OFCs have been reported on SiN platforms [56]. A potential future direction would involve hybrid integration of the OFC and DWL on a single chip, combining the low-noise characteristics of SiN-based OFCs with the DWL's high-performance RF signal generation capabilities. Several methods have already been reported to achieve this functionality, including photonic wire bonding and heterogeneous integration [183, 184]. The former uses polymer waveguide bonds to connect III-V lasers with SiN microrings, creating an efficient light path between the two

components. The latter involves cleaving and bonding two different devices onto the same substrate while aligning their waveguides. Both of these techniques have been successfully demonstrated and applied in various photonic integration scenarios.

3. **Electro-Optical-Electrical Frequency Multiplication System:** Once phase locking is achieved, the RF signal generated by the device demonstrates quality that matches or even surpasses that of conventional electronic solutions. Although this was not demonstrated in this thesis, based on phenomena observed in harmonic mode-locked lasers, it is possible to achieve phase locking by injecting sub-harmonics of the DWL's frequency into the EAM section of the DWL. This process effectively loads the RF signal onto the optical signal. If high-speed PD is then integrated on the same platform using techniques such as selective area growth (SAG) [185], butt joint integration, or photonic wire bonding, and then the phase-locked optical beat frequency is detected, the system would complete an electro-optical-electrical signal conversion and frequency multiplication process. Based on results from OFC injection locking, this process can easily achieve 10x frequency multiplication or higher, with the multiplied signals reaching THz frequencies, which is difficult for conventional electronic circuits to achieve.

   However, there are several challenges with this approach, including: Material lattice mismatch and inherent RC oscillations: Growing UTC-PD structures together with III-V lasers on the same substrate is difficult due to lattice mismatch between materials; The inherent RC oscillations of the device can impede the injection of high-frequency signals, limiting the system's performance at higher frequencies.

In this thesis, another point worth discussing in the future is the role played by the EAM section. The EAM section here is considered to act as a phase modulator, balancing and compensating the end-face phases of the dual wavelength. When a reverse bias is applied to modulate the EAM, this region enters a state of light absorption, note that this absorption is saturable. Similar to passive mode-locked lasers, if the power of the dual wavelengths is sufficiently high, or if the beat frequency signal reaches the saturation condition of the EAM, it will momentarily stop absorbing the optical signal [186-188]. In other words, the overall loss of the device will change, following the beat frequency signal, locking the output state of the device through a gain-loss mechanism. At this point, due to the net gain oscillating with the beat frequency, the DWL operates in a state similar to amplitude-modulated output. It is important to note that, the output is a continuous sine wave rather than pulses.

However, unlike passive mode-locked lasers, it is difficult to check whether the EAM in a DWL can reach a saturated state to produce this locking mechanism. This is because, as

long as the phase relationship is appropriate, the two wavelengths can operate in a CW state, potentially without the involvement of the EAM section [189]. Moreover, even if the EAM does not cause net gain oscillation in the device and the two wavelengths operate in a CW output mode, a beat frequency signal can still be generated in the PD. In the future, this phenomenon is worth investigating, as once the EAM oscillates between saturation and absorption states, it effectively applies a self modulation signal to the device at a frequency matching the beat frequency. This has the potential to further enhance the quality of the beat signal without the need for external injection locking.

Reference

[1] E. Ezhilarasan and M. Dinakaran. "A review on mobile technologies: 3G, 4G and 5G." 2017 second international conference on recent trends and challenges in computational models ICRTCCM. IEEE, 2017.

[2] D.R. Vizard, "millimeter-wave applications: from satellite communications to security systems.," in Microwave Journal, vol. 49, pp.7, 2006.

[3] K. Komsan, and C. Wang. "A wideband resonant cavity antenna assembled using a micromachined CPW-fed patch source and a two-layer metamaterial superstrate," in IEEE Transactions on Components, Packaging and Manufacturing Technology, vol. 9, issue. 6, pp. 1142-1150,2018.

[4] S. Ashraf, J. A. Sheikh, A. Ashraf, U. Rasool, "5G Millimeter Wave Technology: An Overview, " In: Sheikh, J.A., Khan, T., Kanaujia, B.K. eds Intelligent Signal Processing and RF Energy Harvesting for State of art 5G and B5G Networks. Energy Systems in Electrical Engineering. Springer, Singapore, 2024.

[5] Q. -D. Cao, X. -X. Yang, F. Yu and S. Gao, "High Scanning Rate Millimeter-Wave Circularly Polarized CTS Leaky Wave Antenna," in IEEE Transactions on Antennas and Propagation, vol. 72, no. 7, pp. 6087-6092, July 2024,

[6] R. Tiwari, D. Sharma, P. Singh, et al., "A flexible dual-band 4 × 4 MIMO antenna for 5G mm-wave 28/38 GHz wearable applications, " in Scientific Report, vol. 14, pp. 14324 2024.

[7] B. Yang, Z. Yu, J. Lan, R. Zhang, J. Zhou and W. Hong, "Digital Beamforming-Based Massive MIMO Transceiver for 5G Millimeter-Wave Communications," in IEEE Transactions on Microwave Theory and Techniques, vol. 66, no. 7, pp. 3403-3418, July 2018

[8] Y. Wang et al., "Broadband Millimeter-Wave GaAs Dual-Function Switching Attenuators With Low Insertion Loss and Large Attenuation Range," in IEEE Journal on Emerging and Selected Topics in Circuits and Systems, vol. 14, no. 1, pp. 100-110, March 2024.

[9] A. Hubrechsen, L. A. Bronckers, A. C. F. Reniers and A. B. Smolders, "Atmospheric Attenuation in a mmWave Reverberation Chamber," in IEEE Antennas and Wireless Propagation Letters, vol. 23, no. 6, pp. 1730-1733, June 2024.

[10] M. Noor-A-Rahim et al., "6G for Vehicle-to-Everything V2X Communications: Enabling Technologies, Challenges, and Opportunities," in Proceedings of the IEEE, vol. 110, no. 6, pp. 712-734, June 2022.

[11] X. Liang, J. Jiao, S. Wu and Q. Zhang, "Outage Analysis of Multirelay Multiuser Hybrid Satellite-Terrestrial Millimeter-Wave Networks," in IEEE Wireless Communications Letters, vol. 7, no. 6, pp. 1046-1049, Dec. 2018.

[12] I. Leyva-Mayorga et al., "LEO Small-Satellite Constellations for 5G and Beyond-5G Communications," in IEEE Access, vol. 8, pp. 184955-184964, 2020.

[13] D. M. Mittleman, "Twenty years of terahertz imaging [Invited]," in Optics Express, vol. 26, pp. 9417-9431, 2018.

[14] Y. Wu, Y. Wang, D. Bao, et al., "Emerging probing perspective of two-dimensional materials physics: terahertz emission spectroscopy, " in Light Science & Applications, vol. 13, pp. 146, 2024.

[15] U. Welp, K. Kadowaki, R. Kleiner, "Superconducting emitters of THz radiation, " in Nature Photonics, vol. 7, pp.702–710, 2013.

[16] T. Nagatsuma, G. Ducournau, G, C. Renaud, "Advances in terahertz communications accelerated by photonics, " in Nature Photonics, vol. 10, pp. 371–379, 2016.

[17] Y. Liang, Z. Liu, Q. Tian, et al., "Widely tunable electron bunch trains for the generation of high-power narrowband 1–10 THz radiation, " in Nature Photonics, vol. 17, pp. 259–263, 2023.

[18] A. Boulogeorgos et al., "Terahertz Technologies to Deliver Optical Network Quality of Experience in Wireless Systems Beyond 5G," in IEEE Communications Magazine, vol. 56, no. 6, pp. 144-151, June, 2018.

[19] H. Wymeersch et al., "Integration of Communication and Sensing in 6G: a Joint Industrial and Academic Perspective," 2021 IEEE 32nd Annual International Symposium on Personal, Indoor and Mobile Radio Communications PIMRC, Helsinki, Finland, 2021, pp. 1-7.

[20] O. Li et al., "Integrated Sensing and Communication in 6G A Prototype of High Resolution THz Sensing on Portable Device," 2021 Joint European Conference on Networks and Communications & 6G Summit EuCNC/6G Summit, Porto, Portugal, 2021, pp. 544-549.

[21] S. Helal, H. Sarieddeen, H. Dahrouj, T. Y. Al-Naffouri and M. -S. Alouini, "Signal Processing and Machine Learning Techniques for Terahertz Sensing: An overview," in IEEE Signal Processing Magazine, vol. 39, no. 5, pp. 42-62, Sept. 2022.

[22] C. Zandonella, "T-ray specs," in Nature, vol. 424, pp. 721–722, 2003.

[23] E. C. Camus, M. Koch, D.M. Mittleman, "Recent advances in terahertz imaging: 1999 to 2021, " in Applied Physics B, vol. 128, pp. 12, 2022.

[24] H. Sarieddeen, M. -S. Alouini and T. Y. Al-Naffouri, "Terahertz-Band Ultra-Massive Spatial Modulation MIMO," in IEEE Journal on Selected Areas in Communications, vol. 37, no. 9, pp. 2040-2052, Sept. 2019.

[25] M. Lotti, G. Pasolini, A. Guerra, F. Guidi, R. D'Errico and D. Dardari, "Radio SLAM for 6G Systems at THz Frequencies: Design and Experimental Validation," in IEEE Journal of Selected Topics in Signal Processing, vol. 17, no. 4, pp. 834-849, July 2023.

[26] D. Serghiou, M. Khalily, T. W. C. Brown and R. Tafazolli, "Terahertz Channel Propagation Phenomena, Measurement Techniques and Modeling for 6G Wireless Communication Applications: A Survey, Open Challenges and Future Research Directions," in IEEE Communications Surveys & Tutorials, vol. 24, no. 4, pp. 1957-1996, 2022.

[27] ITU-R P.676, “Attenuation by atmospheric gases and related effects,” ITU-R, Recommendation P676-12, 08, 2019.

[28] A. Maestrini, "Frequency tunable electronic sources working at room temperature in the 1 to 3 THz band, " in Terahertz Emitters, Receivers, and Applications III, vol. 8496. 2012.

[29] I. Mehdi, J. V. Siles, C. Lee and E. Schlecht, "THz Diode Technology: Status, Prospects, and Applications," in Proceedings of the IEEE, vol. 105, no. 6, pp. 990-1007, June 2017.

[30] K. M. K. H. Leong et al., "A 0.85 THz Low Noise Amplifier Using InP HEMT Transistors," in IEEE Microwave and Wireless Components Letters, vol. 25, no. 6, pp. 397-399, June 2015.

[31] Z. Hu, M. Kaynak and R. Han, "High-Power Radiation at 1 THz in Silicon: A Fully Scalable Array Using a Multi-Functional Radiating Mesh Structure," in IEEE Journal of Solid-State Circuits, vol. 53, no. 5, pp. 1313-1327, May 2018.

[32] D. Marpaung, J. Yao, J. Capmany, " Integrated microwave photonics, " in Nature Photonics, vol. 13, pp. 80–90, 2019.

[33] E. Pelucchi, G. Fagas, I. Aharonovich, et al., "The potential and global outlook of integrated photonics for quantum technologies, " in Nature Review Physics, vol. 4, pp. 194–208, 2022.

[34] J. Yao, F. Zeng and Q. Wang, "Photonic Generation of Ultrawideband Signals," in Journal of Lightwave Technology, vol. 25, no. 11, pp. 3219-3235, Nov. 2007.

[35] C. Lim et al., "Fiber-Wireless Networks and Subsystem Technologies," in Journal of Lightwave Technology, vol. 28, no. 4, pp. 390-405, Feb.15, 2010.

[36] T. Umezawa, P. T. Dat, K. Kashima, A. Kanno, N. Yamamoto and T. Kawanishi, "100-GHz Radio and Power Over Fiber Transmission Through Multicore Fiber Using Optical-to-Radio Converter," in Journal of Lightwave Technology, vol. 36, no. 2, pp. 617-623, 15 Jan.15, 2018.

[37] W. Zhang, J. Yao, "A fully reconfigurable waveguide Bragg grating for programmable photonic signal processing, " in Nature Communications, vol. 9, pp.1396, 2018.

[38] V. Supradeepa, C. Long, R. Wu, et al., "Comb-based radiofrequency photonic filters with rapid tunability and high selectivity, " in Nature Photonics, vol. 6, pp. 186–194, 2012.

[39] P. Ghelfi, F. Laghezza, F. Scotti, et al., "A fully photonics-based coherent radar system.," in Nature, vol. 507, pp. 341–345, 2014.

[40] Y. Zhang, et al., "A broadband THz-TDS system based on DSTMS emitter and LTG InGaAs/InAlAs photoconductive antenna detector," in Scientific Reports, vol. 6, pp. 26949 2016.

[41] L. Duvillaret, F. Garet and J. . -L. Coutaz, "A reliable method for extraction of material parameters in terahertz time-domain spectroscopy," in IEEE Journal of Selected Topics in Quantum Electronics, vol. 2, no. 3, pp. 739-746, Sept. 1996.

[42] M. Naftaly and R. E. Miles, "Terahertz Time-Domain Spectroscopy for Material Characterization," in Proceedings of the IEEE, vol. 95, no. 8, pp. 1658-1665, Aug. 2007.

[43] M. Tonouchi, "Cutting-edge terahertz technology, " in Nature Photonics, vol. 1, pp. 97–105, 2007.

[44] J. Faist, et al., "Quantum cascade laser," in Science, vol. 264, pp.553-556, 1994.

[45] Y. Yao, A. J. Hoffman, C. F. Gmachl, "Mid-infrared quantum cascade lasers," in Nature Photonics, vol. 6, pp. 432-439, 2012.

[46] R. Köhler et al. "Terahertz semiconductor-heterostructure laser," in Nature, vol, 417, pp. 156-159, 2002.

[47] E. Mujagić et al., "Vertically emitting terahertz quantum cascade ring lasers." in Applied Physics Letters, vol. 95, pp. 1, 2009.

[48] R. Köhler et al., "High-intensity interminiband terahertz emission from chirped superlattices," in Applied physics letters, vol. 80, pp.1867-1869, 2002.

[49] S. W. Benjamin, "Terahertz quantum-cascade lasers." in Nature photonics 1.9, pp 517-525, 2007.

[50] C. Sirtori, "Bridge for the terahertz gap." in Nature, vol. 417, pp. 132-133, 2002.

[51] S. Kumar, "Recent Progress in Terahertz Quantum Cascade Lasers," in IEEE Journal of Selected Topics in Quantum Electronics, vol. 17, no. 1, pp. 38-47, Jan.-Feb. 2011.

[52] S. Kumar, C. Chan, Q. Hu et al., "A 1.8-THz quantum cascade laser operating significantly above the temperature of $\hbar\omega$/kB, " in Nature Physics, vol. 7, pp. 166–171, 2011.

[53] S. Kumar, Q. Hu, J. L. Reno, "186 K operation of terahertz quantum-cascade lasers based on a diagonal design," in Applied. Physics. Letters, vol. 94, pp. 131105, 2009.

[54] T. Schibli, I. Hartl, D. Yost et al., "Optical frequency comb with submillihertz linewidth and more than 10 W average power," in Nature Photonics, vol. 2, pp. 355–359, 2008.

[55] C. Wang, M. Zhang, M. Yu, et al., "Monolithic lithium niobate photonic circuits for Kerr frequency comb generation and modulation, " in Nature Communications, vol. 10, pp. 978, 2019.

[56] J. Liu et al., "Photonic microwave generation in the X-and K-band using integrated soliton microcombs," in Nature Photonics, vol. 14, pp. 486-491, 2020.

[57] J. Warren, et al., "Hertz-linewidth semiconductor lasers using CMOS-ready ultra-high-Q microresonators," in Nature Photonics, vol. 15, pp. 346-353, 2021.

[58] S. Sun, B. Wang, K. Liu, et al., "Integrated optical frequency division for microwave and mmWave generation, " in Nature, vol. 627, pp. 540–545, 2024.

[59] Y. Zhao, J. K. Jang, G. J. Beals et al., "All-optical frequency division on-chip using a single laser, " in Nature, vol. 627, pp. 546–552, 2024.

[60] H. Kogelnik, C. V. Shank, "Stimulated Emission In A Periodic Structure, " in Applied Physics Letters, vol. 15, pp. 152–154, 1971.

[61] H. Kogelnik, C. V. Shank "Coupled-Wave Theory of Distributed Feedback Lasers, " in Journal of Applied Physics, vol. 4, pp. 2327–2335, 1 May 1972.

[62] Y. Itaya, T. Matsuoka, K. Kuroiwa and T. Ikegami, "Longitudinal mode behaviors of 1.5 μm range GaInAsP/InP distributed feedback lasers," in IEEE Journal of Quantum Electronics, vol. 20, no. 3, pp. 230-235, March 1984.

[63] A. Yariv, "Coupled-mode theory for guided-wave optics," in IEEE Journal of Quantum Electronics, vol. 9, no. 9, pp. 919-933, September 1973.

[64] J. -R. Qian, J. Su, L. -L. Xue and L. Yang, "Coupled-Mode Analysis for Chiral Fiber Long-Period Gratings Using Local Mode Approach," in IEEE Journal of Quantum Electronics, vol. 48, no. 1, pp. 49-55, Jan. 2012.

[65] T. Erdogan, "Fiber grating spectra," in Journal of Lightwave Technology, vol. 15, no. 8, pp. 1277-1294, Aug. 1997.

[66] M. S. Muller, H. J. El-Khozondar, A. Bernardini and A. W. Koch, "Transfer Matrix Approach to Four Mode Coupling in Fiber Bragg Gratings," in IEEE Journal of Quantum Electronics, vol. 45, no. 9, pp. 1142-1148, Sept. 2009.

[67] Liang Dong and S. Fortier, "Formulation of time-domain algorithm for fiber Bragg grating simulation and reconstruction," in IEEE Journal of Quantum Electronics, vol. 40, no. 8, pp. 1087-1098, Aug. 2004.

[68] W. Zhang, W. Li and J. Yao, "Optical Differentiator Based on an Integrated Sidewall Phase-Shifted Bragg Grating," in IEEE Photonics Technology Letters, vol. 26, no. 23, pp. 2383-2386, 1 Dec.1, 2014.

[69] X. Wang, W. Shi, R. Vafaei, N. A. F. Jaeger and L. Chrostowski, "Uniform and Sampled Bragg Gratings in SOI Strip Waveguides With Sidewall Corrugations," in IEEE Photonics Technology Letters, vol. 23, no. 5, pp. 290-292, March1, 2011.

[70] Y. -B. Cho, B. -K. Yang, J. -H. Lee, J. -B. Yoon and S. -Y. Shin, "Silicon Photonic Wire Filter Using Asymmetric Sidewall Long-Period Waveguide Grating in a Two-Mode Waveguide," in IEEE Photonics Technology Letters, vol. 20, no. 7, pp. 520-522, April1, 2008.

[71] S. Mokhov, D. Ott, I. Divliansky, B. Zeldovich, and L. Glebov, "Moiré volume Bragg grating filter with tunable bandwidth," in Optics Express, vol. 22, pp. 20375-20386, 2014.

[72] C. Henry, "Theory of spontaneous emission noise in open resonators and its application to lasers and optical amplifiers," in Journal of Lightwave Technology, vol. 4, no. 3, pp. 288-297, March 1986.

[73] S. K. B. Lo and H. Ghafouri-Shiraz, "A method to determine the above-threshold stability of distributed feedback semiconductor laser diodes," in Journal of Lightwave Technology, vol. 13, no. 4, pp. 563-568, April 1995.

[74] T. Yamanaka, S. Seki and K. Yokoyama, "Numerical analysis of static wavelength shift for DFB lasers with longitudinal mode spatial hole burning," in IEEE Photonics Technology Letters, vol. 3, no. 7, pp. 610-612, July 1991.

[75] M. Okai, S. Tsuji and N. Chinone, "Stability of the longitudinal mode in lambda /4-shifted InGaAsP/InP DFB lasers," in IEEE Journal of Quantum Electronics, vol. 25, no. 6, pp. 1314-1319, June 1989.

[76] O. K. Kwon, Y. A. Leem, D. H. Lee, C. W. Lee, Y. S. Baek and Y. C. Chung, "Effects of Asymmetric Grating Structures on Output Efficiency and Single Longitudinal Mode Operation in λ/4-Shifted DFB Laser," in IEEE Journal of Quantum Electronics, vol. 47, no. 9, pp. 1185-1194, Sept. 2011.

[77] P. Nezih, and M. Karabiyik, "Electron beam lithography EBL." In Encyclopedia of Nanotechnology, pp. 1033-1057, 2016.

[78] R. Zheng, L. Qi, S. Li, Z. Gan, D. Zhao and M. Qiu, "Liquid Hydrogen Temperature Cryostage for Ice-Assisted Electron-Beam Lithography," *in IEEE Transactions on Instrumentation and Measurement, vol. 73, pp. 1-4, 2024*

[79] Z. Shu et al. "Programmable nanoscale crack lithography for multiscale PMMA patterns," in ACS Applied Materials & Interfaces, vol. 15, pp. 28349-28357, 2023.

[80] V. Jayaraman, Z. -M. Chuang and L. A. Coldren, "Theory, design, and performance of extended tuning range semiconductor lasers with sampled gratings," in IEEE Journal of Quantum Electronics, vol. 29, no. 6, pp. 1824-1834, June 1993.

[81] L. A. Coldren, G. A. Fish, Y. Akulova, J. S. Barton, L. Johansson and C. W. Coldren, "Tunable semiconductor lasers: a tutorial," in Journal of Lightwave Technology, vol. 22, no. 1, pp. 193-202, Jan. 2004.

[82] Y. Shi et al., "Study of the Multiwavelength DFB Semiconductor Laser Array Based on the Reconstruction-Equivalent-Chirp Technique," in Journal of Lightwave Technology, vol. 31, no. 20, pp. 3243-3250, Oct.15, 2013.

[83] J. Li et al., "A Multiexposure Technology for Sampled Bragg Gratings and its Applications in Dual-Wavelength Lasing Generation and OCDMA En/Decoding," in IEEE Photonics Technology Letters, vol. 21, no. 21, pp. 1639-1641, Nov.1, 2009.

[84] X. Wang et al., "Precise control of the coupling coefficient through destructive interference in silicon waveguide Bragg gratings," Opt. Lett. vol 39, pp. 5519-5522, 2014.

[85] B. Lin, et al., "Analysis of inverse-Gaussian apodized fiber Bragg grating," Appl. Opt. vol. 49, no. 25, pp. 4715-4722, 2010.

[86] B. Lin, S. Tjin, M. Jiang, and P. Shum, "Tunable microwave generation based on a dual-wavelength fiber laser with an inverse-Gaussian apodized fiber Bragg grating," in Applied. Optics, vol. 50, no. 25, pp. 4912-4916, 2011.

[87] S. Liu, et al., "Planar waveguide moiré grating," in Optics Express, vol. 25, pp. 24960-24973, 2017.

[88] W. Shi et al., “Silicon photonic grating-assisted, contra-directional couplers,” in Optics Express, vol. 213, pp. 3633–3650, 2013.

[89] D. C. J. Reid, C. M. Ragdale, I. Bennion, D. J. Robbins, J. Buus, and W. J. Stewart, “Phase-shiftd moiré grating fiber resonators,” in Electron. Lett, vol. 261, pp. 10–12 1990.

[90] M. Tang, H. Xie, J. Zhu, X. Li, and Y. Li, “Study of moiré grating fabrication on metal samples using nanoimprint lithography,” in Optics Express, vol. 203, pp. 2942–2955, 2012.

[91] R. Mizushima, T. Detani, C. Zhu, P. Wang, H. Zhao and H. Li, "The Superimposed Multi-Channel Helical Long-Period Fiber Grating and Its Application to Multi-Channel OAM Mode Generator," in Journal of Lightwave Technology, vol. 39, no. 10, pp. 3269-3275, 15 May15, 2021.

[92] S. Gao, C. Baker, L. Chen and X. Bao, "Fabrication of Multiple Superimposed Fiber Bragg Gratings for Multiple Parameter Sensing," in IEEE Sensors Letters, vol. 4, no. 7, pp. 1-4, July 2020.

[93] P. Peterka, P. Koška and J. Čtyroký, "Reflectivity of Superimposed Bragg Gratings Induced by Longitudinal Mode Instabilities in Fiber Lasers," in IEEE Journal of Selected Topics in Quantum Electronics, vol. 24, no. 3, pp. 1-8, May-June 2018.

[94] Y. -C. Wang et al., "Phase-Shifted Distributed Feedback Lasers With Two-Layer Moiré Gratings," in IEEE Photonics Technology Letters, vol. 32, no. 11, pp. 631-634, 1 June1, 2020.

[95] P. Chen, X. Liang, J. Ma and X. Zhang, "Research and Fabrication of the Chirped Moiré Fiber Bragg Grating With Tunable Channels Based on Temperature Control," in Journal of Lightwave Technology, vol. 42, no. 10, pp. 3852-3861, 15 May15, 2024.

[96] M. Tang, H. Xie, J. Zhu, X. Li, and Y. Li, "Study of moiré grating fabrication on metal samples using nanoimprint lithography," in Optics Express, vol. 20, pp. 2942-2955, 2012.

[97] R. Cheng, N. Jaeger, L. Chrostowski, "Fully tailorable integrated-optic resonators based on chirped waveguide Moiré gratings," in Optica, vol. 7, pp. 647-657, 2020.

[98] L. Hou, M. Haji, I. Eddie, H. Zhu, and J. H. Marsh, "Laterally coupled dual-grating distributed feedback lasers for generating mode-beat terahertz signals," in Optics Letters, vol. 40, pp. 182-185, 2015.

[99] Y. Dai, X. Chen, L. Xia, Y. Zhang, and S. Xie, "Sampled Bragg grating with desired response in one channel by use of a reconstruction algorithm and equivalent chirp," in Optics Letters, vol. 29, pp. 1333-1335, 2004.

[100] Y. Shi et al., "Study of the Multiwavelength DFB Semiconductor Laser Array Based on the Reconstruction-Equivalent-Chirp Technique," in Journal of Lightwave Technology, vol. 31, no. 20, pp. 3243-3250, Oct.15, 2013.

[101] S. Guan et al., "Research on the Asymmetric Corrugation-Pitch-Modulated HR-AR DFB Lasers With Sampled Gratings," in Journal of Lightwave Technology, vol. 39, no. 14, pp. 4725-4736, July15, 2021.

[102] Y. Zhang et al., "Study on Two-Section DFB Lasers and Laser Arrays Based on the Reconstruction Equivalent Chirp Technique and Their Application in Radio-Over-Fiber Systems," in IEEE Journal of Selected Topics in Quantum Electronics, vol. 21, no. 6, pp. 232-240, Nov.-Dec. 2015.

[103] L. Wang et al., "Optical Circuit Switching Using REC-DFB Laser Array," in Journal of Lightwave Technology, vol. 42, no. 8, pp. 2880-2886, 15 April15, 2024.

[104] Y. Zhang et al., "Over 100 mW O-Band Multi-Wavelength DFB Laser Array for Optical I/O Technology," in IEEE Photonics Technology Letters, vol. 36, no. 13, pp. 821-824, 1 July1, 2024.

[105] J. Zhao et al., "Multi-Wavelength DFB Laser With High Mode Stability and Uniform Spacing for Optical I/O Technology," in Journal of Lightwave Technology, vol. 42, no. 14, pp. 4874-4881, 15 July15, 2024.

[106] L. M. Zhang, S. F. Yu, M. C. Nowell, D. D. Marcenac, J. E. Carroll and R. G. S. Plumb, "Dynamic analysis of radiation and side-mode suppression in a second-order DFB laser using time-domain large-signal traveling wave model," in IEEE Journal of Quantum Electronics, vol. 30, no. 6, pp. 1389-1395, June 1994.

[107] A. Akrout, K. Dridi and T. J. Hall, "Dynamic Analysis of High-Order Laterally Coupled DFB Lasers Using Time-Domain Traveling-Wave Model," in IEEE Journal of Quantum Electronics, vol. 48, no. 10, pp. 1252-1258, Oct. 2012.

[108] N. Holonyak, R. Kolbas, R. Dupuis and P. Dapkus, "Quantum-well heterostructure lasers," in IEEE Journal of Quantum Electronics, vol. 16, no. 2, pp. 170-186, February 1980

[109] C. Henry, "Theory of the linewidth of semiconductor lasers," in IEEE Journal of Quantum Electronics, vol. 18, no. 2, pp. 259-264, February 1982.

[110] D. Marcenac, J. Carroll, "Quantum-mechanical model for realistic Fabry—Perot lasers, " in IEE Proceedings J Optoelectronics, vol. 140, pp. 157-171, 1993.

[111] K. Petermann, "Calculated spontaneous emission factor for double-heterostructure injection lasers with gain-induced waveguiding," in IEEE Journal of Quantum Electronics, vol. 15, no. 7, pp. 566-570, July 1979.

[112] K. Utaka, S. Akiba, K. Sakai and Y. Matsushima, "Effect of mirror facets on lasing characteristics of distributed feedback InGaAsP/InP laser diodes at 1.5 μm range," in IEEE Journal of Quantum Electronics, vol. 20, no. 3, pp. 236-245, March 1984.

[113] R. D. Martin et al., "CW performance of an InGaAs-GaAs-AlGaAs laterally-coupled distributed feedback LC-DFB ridge laser diode," in IEEE Photonics Technology Letters, vol. 7, no. 3, pp. 244-246, March 1995.

[114] K. David, J. Buus and R. G. Baets, "Basic analysis of AR-coated, partly gain-coupled DFB lasers: the standing wave effect," in IEEE Journal of Quantum Electronics, vol. 28, no. 2, pp. 427-434, Feb. 1992.

[115] F. Grillot, "On the Effects of an Antireflection Coating Impairment on the Sensitivity to Optical Feedback of AR/HR Semiconductor DFB Lasers," in IEEE Journal of Quantum Electronics, vol. 45, no. 6, pp. 720-729, June 2009.

[116] Y. Arakawa and A. Yariv, "Quantum well lasers--Gain, spectra, dynamics," in IEEE Journal of Quantum Electronics, vol. 22, no. 9, pp. 1887-1899, September 1986.

[117] D. Miller et al., "The quantum well self-electrooptic effect device: Optoelectronic bistability and oscillation, and self-linearized modulation," in IEEE Journal of Quantum Electronics, vol. 21, no. 9, pp. 1462-1476, September 1985.

[118] G. Bastard and J. Brum, "Electronic states in semiconductor heterostructures," in IEEE Journal of Quantum Electronics, vol. 22, no. 9, pp. 1625-1644, September 1986.

[119] N. Holonyak, R. Kolbas, R. Dupuis and P. Dapkus, "Quantum-well heterostructure lasers," in IEEE Journal of Quantum Electronics, vol. 16, no. 2, pp. 170-186, February 1980.

[120] R. Nagarajan, M. Ishikawa, T. Fukushima, R. S. Geels and J. E. Bowers, "High speed quantum-well lasers and carrier transport effects," in IEEE Journal of Quantum Electronics, vol. 28, no. 10, pp. 1990-2008, Oct. 1992.

[121] C. Zah et al., "High-performance uncooled 1.3-/spl mu/m Al/sub x/Ga/sub y/In/sub 1-x-y/As/InP strained-layer quantum-well lasers for subscriber loop applications," in IEEE Journal of Quantum Electronics, vol. 30, no. 2, pp. 511-523, Feb. 1994.

[122] W. G. Daniel, "Numerical Simulations of Gain and Power of a Multi-Quantum Well Laser," 2021 SBFoton International Optics and Photonics Conference SBFoton IOPC, Sao Carlos, Brazil, 2021.

[123] A. Polimeni, M. Capizzi, M. Geddo, M. Fischer, M. Reinhardt, A. Forchel, "Effect of temperature on the optical properties of InGaAsN/GaAs single quantum wells," in Applied Physics Letters, vol. 77, pp. 2870–2872, 2000.

[124] H. Peyre, F. Alsina, J. Camassel, J. Pascual, R. W. Glew; "Thermal stability of InGaAs/InGaAsP quantum wells," in journal of Applied Physics, vol. 73, pp. 3760–3768, 1993.

[125] J. Javaloyes and S. Balle, "Detuning and Thermal Effects on the Dynamics of Passively Mode-Locked Quantum-Well Lasers," in IEEE Journal of Quantum Electronics, vol. 48, no. 12, pp. 1519-1526, Dec. 2012.

[126] D. R. Medeiros et al., "Recent progress in electron-beam resists for advanced mask-making," in IBM Journal of Research and Development, vol. 45, no. 5, pp. 639-650, Sep. 2001.

[127] N. Vella, A. E. I. Joumha and A. Toureille, "Space charge measurement by the Thermal Step method and TSDC in PMMA," Proceedings of 8th International Symposium on Electrets ISE 8, Paris, France, 1994.

[128] Seoijin Park, Seong-Soo Kim, Liwei Wang and Seng-Tiong Ho, "InGaAsP-InP nanoscale waveguide-coupled microring lasers with submilliampere threshold current using Cl/sub 2/--N/sub 2/-based high-density plasma etching," in IEEE Journal of Quantum Electronics, vol. 41, no. 3, pp. 351-356, March 2005.

[129] K. Inoshita and T. Baba, "Fabrication of GaInAsP/InP photonic Crystal lasers by ICP etching and control of resonant mode in point and line composite defects," in IEEE Journal of Selected Topics in Quantum Electronics, vol. 9, no. 5, pp. 1347-1354, Sept.-Oct. 2003.

[130] Ü. Sökmen, et al., "Capabilities of ICP-RIE cryogenic dry etching of silicon: review of exemplary microstructures." in Journal of Micromechanics and Microengineering 19.10 2009: 105005.

[131] N. Furuhata, H. Miyamoto, A. Okamoto, K. Ohata, "Chemical dry etching of GaAs and InP by Cl2 using a new ultrahigh-vacuum dry-etching molecular-beam-epitaxy system," in Journal of Applied Physics, vol. 65, pp. 168–171, 1989.

[132] U. K. Chakrabarti, S. J. Pearton, and F. Ren. "Sidewall roughness during dry etching of InP," in Semiconductor science and technology, vol. 6, pp. 408, 1991.

[133] C. Chen, D. G. Yu, E. Hu, P. Petroff, "Photoluminescence studies on radiation enhanced diffusion of dry-etch damage in GaAs and InP materials, " in J. Vac. Sci. Technol. B, vol. 14, pp. 3684–3687, 1996.

[134] S. Choi, K. Djordjev, S. J. Choi, P. Daniel Dapkus "CH4-based dry etching of high Q InP microdisks, " in J. Vac. Sci. Technol. B, vol. 20, pp. 301–305, 2002.

[135] K. Nakahara et al., "Direct Modulation at 56 and 50 Gb/s of 1.3- μ m InGaAlAs Ridge-Shaped-BH DFB Lasers," in IEEE Photonics Technology Letters, vol. 27, no. 5, pp. 534-536, 1 March1, 2015.

[136] J. Li, S. Tang, J. Wang, Y. Liu, X. Chen and J. Cheng, "An Eight-Wavelength BH DFB Laser Array With Equivalent Phase Shifts for WDM Systems," in IEEE Photonics Technology Letters, vol. 26, no. 16, pp. 1593-1596, 15 Aug.15, 2014.

[137] T. Okamoto, N. Nunoya, Y. Onodera, T. Yamazaki, S. Tamura and S. Arai, "Optically pumped membrane BH-DFB lasers for low-threshold and single-mode operation," in IEEE Journal of Selected Topics in Quantum Electronics, vol. 9, no. 5, pp. 1361-1366, Sept.-Oct. 2003.

[138] N. W. Carlson, S. K. Liew, R. Amantea, D. P. Bour, G. A. Evans and E. A. Vangieson, "Mode discrimination in distributed feedback grating surface emitting lasers containing a buried second-order grating," in IEEE Journal of Quantum Electronics, vol. 27, no. 6, pp. 1746-1752, June 1991.

[139] S. Sakamoto, T. Okamoto, T. Yamazaki, S. Tamura and S. Arai, "Multiple-wavelength membrane BH-DFB laser arrays," in IEEE Journal of Selected Topics in Quantum Electronics, vol. 11, no. 5, pp. 1174-1179, Sept.-Oct. 2005.

[140] S. Nilsson, T. Kjellberg, T. Klinga, J. Wallin, K. Streubel and R. Schatz, "DFB laser with nonuniform coupling coefficient realized by double-layer buried grating," in IEEE Photonics Technology Letters, vol. 5, no. 10, pp. 1128-1131, Oct. 1993.

[141] R. Yu et al., "Top-down process of Germanium nanowires using EBL exposure of Hydrogen Silsesquioxane resist," 2012 13th International Conference on Ultimate Integration on Silicon ULIS, Grenoble, France, pp. 145-148, 2012.

[142] M. Yasui et al., "Fabrication of Glassy Carbon Molds Using Hydrogen Silsequioxane Patterned by Electron Beam Lithography as O2 Dry Etching Mask," 2007 Digest of papers Microprocesses and Nanotechnology, Kyoto, Japan, pp. 290-291. 2007.

[143] M.I. Alayo, I. Pereyra, M.N.P. Carreño, "Thick SiOxNy and SiO2 films obtained by PECVD technique at low temperatures, " in Thin Solid Films, vol. 332, pp. 40-45, 1998.

[144] J. Hnilica, et al. "PECVD of nanostructured SiO2 in a modulated microwave plasma jet at atmospheric pressure," in Journal of Physics D: Applied Physics, vol. 46, pp. 335202, 2013.

[145] M. Geis et al., "A novel anisotropic dry etching technique," In Journal of Vacuum Science and Technology, vol. 19, pp. 1390-1393, 1981.

[146] H. Hoff, et al., "Ohmic contacts to semiconducting diamond using a Ti/Pt/Au trilayer metallization scheme," in Diamond and Related Materials, vol. 12, pp.1450-1456, 1996.

[147] S. Kim, A. Ilesanmi, H. Heedon "Measurements of thermally induced nanometer-scale diffusion depth of Pt/Ti/Pt/Au gate metallization on InAlAs/InGaAs high-electron-mobility transistors," in Applied Physics Letters, vol.87, pp.23, 2005.

[148] P. D. Ye et al., "GaAs metal–oxide–semiconductor field-effect transistor with nanometer-thin dielectric grown by atomic layer deposition," in Applied Physics Letters, vol. 83-1, pp. 180-182, 2003.

[149] W. Min et al., "A comparative study of Ge/Au/Ni/Au-based ohmic contact on graphene," in Journal of Semiconductors, vol. 35.5, pp. 056001, 2014.

[150] J. Narayan, and O. W. Holland. "Rapid thermal annealing of ion-implanted semiconductors." in Journal of applied physics, 56.10, pp. 2913-2921, 1984.

[151] H. Karim, et al., "Doping of semiconductor devices by Laser Thermal Annealing," in Materials Science in Semiconductor Processing, vol. 62, pp. 92-102, 2017.

[152] R. Pawlus, S. Breuer, and M. Virte, "Control of dual-wavelength laser emission via optical feedback phase tuning," in Optics. Continuum, vol. 2, pp. 2186-2199, 2023.

[153] M. Virte, P. M. Palomo, "Integrated multi-wavelength lasers for all-optical processing of ultra-high frequency signals, " in Applied. Physics. Letters, vol. 123-18, pp. 180502, 2023.

[154] G. Verschaffelt, M. Khoder, "Directional power distribution and mode selection in micro ring lasers by controlling the phase and strength of filtered optical feedback," in Optics. Express, vol. 26, pp. 14315-14328, 2018.

[155] O. Nilsson and J. Buus, "Linewidth and feedback sensitivity of semiconductor diode lasers," in IEEE Journal of Quantum Electronics 26, 2039-2042, 1990.

[156] S. K. C. Liew, "Above-threshold analysis of loss-coupled DFB lasers: threshold current and power efficiency," in IEEE Photonics Technology Letters, 7, 1400-1402, 1995.

[157] J. Liu, X. Zhan, H. Yan, and W. Yang, "Theoretical analysis and experimental research on dynamic linewidth of DFB laser diodes under injection current tuning," in 2017 4th International Conference on Industrial Economics System and Industrial Security Engineering IEIS, IEEE, pp. 1-6, 2017.

[158] H. G. Zhang et al., "Narrow-Linewidth Microwave Generation Using a Self-Injected DBR Laser Diode," in IEEE Photonics Technology Letters, 21, 1045-1047, 2009.

[159] Z. Zhao, Z. Bai, D. Jin, Y. Qi, J. Ding, B. Yan, Y. Wang, Z. Lu, and R. P. Mildren, "Narrow laser-linewidth measurement using short delay self-heterodyne interferometry," Opt. Express 30, 30600-30610 2022.

[160] H. Ishii, K. Kasaya and H. Oohashi, "Spectral Linewidth Reduction in Widely Wavelength Tunable DFB Laser Array," IEEE Journal of Selected Topics in Quantum Electronics, vol. 15, no. 3, pp. 514-520, May-June, 2009.

[161] H. Li and N. B. Abraham, "Analysis of the noise spectra of a laser diode with optical feedback from a high-finesse resonator," in IEEE Journal of Quantum Electronics, vol. 25, no. 8, pp. 1782-1793, Aug. 1989.

[162] T. B. Simpson, J. -M. Liu, M. AlMulla, N. G. Usechak and V. Kovanis, "Linewidth Sharpening via Polarization-Rotated Feedback in Optically Injected Semiconductor Laser Oscillators," in IEEE Journal of Selected Topics in Quantum Electronics, vol. 19, no. 4, pp. 1500807-1500807, July-Aug. 2013.

[163] M. J. Golay, "A pneumatic infra-red detector," in Review of Scientific Instruments, vol. 18, pp. 357-362, 1947.

[164] R. Zhang et al., "Metal-Grating-Coupled Terahertz Quantum-Well Photodetectors," in IEEE Electron Device Letters, vol. 32, no. 5, pp. 659-661, May 2011.

[165] S. Ozer, U. Tumkaya, B. Asici and C. Besikci, "Demonstration and Performance Assessment of Large Format InP–InGaAsP Quantum-Well Infrared Photodetector Focal Plane Array," in IEEE Journal of Quantum Electronics, vol. 43, no. 8, pp. 709-713, Aug. 2007.

[166] A. Majumdar et al., "High-responsivity high-gain In/sub 0.53/Ga/sub 0.47/As-InP quantum-well infrared photodetectors grown using metal-organic vapor phase epitaxy," in IEEE Journal of Quantum Electronics, vol. 41, no. 6, pp. 872-878, June 2005.

[167] H. Ito, S. Kodama, Y. Muramoto, T. Furuta, T. Nagatsuma and T. Ishibashi, "High-speed and high-output InP-InGaAs unitraveling-carrier photodiodes," in IEEE Journal of Selected Topics in Quantum Electronics, vol. 10, no. 4, pp. 709-727, July-Aug. 2004.

[168] T. Ishibashi, Y. Muramoto, T. Yoshimatsu and H. Ito, "Unitraveling-Carrier Photodiodes for Terahertz Applications," in IEEE Journal of Selected Topics in Quantum Electronics, vol. 20, no. 6, pp. 79-88, Nov.-Dec. 2014.

[169] N. Shimizu, N. Watanabe, T. Furuta and T. Ishibashi, "InP-InGaAs uni-traveling-carrier photodiode with improved 3-dB bandwidth of over 150 GHz," in IEEE Photonics Technology Letters, vol. 10, no. 3, pp. 412-414, March 1998.

[170] H. Ito, T. Furuta, F. Nakajima, K. Yoshino and T. Ishibashi, "Photonic generation of continuous THz wave using uni-traveling-carrier photodiode," in Journal of Lightwave Technology, vol. 23, no. 12, pp. 4016-4021, Dec. 2005.

[171] Y. Matsui et al., "Chirp-managed directly modulated laser CML," in IEEE Photonics Technology Letters, vol. 18, no. 2, pp. 385-387, Jan. 15, 2006.

[172] R. Linke, "Modulation induced transient chirping in single frequency lasers," in IEEE Journal of Quantum Electronics, vol. 21, no. 6, pp. 593-597, June 1985.

[173] K. Sato, S. Kuwahara and Y. Miyamoto, "Chirp characteristics of 40-gb/s directly Modulated distributed-feedback laser diodes," in Journal of Lightwave Technology, vol. 23, no. 11, pp. 3790-3797, Nov. 2005.

[174] D. Shin, B.S. Kim, H. Jang, et al., "Photonic comb-rooted synthesis of ultra-stable terahertz frequencies, " in Nature Communications, vol. 14, pp. 790, 2023.

[175] S. Abdollahi, M. Ladouce, P. Marin-Palomo, "Agile THz-range spectral multiplication of frequency combs using a multi-wavelength laser, " Nature Communications, vol. 15, pp, 1305, 2024.

[176] A. C. Bordonalli, C. Walton and A. J. Seeds, "High-performance phase locking of wide linewidth semiconductor lasers by combined use of optical injection locking and optical phase-lock loop," in Journal of Lightwave Technology, vol. 17, no. 2, pp. 328-342, Feb. 1999.

[177] Z. Liu and R. Slavík, "Optical Injection Locking: From Principle to Applications," in Journal of Lightwave Technology, vol. 38, no. 1, pp. 43-59, 1 Jan.1, 2020.

[178] G. Schneider, J. Murakowski, C. Schuetz, et al., "Radiofrequency signal-generation system with over seven octaves of continuous tuning, " in Nature Photonics, vol. 7, pp. 118–122, 2013.

[179] J. Shi. et al., "Integrated dual-laser photonic chip for high-purity carrier generation enabling ultrafast terahertz wireless communications, " in Nature Communications, vol. 13, pp. 1388, 2022.

[180] M. Al-Rubaiee, B. Yuan, Y. Fan, S. Zhu, J. Marsh and L. Hou, "Ultrastable 10 GHz Mode-Locked Laser on Semi-Insulating Substrate Through RF Injection Locking," in IEEE Photonics Technology Letters, vol. 36, no. 19, pp. 1189-1192, 1 Oct.1, 2024.

[181] H. Luo, Y. Jiang, R. Dong, Y. Zi, X. Zhang and J. Tian, "A Tunable Single-Mode All-Optical Microwave Oscillator by Using Period-One Oscillation in DFB-LD," in IEEE Photonics Technology Letters, vol. 31, no. 6, pp. 491-494, 15 March15, 2019.

[182] G. Chen, D. Lu, L. Guo, W. Zhao, Y. Huang and L. Zhao, "Frequency-Tunable OEO Using a DFB Laser at Period-One Oscillations With Optoelectronic Feedback," in IEEE Photonics Technology Letters, vol. 30, no. 18, pp. 1593-1596, 15 Sept.15, 2018.

[183] Y. Wan et al., " Linewidth narrowing in self-injection-locked on-chip lasers, "in Light Science & Applications, vol. 12, pp. 162, 2023.

[184] C. Marco, et al., "A chip-scale second-harmonic source via self-injection-locked all-optical poling," in Light Science & Applications, vol. 12, pp. 296, 2023.

[185] T. Tanbun-Ek et al., "DFB lasers integrated with Mach-Zehnder optical modulator fabricated by selective area growth MOVPE technique," in IEEE Photonics Technology Letters, vol. 7, no. 9, pp. 1019-1021, Sept. 1995.

[186] H. A. Haus, "Mode-locking of lasers," in IEEE Journal of Selected Topics in Quantum Electronics, vol. 6, no. 6, pp. 1173-1185, Nov.-Dec. 2000.

[187] H. Haus, "Theory of mode locking with a slow saturable absorber," in IEEE Journal of Quantum Electronics, vol. 11, no. 9, pp. 736-746, September 1975.

[188] J. E. Bowers, P. A. Morton, A. Mar and S. W. Corzine, "Actively mode-locked semiconductor lasers," in IEEE Journal of Quantum Electronics, vol. 25, no. 6, pp. 1426-1439, June 1989.

[189] Y. Zhang et al., "A Stable Dual-Wavelength DFB Semiconductor Laser With Equivalent Chirped Sampled Grating," in IEEE Journal of Quantum Electronics, vol. 58, no. 1, pp. 1-7, Feb. 2022